Daniel Hauck

Magnetic 2π Domain Walls For Tunable Majorana Devices

Magnetic 2π Domain Walls for Tunable Majorana Devices

Zur Erlangung des akademischen Grades eines
Doktors der Naturwissenschaften (Dr. rer. nat.)
von der KIT-Fakultät für Physik des
Karlsruher Instituts für Technologie (KIT)

genehmigte

Dissertation

von

M. Sc. Daniel Hauck
geboren in Bruchsal, Deutschland

Tag der mündlichen Prüfung: 11. Juli 2025
Referent: Prof. Dr. Markus Garst
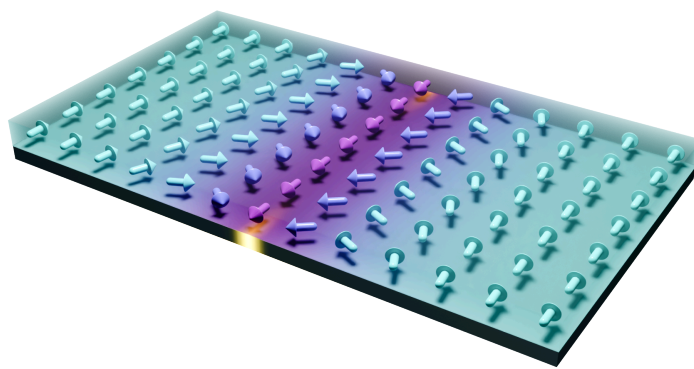Korreferent: Prof. Dr. Alexander Shnirman

The code used in this work is licensed under a *MIT* license
data: https://doi.org/10.35097/rjh6d2704g05qzsg
mbscluster: https://doi.org/10.5281/zenodo.15528160
kwant-braiding: https://doi.org/10.5281/zenodo.15467577

Abstract

Topological quantum computing aims to solve scaling and stability issues with current quantum computing platforms. Majorana bound states (MBSes) are a necessary ingredient for most proposals for topological quantum computing. Magnet-superconductor hybrids (MSHes) provide a promising platform for finding MBSes. We analyse the topology of MSHes with a magnetic 2π domain wall texture on the magnetic side and s-wave pairing and Rashba spin-orbit coupling (SOC) in the superconductor. The two layers are coupled with an antiferromagnetic exchange coupling. With this, we extend previous proposals concerning elongated skyrmions. We show that magnetic 2π domain walls are suitable for hosting MBSes and are advantageous compared to elongated skyrmions both for their attainability and mobility and for sidestepping issues with out-of-plane fields due to Pauli limiting. For various parameters of the system, we examine their influence on the topological phase space. Finally, we analyse the dynamics of the system under movement of the domain wall and show that MBSes can be moved in this way. This makes MSHes with magnetic 2π domain walls a suitable candidate for approachable and tunable Majorana devices.

Contents

Notation

$\boldsymbol{v}$: vector

$\hat{O}$: operator

$\bar{M}$: matrix

$\mathfrak{R}(x)$: real part of x

$\mathfrak{I}(x)$: imaginary part of x

x^*: complex conjugate of x

$\bar{M}^{\mathrm{T}}$: transpose of $\bar{M}$

$\bar{M}^\dagger = \left(\bar{M}^{\mathrm{T}}\right)^*$: hermitian conjugate of $\bar{M}$

$[\hat{A}, \hat{B}] = \hat{A}\hat{B} - \hat{B}\hat{A}$: commutator of $\hat{A}$ and $\hat{B}$

$\{\hat{A}, \hat{B}\} = \hat{A}\hat{B} + \hat{B}\hat{A}$: anti-commutator of $\hat{A}$ and $\hat{B}$

Introduction 1

Quantum computing is an active area of research that gathers a lot of interest. Quantum computers offer a different approach to performing computations compared to classical computers, by utilizing the exponential state space of a system of multi-state quantum systems, referred to as qubits, in the typical case of two states. Computations are performed through state rotations in this high-dimensional space state. For certain sets of problems, quantum computers are predicted to outperform classical computers[1]. While there are already functional quantum computers with over 100 qubits[2], scaling both the number of qubits and the possible size of programs running on them remains an unsolved question[3,4].

Topological systems are promising candidates to improve this situation[5–10]. They rely on a concept called topological protection. States of topological origin are stable against disorder and protected by an energy gap[7]. The computations in topological quantum computing are based on the statistics of non-abelian anyons, where the path of permutations is of importance[8]. This non-commutativity can be utilized to express quantum gates as braiding patterns of these anyons[11].

The most common candidate for such anyons is realised by Majorana bound states (MBSes) in topological superconductors, which are localised zero-dimensional edge states with a topological origin. While their statistics are anyonic, their structure is akin to Majorana fermions[12]. MBSes act as their particle-hole partner in the same vein as Majorana fermions are their own anti-particle. MBSes are a special case of Andreev bound states (ABSes) which exhibit a pinning to zero energy facilitated by topological protection[13]. While they were first proposed to exist in spinless p-wave superconducting wires[14], a spinful variation is necessary to realise them experimentally. This is typically done by utilizing a combination of magnetic Zeeman fields and spin-orbit coupling (SOC) in a wire with superconductive s-wave pairing, which is equivalent to spinless p-wave superconductivity in terms of the topology[15–17]. The wire set-up is usually realised using a semiconducting wire which is proximity coupled to a superconductor[18–22]. This setup is also part in the quantum computing chip recently presented by Microsoft[23].

For the computing use case, a one-dimensional wire alone is not sufficient any more. To braid the MBSes, the wire needs to be embedded in a two-dimensional layer[11,24]. T-junctions of wires provide one option to do this with nanowires. A similar approach is the usage of magnetic adatoms on top of an s-wave superconductor with SOC[25–29]. Here the topology manifests itself in localised regions of the two-dimensional superconductor. This work, however, focuses on the more flexible option of using fully two-dimensional structures. These magnet-superconductor hybrids (MSHes) are used in several proposals to obtain MBSes. They consist of a magnetic and a superconducting layer which are coupled through a Zeeman interaction. The effectively one-dimensional topology is accomplished though the use of magnetic textures. Among the many proposals for using MSHes for MBSes, magnetic skyrmions have been suggested to be suitable for this purpose[30–33]. While circular skyrmions can be paired with vortices in the superconductor[31], vortices are not necessary when using a magnetic texture in addition to an external field. Such setups have been proposed with various magnetic textures such as helical and cycloidal phases[32] or elongated skyrmions[30,33]. The latter are of particular interest as they make the Majorana pairs separately accessible. The mobility of the skyrmions also facilitates possible braiding operations[31], but they come with critical drawbacks of two kinds. On the magnetic side, elongated skyrmions are difficult to obtain and to move in a controlled way. More importantly, though, they require out-of-plane fields, which for the existence of topology must have a large magnitude with Zeeman energies larger than the superconducting gap[34]. Consequently, the setup faces the risk of breaking the superconductivity due to Pauli limiting and thus making the realisation of topology and therefore MBSes impossible, as they depend on the superconductivity. Both these issues can be circumvented with magnetic 2π domain walls. Magnetic domain walls are accessible in a wide range of materials[35–38] and movable with spin currents[39–43]. They also exist in in-plane configurations, which prevents breaking the pairing. This makes them more accessible than elongated skyrmions, while still providing access to dynamical features.

In this work, we examine the topology and potential of using magnetic 2π domain walls in MSHes to obtain and move MBSes. The content is structured in the following way. Chapter 2 contains an overview of the necessary background knowledge covering superconductivity, topology, magnetism, and the numerical methods. Chapter 3 then explores the topology in MSHes with static magnetic 2π domain walls and the influence of the parameters of the system. The dynamics

of movable domain walls and their limitations are evaluated in Chapter 4. We conclude with a summary of the work and an outlook towards possible future research directions in Chapter 5. Part of this work was published under Ref. [44].

Background 2

In this chapter, we discuss the basics of relevant topics for the rest of the work. We start with explaining the description of superconductors with an effective single particle Hamiltonian through the framework of Bogoliubov-de Gennes (BdG) theory. Afterwards, we give an introduction to topology itself before discussing the application to condensed matter physics and superconductors in particular. This is followed by a section on the basics of micromagnetics and an explanation of the magnetic parameters of the system. We continue with some basics of describing dynamical systems and conclude with an explanation of the numerical methods used for diagonalisation.

2.1 Superconductors

Superconductors form a class of materials, characterized by their low-temperature behaviour. It can be defined as the following:

> *A superconductor is a material that, below a critical temperature, is both a perfect conductor and a perfect diamagnet. [45]*

In more detail, this means that a superconductor has a low-temperature phase with both zero resistivity and perfectly expels magnetic fields[1].

2.1.1 Historical Overview

Historically[2], superconductors were first discovered by Heike Kamerlingh Onnes in 1911[47–51], when he measured the jump of resistivity to $0\,\Omega$ in mercury. In Figure 1, his measurements of the resistivity of mercury at the phase transition are shown.

With this, the first important and defining property of superconductors was discovered: there are perfect conductors. The second part of the definition was measured around two decades later. In 1933, Walther Meißner and Robert

---

[1]Ignoring the case of type II superconductors, which is not relevant for the current work.

[2]This section roughly follows [46].
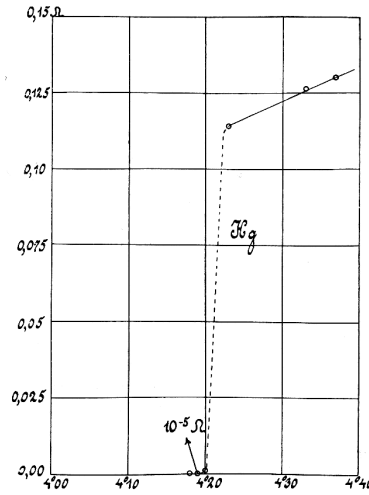
Figure 1: Measured temperature dependence of the resistivity of mercury at low temperatures by Heike Kamerlingh-Onnes in 1911. [49]

Ochsenfeld measured the behaviour of tin and lead superconductors in magnetic fields[52]. They found that the effects of superconductivity go beyond those just explainable by being a perfect conductor. When taking a superconductor and then applying a field, no magnetic field is entered. This is expected from perfect conductance, as currents are induced that cancel all fields. But, this is also true when cooling down the sample in a magnetic field. In this case, a simple perfect conductor would trap the field. Superconductors, on the other hand, expel the fields here as well, leading to the second part of their definition of being perfect diamagnets as well. The next big step in understanding superconductivity already followed in 1935, when Fritz and Heinz London proposed phenomenological equations to describe their properties[53]. Those were already capable of describing both electrical and magnetic properties of superconductors. It took another two decades, until a microscopic theory of superconductivity was developed.

2.1.2 Bardeen-Cooper-Schrieffer Theory

In this chapter, we discuss the Bardeen-Cooper-Schrieffer (BCS) theory introduced in the 1950s[54].[3] We start from a very general Hamiltonian in second quantization describing the electrons in a translational invariant case

---

[3]The following discussion closely follows [55] and also [46,56,57].

$$\hat{H} = \sum_{\boldsymbol{k},s} \varepsilon_k \, \hat{c}_{\boldsymbol{k}s}^\dagger \hat{c}_{\boldsymbol{k}s} + \sum_{\boldsymbol{k},\boldsymbol{k}'} \sum_{s,s'} V_{\boldsymbol{k};s,s'} \, \hat{c}_{\boldsymbol{k}s}^\dagger \hat{c}_{\boldsymbol{k}s'}$$
$$+ \sum_{\boldsymbol{k},\boldsymbol{k}'} \sum_{s,s'} W_{\boldsymbol{k},\boldsymbol{k}';s,s'} \, \hat{c}_{\boldsymbol{k}s}^\dagger \hat{c}_{-\boldsymbol{k}s'}^\dagger \hat{c}_{-\boldsymbol{k}'s'} \hat{c}_{\boldsymbol{k}'s} \tag{1}$$

$$V_{\boldsymbol{k};s,s'} \equiv \langle \boldsymbol{k};s | \hat{V} | \boldsymbol{k};s' \rangle \tag{2}$$

$$W_{\boldsymbol{k},\boldsymbol{k}';s,s'} \equiv \langle \boldsymbol{k},-\boldsymbol{k};s,s' | \hat{V} | \boldsymbol{k}',-\boldsymbol{k}';s,s' \rangle \tag{3}$$

$$\varepsilon_k \equiv \frac{k^2}{2m} - \mu \tag{4}$$

$$k \equiv |\boldsymbol{k}|, \tag{5}$$

where ε_k describes the kinetic term with mass m and chemical potential μ, $\hat{V}$ external potentials (e.g., magnetic or electric fields) and $\hat{W}$ the interaction between the electrons, typically mediated by phonons. We want to transform this into an effective single-particle Hamiltonian. This is currently prevented by the interaction term with four ladder operators.

As a simplification step, we apply a mean-field approximation, which describes the interactions by an effective background field. For general operators $\hat{A}$ and $\hat{B}$ we are interested in finding an approximation for their product $\hat{A}\hat{B}$. The main assumption is that they do not differ much from their expectation value, allowing us to neglect

$$(\hat{A} - \langle \hat{A} \rangle)(\hat{B} - \langle \hat{B} \rangle) \approx 0 \,. \tag{6}$$

Expanding this yields

$$(\hat{A} - \langle \hat{A} \rangle)(\hat{B} - \langle \hat{B} \rangle) = \hat{A}\hat{B} - \hat{A}\langle \hat{B} \rangle - \langle \hat{A} \rangle \hat{B} + \langle \hat{A} \rangle \langle \hat{B} \rangle \,. \tag{7}$$

Combining this with the assumption from above, we can simplify the operator product

$$\hat{A}\hat{B} = (\hat{A} - \langle \hat{A} \rangle)(\hat{B} - \langle \hat{B} \rangle) + \hat{A}\langle \hat{B} \rangle + \langle \hat{A} \rangle \hat{B} - \langle \hat{A} \rangle \langle \hat{B} \rangle$$
$$\approx \hat{A}\langle \hat{B} \rangle + \langle \hat{A} \rangle \hat{B} - \langle \hat{A} \rangle \langle \hat{B} \rangle \,. \tag{8}$$

Here we used that if both $\hat{A}$ and $\hat{B}$ are close to their median described by some small parameter δ, the first term scales as δ^2. Importantly, now every term on the right-hand-side has only terms with up to one operator. This means, that if $\hat{A}$ and $\hat{B}$ are linear in some operator, the right-hand-side is linear in it as well, despite the left-hand-side being quadratic. This allows us to reduce the quartic interaction part in Equation (1) to a quadratic term, and therefore a single particle potential, by choosing $\hat{A}$ and $\hat{B}$ appropriately[56]:

$$\underbrace{\hat{c}^\dagger_{ks}\hat{c}^\dagger_{-ks'}}_{\hat{A}}\underbrace{\hat{c}_{-k't}\hat{c}_{k't'}}_{\hat{B}} \approx \hat{c}^\dagger_{ks}\hat{c}^\dagger_{-ks'}\langle\hat{c}_{-k't}\hat{c}_{k't'}\rangle + \left\langle\hat{c}^\dagger_{ks}\hat{c}^\dagger_{-ks'}\right\rangle\hat{c}_{-k't}\hat{c}_{k't'}$$

$$-\left\langle\hat{c}^\dagger_{ks}\hat{c}^\dagger_{-ks'}\right\rangle\langle\hat{c}_{-k't}\hat{c}_{k't'}\rangle \qquad (9)$$

The last term is just a constant and can therefore be ignored in the Hamiltonian. We insert this into Equation (1) and obtain the effective single-particle Hamiltonian

$$
\begin{aligned}
\hat{H} &\approx \sum_{k,s}\varepsilon_k\,\hat{c}^\dagger_{ks}\hat{c}_{ks} + \sum_{k,k'}\sum_{s,s'}V_{k;s,s'}\,\hat{c}^\dagger_{ks}\hat{c}_{ks'} \\
&\quad + \sum_{k,k'}\sum_{s,s'}W_{k,k';s,s'}\left(\hat{c}^\dagger_{ks}\hat{c}^\dagger_{-ks'}\langle\hat{c}_{-k's'}\hat{c}_{k's}\rangle + \left\langle\hat{c}^\dagger_{ks}\hat{c}^\dagger_{-ks'}\right\rangle\hat{c}_{-k's'}\hat{c}_{k's}\right) \\
&\quad + \text{const} \\
&= \sum_{k,s}\varepsilon_k\,\hat{c}^\dagger_{ks}\hat{c}_{ks} + \sum_{k,k'}\sum_{s,s'}V_{k;s,s'}\,\hat{c}^\dagger_{ks}\hat{c}_{ks'} \\
&\quad + \sum_{k,k'}W_{k,k';s,s'}\langle\hat{c}_{-k's'}\hat{c}_{k's}\rangle\hat{c}^\dagger_{ks}\hat{c}^\dagger_{-ks'} \\
&\quad + \sum_{k,k'}W_{k',k;s,s'}\left\langle\hat{c}^\dagger_{k's}\hat{c}^\dagger_{-k's'}\right\rangle\hat{c}_{-ks'}\hat{c}_{ks} \\
&\quad + \text{const}\,. \qquad (10)
\end{aligned}
$$

From the hermiticity of the interaction potential we infer the following relation, that we can use to further simplify the Hamiltonian to

$$
\begin{aligned}
W_{k,k';s,s'} &\equiv \left\langle k',-k';s,s'\middle|\hat{W}\middle|k,-k;s,s'\right\rangle \\
&= \left\langle k,-k;s,s'\middle|\hat{W}\middle|k',-k';s,s'\right\rangle^* = W^*_{k',k;s,s'}\,. \qquad (11)
\end{aligned}
$$

This makes it possible for us to introduce a quantity Δ that turns out, like we will later see, to just be the superconducting gap:

$$\Delta_{k;s,s'} \equiv \sum_{k'}W_{k,k';s,s'}\langle\hat{c}_{-k's'}\hat{c}_{k's}\rangle \qquad (12)$$

All in all, we combine this and drop the constant term to arrive at the BCS Hamiltonian

$$\hat{H}_{\text{BdG}} = \sum_{\boldsymbol{k},s} \varepsilon_k \, \hat{c}^\dagger_{\boldsymbol{k}s} \hat{c}_{\boldsymbol{k}s} + \sum_{\boldsymbol{k},\boldsymbol{k}'} \sum_{s,s'} V_{\boldsymbol{k};s,s'} \, \hat{c}^\dagger_{\boldsymbol{k}s} \hat{c}_{\boldsymbol{k}s'}$$
$$+ \sum_{\boldsymbol{k}} \sum_{s,s'} \Delta_{\boldsymbol{k};s,s'} \hat{c}^\dagger_{\boldsymbol{k}s} \hat{c}^\dagger_{-\boldsymbol{k}s'} + \sum_{\boldsymbol{k}} \sum_{s,s'} \Delta^*_{\boldsymbol{k};s,s'} \hat{c}_{-\boldsymbol{k}s'} \hat{c}_{\boldsymbol{k}s} \,. \tag{13}$$

This Hamiltonian is also referred to as *BdG* Hamiltonian[58]. Note that the gap parameter Δ obeys the following symmetry due to the fermionic commutation relations of the ladder operators:

$$\Delta_{-\boldsymbol{k};s,s'} = \sum_{\boldsymbol{k}'} W_{-\boldsymbol{k},\boldsymbol{k}';s,s'} \langle \hat{c}_{-\boldsymbol{k}'s'} \hat{c}_{\boldsymbol{k}'s} \rangle = \sum_{\boldsymbol{k}'} W^*_{\boldsymbol{k},-\boldsymbol{k}';s,s'} \langle \hat{c}_{-\boldsymbol{k}'s'} \hat{c}_{\boldsymbol{k}'s} \rangle$$
$$= \sum_{\boldsymbol{k}'} W^*_{\boldsymbol{k},\boldsymbol{k}';s,s'} \langle \hat{c}_{\boldsymbol{k}'s'} \hat{c}_{-\boldsymbol{k}'s} \rangle = \left(\sum_{\boldsymbol{k}'} W_{\boldsymbol{k},\boldsymbol{k}';s,s'} \langle \hat{c}_{-\boldsymbol{k}'s} \hat{c}_{\boldsymbol{k}'s'} \rangle \right)^*$$
$$= \Delta^*_{\boldsymbol{k};s',s} \,. \tag{14}$$

In most parts of this work, we only have singlet s-wave pairing, meaning that it is independent of k and only pairing of spin-up with spin-down is happening, thus

$$\Delta_{\boldsymbol{k};s,s'} = \Delta \big(\mathrm{i}\bar{\Sigma}_y \big)_{s,s'} \,, \tag{15}$$

where $\bar{\Sigma}_y$ is the usual second Pauli matrix[4]. Furthermore, as global phases and vortices are irrelevant for this work, Δ is chosen to be real.

2.1.3 Nambu Spinors

Having obtained this effective single particle Hamiltonian, we now want to diagonalize it. So far, we described everything with a Hamiltonian consisting of terms composed of creation and annihilation operators. There is actually a very handy rephrasing of this Hamiltonian in terms of spinors (so called Nambu spinors), that results in a matrix form Hamiltonian[5]. We start by defining the spinor

---

[4]As $\bar{\sigma}_i$ is already taken in the community by 4×4 matrices that describe spin space, this unusual notation is chosen here.

[5]This discussion mostly follows [59], but with added consideration for spin dependent potentials.

$$\hat{\psi}_{\boldsymbol{k}} \equiv \begin{pmatrix} \hat{c}_{\boldsymbol{k}\uparrow} \\ \hat{c}_{\boldsymbol{k},\downarrow} \\ \hat{c}^{\dagger}_{-\boldsymbol{k}\downarrow} \\ -\hat{c}^{\dagger}_{-\boldsymbol{k},\uparrow} \end{pmatrix}. \tag{16}$$

Note the seemingly arbitrary minus sign in the 4th component and the reversed order of spins in the conjugated (therefore hole-) part of the vector. These are not the only possible choices, but will result later in a nicer form for the potentials. Different conventions can be found in various references, though. With this definition, we can rewrite Equation (13) in a matrix form:

$$\hat{H}_{\mathrm{BdG}} = \sum_{\boldsymbol{k}} \hat{\psi}^{\dagger}_{\boldsymbol{k}} \frac{1}{2} \begin{pmatrix} \varepsilon_k - V_{\boldsymbol{k};\uparrow,\uparrow} & V_{\boldsymbol{k};\uparrow,\downarrow} & \Delta_{\boldsymbol{k};\uparrow,\downarrow} & -\Delta_{\boldsymbol{k};\uparrow,\uparrow} \\ V_{\boldsymbol{k};\downarrow,\uparrow} & \varepsilon_k + V_{\boldsymbol{k};\downarrow,\downarrow} & \Delta_{\boldsymbol{k};\downarrow,\downarrow} & -\Delta_{\boldsymbol{k};\downarrow,\uparrow} \\ \Delta^{*}_{\boldsymbol{k};\uparrow,\downarrow} & \Delta^{*}_{\boldsymbol{k};\downarrow,\downarrow} & -\varepsilon_k - V_{-\boldsymbol{k};\uparrow,\uparrow} & V_{-\boldsymbol{k};\uparrow,\downarrow} \\ -\Delta^{*}_{\boldsymbol{k};\uparrow,\uparrow} & -\Delta^{*}_{\boldsymbol{k};\downarrow,\uparrow} & V_{-\boldsymbol{k};\downarrow,\uparrow} & -\varepsilon_k - V_{-\boldsymbol{k};\downarrow,\downarrow} \end{pmatrix} \hat{\psi}_{\boldsymbol{k}} \tag{17}$$

We introduce the Pauli matrices in spin space ($\bar{\sigma}_i \in \mathbb{C}^{4\times4}$) and particle-hole space ($\bar{\tau}_i \in \mathbb{C}^{4\times4}$)

$$\bar{\sigma}_i = \bar{\mathbb{1}}_2 \otimes \tilde{\sigma}_i \tag{18}$$

$$\bar{\tau}_i = \tilde{\sigma}_i \otimes \bar{\mathbb{1}}_2 \tag{19}$$

with the Kronecker product $\otimes$ and the usual Pauli matrices $\tilde{\sigma}_i \in \mathbb{C}^{2\times2}$. With leveraging time reversal symmetry, we assume $\Delta_{\boldsymbol{k};s,s'} = \Delta_{-\boldsymbol{k};s,s'}$[55] which leads us to $\Delta_{\boldsymbol{k};s,s'} = \Delta_{\boldsymbol{k};s',s}$. In this work, we are only interested in singlet superconductivity which means that we set $\Delta_{\boldsymbol{k};\uparrow,\uparrow} = \Delta_{\boldsymbol{k};\downarrow,\downarrow} = 0$ and just call $\Delta_{\boldsymbol{k};\uparrow,\downarrow} \equiv \Delta_{\boldsymbol{k}}$. With this, we rephrase the Hamiltonian in a matrix form:

$$\hat{H}_{\mathrm{BdG}} = \frac{1}{2} \sum_{\boldsymbol{k}} \hat{\psi}^{\dagger}_{\boldsymbol{k}} (\varepsilon_k \bar{\tau}_z + \Re(\Delta_{\boldsymbol{k}})\bar{\tau}_x + \Im(\Delta_{\boldsymbol{k}})\bar{\tau}_y + \bar{V})\hat{\psi}_{\boldsymbol{k}} \tag{20}$$

The interesting contributions to the potential $\bar{V}$ are Rashba and Zeeman terms. In the used matrix formalism, they can be expressed as follows:

$$\bar{V} = \boldsymbol{B} \cdot \boldsymbol{\sigma} - \alpha \hat{e}_z \cdot (\boldsymbol{k} \times \boldsymbol{\sigma})\bar{\tau}_z \tag{21}$$

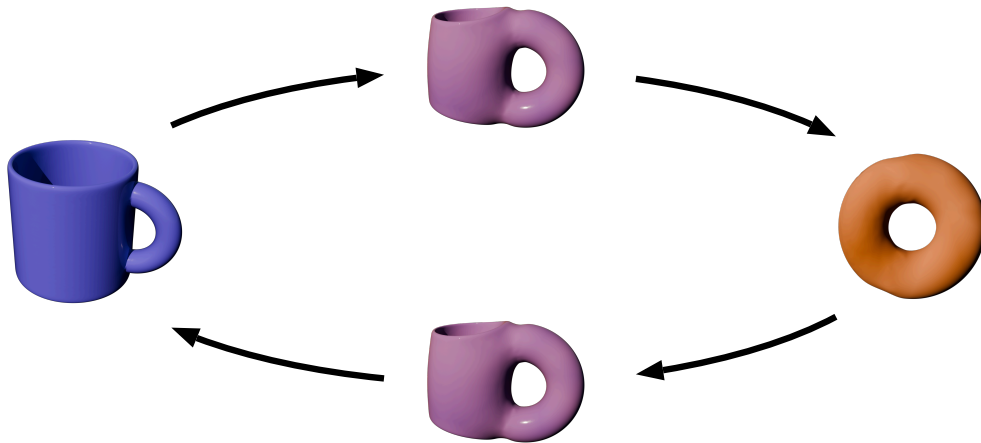$$\boldsymbol{\sigma} = \begin{pmatrix} \bar{\sigma}_x \\ \bar{\sigma}_y \\ \bar{\sigma}_z \end{pmatrix} \tag{22}$$

Figure 2: Schematic transformation of a cup into a donut and back.

Here $\boldsymbol{B}$ represents an external magnetic field and α the strength of the Rashba spin-orbit-coupling. Note that for simplicity, we discussed everything in Fourier space. For the later discussions we have to give this up as the field of a magnetic texture depends on location.

2.2 Topology

Topology is an area of mathematics that is concerned with *continuous* transformations. The most well known introductory example for this is the comparison of three-dimensional objects by comparing their number of holes. By this measure, for example, a Brezel and a t-shirt are *equivalent* as they have the same number of holes. Here, *continuous* means that any line that we can draw on the surface will stay intact during the transformation. Between a cup and a donut, such a transformation exists (see Figure 2), which is why they are *equivalent*.[6]

By applying this concept not to just those two objects, but any possible object, we can divide them into *classes*. Every pair of objects can be *continuously* transformed into each other if and only if they are in the same *class*. This is in of itself not that useful yet, as finding a concrete transformation is not a trivial task. But as it turns out, we can find a quantity (a *topological invariant*) that identifies the classes. Such a quantity for our previous example of three-dimensional

---

[6]See also the video in the supplementary data[60] or the flip-book in the corner.

Table 1: Topological classification of some real life objects by their number of holes. We ignore small pores, otherwise the sponge and t-shirt would be classified differently.

0 holes	1 hole	3 holes

objects turns out to be the number of holes. This is a better accessible quantity as counting holes is a much easier task than finding transformations. Often, one of the classes is called *trivial* in our example, the class of objects with no holes. The application of this concept to real-life objects can be seen in Table 1.

But, topology can not only be applied to geometrical objects in Euclidean space, but also more abstractly to other spaces. The integral part of topology is the definition of a continuous transformation. We will not give a rigorous mathematical introduction to topology, as this is not relevant for this work; the interested reader is referred to textbooks like Ref. [61]. In the following, we are going to see how topology can be applied in condensed matter physics.

2.2.1 Topology in Condensed Matter Physics

Topology can also be useful for describing and understanding condensed matter systems. A prominent example is the integer quantum Hall effect[7], which

---

[7]At the time of discovery, it was still described as quantum Hall effect (QHE). Only later, when the fractional quantum Hall effect (FQHE) was discovered, this distinction became important.
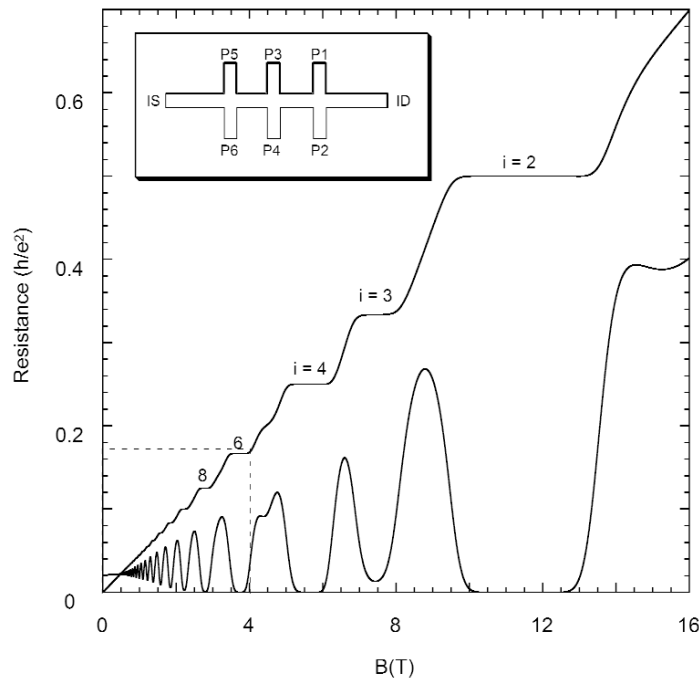
Figure 3: Measured transverse and longitudinal resistance of a quantum Hall device used as a resistance standard by the American standards organization NIST[65]. There are pronounced plateaus visible in the transverse resistance for integer filling values (here called i instead of ν) and peaks in the longitudinal resistance at transitions between those.

was discovered in 1980[62]. The discovery, later honoured with a Nobel Prize, showed, that the Hall conductivity σ_{xy} of a two-dimensional system takes quantized values at high magnetic fields and low temperatures

$$\sigma_{xy} = \frac{e^2 \nu}{2\pi\hbar},$$ (23)

where ν is called the filling factor and is an integer for the integer quantum Hall effect (IQHE).[8] See Figure 3 for experimental results from a more recent publication. This is substantially different from the classical expectation of a linear dependence of the conductance to the magnetic field. The quantized behaviour is very robust and precise, which is why this effect is nowadays utilized in resistance standards for device calibrations.

---

[8]For this historical overview, we follow Refs. [63] and [64].

Already one year after its discovery, Robert Laughlin did the first step towards finding a theoretical explanation of the IQHE by considering currents in a ring in a magnetic field[66]. Building on this, Bertrand Halperin showed a connection with the edge of the system[67], thus confirming its geometrical origin. This is also a strong hint to the topological nature of the problem. While most of the time in physics, a large but finite system can be approximated very well by an infinite system, this is no longer the case for topological effects because edge effects are essential and cannot be neglected any more.

The big breakthrough came, when David Thouless, Mahito Komoto, Peter Nightingale and Marcel den Nijs derived an explicit topological expression for the quantized Hall conductance[68]. Thouless received a Nobel Prize together with Micheal Kosterlitz as well, but for their earlier description of another topological effect[69]. This so called Berezinskii-Kosterlitz-Thouless (BKT) transition happens in some spin systems and describes a transition between a phase with vortex-anti-vortex pairs and a one with unpaired vortices and anti-vortices.

2.2.2 Gapped Hamiltonians

To transfer the concept of topology to condensed matter systems, we need to discuss what *continuous* transformations are in this case. The physical systems are described by a Hamiltonian $H(c_0, c_1, \ldots)$ depending on a set of parameters $\{c_i \mid i \in \mathbb{N}\}$. As a hermitian operator, it has a spectrum of real values, possibly with gaps. If we speak about *continuous* transformations, we mean smooth transformations of the parameters that neither open nor close a gap in the spectrum. Therefore, we can only apply this to gapped Hamiltonians.[9] This allows us then to categorize Hamiltonians into classes like described before, with the label *trivial* usually applied in a way such that the vacuum is trivial. For convenience, everything in the following is phrased in a way that the gap we are interested in is around *zero energy ($E = 0$)*.

---

[9]There are topological applications to gapless systems like Weyl semimetals. In these cases there is a local gap that leads to topological effects. Those systems are not relevant for the present work, so we do not discuss them in detail. The description of topology in magnets also works differently.
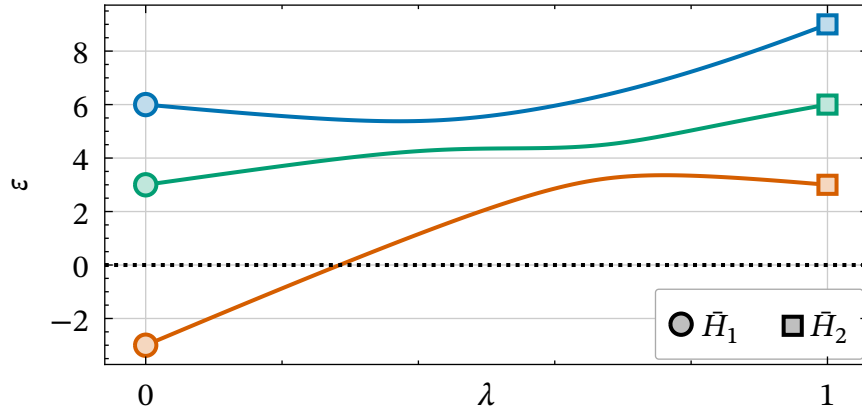
Figure 4: Spectrum of the Hamiltonian $\bar{H}(\lambda)$ interpolating between $\bar{H}_1$ and $\bar{H}_2$. The lowest eigenvalue necessarily crosses zero, placing them into different topological classes.

So far, this explanation is rather abstract, so let us follow through with an example[10]. We start with two Hamiltonians represented by matrices $\bar{H}_1$ and $\bar{H}_2$ and corresponding eigenvalues $\varepsilon_{i,j}$.

$$\bar{H}_1 = \begin{pmatrix} 4 & -1 & -1 \\ -1 & 1 & 4 \\ -1 & 4 & 1 \end{pmatrix} \qquad \bar{H}_2 = \begin{pmatrix} 6.5 & 2 & -0.5 \\ 2 & 5 & -2 \\ -0.5 & -2 & 6.5 \end{pmatrix} \tag{24}$$

$$\varepsilon_{1,1\ldots3} = 6, 3, -3 \qquad \varepsilon_{2,1\ldots3} = 9, 6, 3. \tag{25}$$

While these are completely arbitrary, we can still examine their topology. The question arises, whether they are topologically equivalent or not. Or in other words, is there *any* continuous transformation from $\bar{H}_1$ to $\bar{H}_2$ such that no eigenvalue crossed zero? Consider the following path that connects the two Hamiltonians

$$\bar{H}(\lambda) = \bar{H}_1 + \lambda(\bar{H}_2 - \bar{H}_1), \lambda \in [0, 1] \tag{26}$$
$$\bar{H}(0) = \bar{H}_1 \quad \bar{H}(1) = \bar{H}_2.$$

This linearly interpolates between the two Hamiltonians and its eigenvalues smoothly transform from those of $\bar{H}_1$ to those of $\bar{H}_2$. This evolution is shown in Figure 4. Clearly, this path closes the gap. But, importantly, this does not automatically mean that the two Hamiltonians are not in the same class. For this to be true, *all* paths have to close the gap.

---

[10]This part roughly follows[70].

Luckily, in this case, this can be shown in a straightforward way by looking at the number of negative (or positive) eigenvalues. $\bar{H}_1$ has a single negative eigenvalue, while $\bar{H}_2$ has none. Therefore, to transform one into the other, we somehow have to bring this one eigenvalue up on the other side of 0. There is no continuous way to do this without crossing 0 at some point. This means that there indeed *cannot* be any continuous transformation between the two Hamiltonians without crossing zero, placing them in two different topological classes.

We also touched another important concept here. By counting the number of negative eigenvalues, we discovered the concept of a *topological invariant*. This is an identifier which uniquely labels each class. *Unique* means here, that each class gets a unique label, but not that the lable scheme is unique. This is visible in our example as we could as well have chosen the number of positive values, twice the number of negative values or many other quantities. Here, the invariant is a natural number, but we will encounter other kinds of invariants later.

Moreover, looking at $\bar{H}(\lambda)$, we see a *topological phase transition* happening here. By changing the parameter λ, we go from one topological class to another. In physical systems, this parameter can be given by a large range of physical quantities, for example an external magnetic field.

2.2.3 Topological Superconductors

As we have seen now, topological concepts can be applied to condensed systems that have a gap in their spectrum, namely insulators or superconductors. In the following we will only consider superconductors as they are relevant for this thesis. In general, the concepts can and have been applied to insulators as well, though[71–73]. We give an overview of the concepts and ideas. For an in-depth introduction, have a look at the course in Ref. [70].

Kitaev Wire

The simplest example of a superconducting system that shows topological behaviour is the Kitaev wire. It consists of a one-dimensional spinless *p*-wave superconductor and is described by

$$\hat{H}_{\text{Kitaev}} = \sum_{\boldsymbol{k}} \hat{\boldsymbol{\varphi}}_{\boldsymbol{k}} \bar{h} \hat{\boldsymbol{\varphi}}_{\boldsymbol{k}}^{\dagger} \tag{27}$$

$$\bar{h} = \begin{pmatrix} \frac{k^2}{2m} - \mu & \Delta^* k \\ \Delta k & -\frac{k^2}{2m} + \mu \end{pmatrix} \tag{28}$$

$$\hat{\varphi} = \begin{pmatrix} \varphi_k \\ \varphi_{-k}^{\dagger} \end{pmatrix} \tag{29}$$

with the mass $m > 0$, the chemical potential μ and the superconducting gap Δ as parameters. Compared to the previous section where the Nambu basis consisted of four components (Equation (16)), we now only have two. This is due to the spinlessness of the model. This is not realistic, as electrons do have spin. We later discuss how one can map a more realistic model onto this. This cannot be done by just doubling the model and taking spin up and down separately, as then we would get pairs of states.

This Hamiltonian has eigenvalues

$$E_k = \pm\sqrt{\left(\frac{k^2}{2m} - \mu\right)^2 + k^2 |\Delta|^2} \tag{30}$$

resulting in a gap at $k = 0$ of $E_{\text{g}} = |\mu|$ that closes when the chemical potential vanishes ($\mu = 0$). This means that there is no way to continuously change parameters from a set of values with $\mu > 0$ to another set of values with $\mu < 0$ without closing the gap. Therefore, we can group the possible Hamiltonians in exactly two classes ($\mu > 0$ and $\mu < 0$).

2.2.4 Influence of Symmetries

We can get a lot of insight into the topology of a system by looking at its symmetries. The symmetries together with the number of dimensions define the kind of topological invariant the system possesses. This has been in discussed in Refs. [74–76]. Those works approach the discussion from the viewpoint of group theory. Here we give an introduction more similar to the one in [70] by starting from the symmetries. This is a more pedagogical and less mathematically exhaustive discussion. For example, we give no proof here that the presented set of symmetries is completely exhaustive.

According to Wigner's theorem[77], symmetries can only be represented by *unitary* or *antiunitary* operators that *commute* with the Hamiltonian. This is deduced from requiring the probability to be conserved. For superconductors in the BdG formalism, this is not exhaustive though, as we can also have symmetries[11] that are represented by operators, that *anti-commute* with the Hamiltonian. This is made possible by the fact that we have the artificial doubling of the space and have pairs of eigenstates with energies with opposite sign.

Not all symmetries are relevant for the topological properties. If the superconductor possesses some unitary symmetry represented by a matrix $\bar{U}$, we can rewrite the matrix in block diagonal form. We can then perform the topology analysis on each block separately and just get the invariant of the whole system by adding those of the blocks. Therefore, nothing interesting topology-wise happens. In the following, we assume that this step has already been carried out and are looking at a block of this new block matrix[12].

This leaves as with non-unitary symmetries. We have multiple options to build these. For superconductors, the relevant ones are time-reversal (TRS), particle-hole (PHS), and chiral (CS) symmetry, where the last one is a combination of the first two.

Time-Reversal Symmetry

TRS is represented by an *antiunitary* operator $\hat{\mathcal{T}}$ that *commutes* with the Hamiltonian. Antiunitary means, that it is a combination of a unitary operator, combined with complex conjugation $\hat{\mathcal{K}}$. This complex conjugation is meant to be in real-space, thus in momentum space we additionally need to invert the momentum. Therefore, we have

$$\hat{\mathcal{T}} \equiv \bar{U}_T \hat{\mathcal{K}} \tag{31}$$

$$\hat{H}(-\boldsymbol{k}) = \hat{\mathcal{T}} \hat{H}(\boldsymbol{k}) \hat{\mathcal{T}}^{-1} = \bar{U}_T \hat{H}^*(\boldsymbol{k}) \bar{U}_T^\dagger. \tag{32}$$

Very importantly, as this is not a linear operator, $\hat{\mathcal{T}}$ does not commute with scalars. More concretely, we have $\{\hat{\mathcal{T}}, \mathrm{i}\} = 0$. Now we make the, for now seemingly arbitrary, step of applying this transformation twice and obtain

---

[11]Some authors also call these pseudosymmetries.

[12]Ref. [78] discusses a way to do this algorithmically.

$$\hat{H}(\boldsymbol{k}) = \hat{\mathcal{T}}^2 \hat{H}(\boldsymbol{k})\hat{\mathcal{T}}^{-2} = \underbrace{\left(\bar{U}_T \bar{U}_T^*\right)}_{\bar{U}_2}\hat{H}(\boldsymbol{k})\left(\bar{U}_T \bar{U}_T^2\right)^\dagger \equiv \bar{U}_2 \hat{H}(\boldsymbol{k})\bar{U}_2^\dagger \qquad (33)$$

$$\Rightarrow \hat{\mathcal{T}}^2 = \bar{U}_2 \, . \qquad (34)$$

This new matrix $\bar{U}_2$ is also unitary and, as can be seen here, commutes with the Hamiltonian. But, as we are working on a block of the matrix after all unitary symmetries are already dealt with, the only remaining option is a simple scalar multiplication. This is not the final result yet, though, as we can apply a similar trick to before. We go one power higher in $\hat{\mathcal{T}}$ and calculate $\hat{\mathcal{T}}^3$. With this, we obtain

$$\hat{\mathcal{T}}^2 = \bar{U}_2 = e^{i\varphi}\bar{\mathbb{1}} \qquad (35)$$
$$\hat{\mathcal{T}}^3 = \hat{\mathcal{T}}\hat{\mathcal{T}}^2 = \hat{\mathcal{T}}^2\hat{\mathcal{T}}$$
$$= \hat{\mathcal{T}}e^{i\varphi} = e^{i\varphi}\hat{\mathcal{T}}$$
$$= e^{-i\varphi}\hat{\mathcal{T}} = e^{i\varphi}\hat{\mathcal{T}}$$
$$\Rightarrow e^{i\varphi} = \pm 1, \quad \hat{\mathcal{T}}^2 = \pm\bar{\mathbb{1}} \, . \qquad (36)$$

Here we used that fact that, if it holds for a complex number $z \in \mathcal{C}$ that $z = z^*$, it has to be real. And the only real numbers of magnitude 1 are ± 1. Therefore, we can have two kinds of realisations of time reversal symmetry, which can be distinguished by the sign of $\hat{\mathcal{T}}^2$. The proof that these indeed belong to different symmetry classes goes beyond the scope of this work, but is discussed in the original works[74–76].

Particle-Hole Symmetry

PHS is also an *antiunitary* symmetry, but one that is represented by an operator $\hat{\mathcal{C}}$, that *anti-commutes* with the Hamiltonian. Like any antiunitary operator, it can be written as a combination of a unitary matrix and complex conjugation. Therefore, it is defined by

$$\hat{\mathcal{C}} \equiv \bar{U}_C \hat{\mathcal{K}} \qquad (37)$$
$$\hat{H}(-\boldsymbol{k}) = -\hat{\mathcal{C}}\hat{H}(\boldsymbol{k})\hat{\mathcal{C}}^{-1} = -\bar{U}_C \hat{H}^*(\boldsymbol{k})\bar{U}_C^\dagger \, . \qquad (38)$$

The same procedure we did to analyse possible TRS realisations can also be applied to PHS. Thus, PHS as well can only by found in flavours of $\hat{\mathcal{C}} = \pm 1$.

Chiral Symmetry

The combination of TRS and PHS is called chiral symmetry. As a combination of an *antiunitary commuting* and an *antiunitary anti-commuting* symmetry, it is represented by a *unitary* operator $\hat{S}$ that *anti-commutes* with the Hamiltonian. Thus, we have

$$\hat{S} \equiv \bar{U}_S = \hat{C}\hat{T} = \bar{U}_C \bar{U}_T^* \tag{39}$$

$$\hat{H}(\boldsymbol{k}) = -\hat{S}\hat{H}(\boldsymbol{k})\hat{S}^{-1}. \tag{40}$$

It might look like this wouldn't add any additional information, as we already looked at the two components. But there is also the possibility that the Hamiltonian obeys CS without having TRS or PHS. Similar to before, we can conclude, that $\hat{S}^2$ can only be a multiplication with a complex phase $e^{i\varphi_S}$. But unlike before, $\hat{S}$ is a unitary operator and therefore any phase can be absorbed into the operator. For simplicity, we arbitrarily fix $\hat{S}^2 = 1$. Ergo, there is only one kind of CS.

Putting Everything Together

Having discussed all the three relevant symmetries, we can put everything together. Summarizing and repeating the previous definitions, we have

$$\hat{H}(-\boldsymbol{k}) = \hat{T}\hat{H}(\boldsymbol{k})\hat{T}^{-1}, \quad \hat{T} \equiv \bar{U}_T\hat{K}, \quad \hat{T}^2 = \pm 1 \tag{41}$$

$$\hat{H}(-\boldsymbol{k}) = -\hat{C}\hat{H}(\boldsymbol{k})\hat{C}^{-1}, \quad \hat{C} \equiv \bar{U}_C\hat{K}, \quad \hat{C}^2 = \pm 1 \tag{42}$$

$$\hat{H}(\boldsymbol{k}) = -\hat{S}\hat{H}(\boldsymbol{k})\hat{S}^{-1}, \quad \hat{S} \equiv \bar{U}_S = \hat{C}\hat{T}, \quad \hat{S}^2 = 1. \tag{43}$$

Now, we can count the possible combinations of the possible symmetries. TRS and PHS can each be not present, have a positive sign and have a negative sign in Equation (41), leaving us with 3 options each. It is also possible for a system to have CS, even if neither TRS nor PHS is present, therefore giving us 2 classes without TRS and PHS. All the resulting 10 classes are summarized in Table 2 together with the name of their symmetry class. The names are tied to the names of the underlying mathematical Cartan symmetry classes. A discussion of their relation would go too far here, but for interested and mathematically inclined readers can be found in Ref. [74].

Table 2: Symmetry classes according to the tenfold way with their corresponding signs.[74] The sign corresponds to the sign in Equation (41) and a 0 signifies that the symmetry is not present. The right-most two columns show the kind of invariant in one and two dimensions[79].[13] $\mathbb{Z}_2$ means a whole number, but only two possible values (for example the sign of a quantity), and $2\mathbb{Z}$ corresponds to an even number.

class	TRS	PHS	CS	$1d$	$2d$
A	0	0	0	–	$\mathbb{Z}$
AI	+	0	0	–	–
AII	–	0	0	–	$\mathbb{Z}_2$
AIII	0	0	+	$\mathbb{Z}$	–
BDI	+	+	+	$\mathbb{Z}$	–
C	0	–	0	–	$2\mathbb{Z}$
CI	+	–	+	–	–
CII	–	–	+	$2\mathbb{Z}$	–
D	0	+	0	$\mathbb{Z}_2$	$\mathbb{Z}$
DIII	–	+	+	$\mathbb{Z}_2$	$\mathbb{Z}_2$

Let us apply this now to Hamiltonians in BdG form from Equation (20). By construction we have a PHS symmetry because there are pairs of eigenstates with opposite energy. The corresponding operator is

$$\hat{\mathcal{C}} = \bar{\tau}_y \bar{\sigma}_y \hat{\mathcal{K}} \tag{44}$$

$$\hat{\mathcal{C}}^2 = \bar{\mathbb{1}}_4 . \tag{45}$$

This means that we are in the group of classes D (no other symmetry), BDI (TRS with sign +) and DIII (TRS with sign −). Which one of these is the correct one depends on the choice of potential and gap.

One essential insight that we get from the classification is the kind of invariant we have in the system. In Table 2, the values the invariant can take in one and two dimensions are listed[79].

---

[13]All classes are topological, just not necessarily in one or two dimensions.
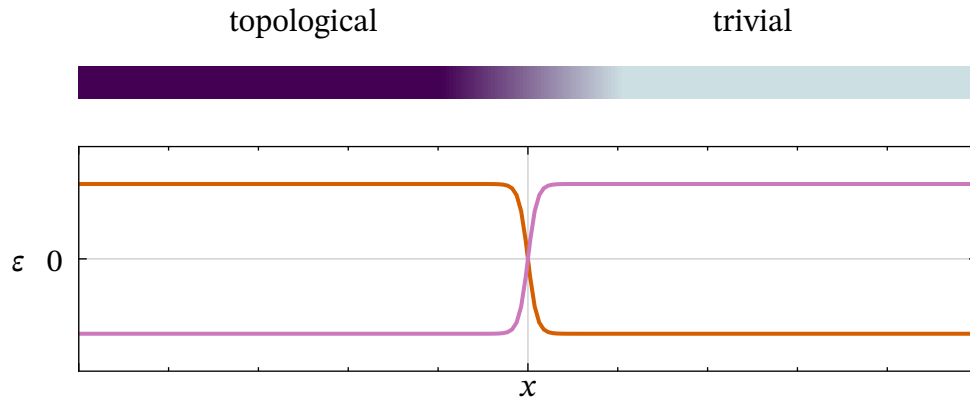
Figure 5: Boundary between a topological (left) and trivial (right) region in a one-dimensional wire. The local spectra on both sides are indistinguishable, but the states are essentially swapped. This requires the energies to locally crossover and close the gap.

2.2.5 Bulk-Edge Correspondence

The topological properties we discussed so far were *bulk* quantities. This means that they are associated with the Hamiltonian of an infinite translational invariant system. For most physical problems, an infinite system is a good approximation and a large but finite system behaves basically the same as an infinite one.

This is not the case any more for topological systems, where the boundaries are essential. Let us assume that we are in one-dimension and have a two-state Hamiltonian. To see the effect of the topology, we put a boundary into the system where the spectrum on both sides is the same, but the topology is different (see Figure 5). Their topology being different means that the only way to transform them into each other is by some transformation that closes the gap. Therefore, in the boundary region, the energies somewhere have to somewhere cross zero. This leads to a bound state, which is localised at the edge and has zero energy. As we defined trivially before as being topologically equivalent, this means that these edge states also appear on the edges of topological samples.

In consequence, there is behaviour at the edges of regions, which is a result of the bulk topology. This concept is called *bulk-edge correspondence*. While we made a one-dimensional example, this concept holds true in any number of

dimensions. But in higher dimensions, the edge state also is of higher dimension and thus not a single zero-energy state any more, but rather a band that crosses zero.

Because the origin of these edge states is the bulk topology, they are very robust. To make them vanish, one would need to change the topology of the bulk, which is protected by the existence of the gap.

2.2.6 Majorana States

As we have seen in Section 2.1, superconducting systems have a PHS by construction that results in eigenstates to come in pairs with opposite energy. This makes them suitable to host so called Majorana states, which refer to the concept of Majorana fermions.

Majorana fermions are real fermions compared to the more usual complex — or Dirac — fermions like electrons. They were proposed by Ettore Majorana in 1937[12]. In second quantization, Dirac fermions are described by creation and annihilation operators $\hat{a}^\dagger$ and $\hat{a}$ which obey the anti-commutator relations

$$\left\{\hat{a}_i, \hat{a}_j^\dagger\right\} = \delta_{i,j} \tag{46}$$

$$\{\hat{a}_i, \hat{a}_j\} = \left\{\hat{a}_i^\dagger, \hat{a}_j^\dagger\right\} = 0 \tag{47}$$

with the Kronecker delta $\delta_{i,j}$. They are called complex, as the hermitian conjugate plays the same role as the complex conjugation for complex numbers. From these anti-commutation rules, it follows, that many-particle states of Dirac fermions are *antisymmetric* regarding permutation. This means, that swapping two Dirac fermions causes the wave function to obtain a global phase of π. We can see this from Equation (47) and obtain with the ground state $|0\rangle$ which has no particles

$$|i, j\rangle \equiv \hat{a}_j^\dagger \hat{a}_i^\dagger |0\rangle = -\hat{a}_i^\dagger \hat{a}_j^\dagger |0\rangle = -|j, i\rangle. \tag{48}$$

Majorana fermions work in a very similar way, but with the added feature of being *real*. In this context, this means that their creation and annihilation operators are identical. This means, the Majorana fermion is described with a single ladder operator $\hat{\gamma}$. Analogous to complex numbers, we can also write every Dirac fermion in terms of a real and imaginary part by expressing the Dirac operator with two Majorana operators as

$$\hat{a}^\dagger \equiv \frac{1}{\sqrt{2}}(\hat{\gamma}_1 + i\hat{\gamma}_2) \tag{49}$$

$$\hat{a} \equiv \frac{1}{\sqrt{2}}(\hat{\gamma}_1 - i\hat{\gamma}_2) \tag{50}$$

$$\hat{\gamma}_1 = \frac{1}{\sqrt{2}}(\hat{a} + \hat{a}^\dagger) \tag{51}$$

$$\hat{\gamma}_2 = \frac{i}{\sqrt{2}}(\hat{a} - \hat{a}^\dagger). \tag{52}$$

From the complex fermion anti-commutator, we can also infer the Majorana anti-commutator for the Majorana operators. This yields

$$\{\hat{\gamma}_1, \hat{\gamma}_2\} = \frac{i}{2}\{\hat{a} + \hat{a}^\dagger, \hat{a} - \hat{a}^\dagger\}$$
$$= \frac{i}{2}\Big(\underbrace{\{\hat{a}, \hat{a}\}}_{0} + \underbrace{\{\hat{a}^\dagger, \hat{a}\}}_{1} - \underbrace{\{\hat{a}, \hat{a}^\dagger\}}_{1} - \underbrace{\{\hat{a}^\dagger, \hat{a}^\dagger\}}_{0}\Big) = 0 \tag{53}$$

$$\{\hat{\gamma}_1, \hat{\gamma}_1\} = \frac{1}{2}\{\hat{a} + \hat{a}^\dagger, \hat{a} + \hat{a}^\dagger\}$$
$$= \frac{1}{2}\Big(\underbrace{\{\hat{a}, \hat{a}\}}_{0} + \underbrace{\{\hat{a}^\dagger, \hat{a}\}}_{1} + \underbrace{\{\hat{a}, \hat{a}^\dagger\}}_{1} + \underbrace{\{\hat{a}^\dagger, \hat{a}^\dagger\}}_{0}\Big) = 1 \tag{54}$$

$$\{\hat{\gamma}_2, \hat{\gamma}_2\} = -\frac{1}{2}\{\hat{a} - \hat{a}^\dagger, \hat{a} - \hat{a}^\dagger\}$$
$$= -\frac{1}{2}\Big(\underbrace{\{\hat{a}, \hat{a}\}}_{0} - \underbrace{\{\hat{a}^\dagger, \hat{a}\}}_{1} - \underbrace{\{\hat{a}, \hat{a}^\dagger\}}_{1} + \underbrace{\{\hat{a}^\dagger, \hat{a}^\dagger\}}_{0}\Big) = 1 \tag{55}$$

$$\Rightarrow \{\hat{\gamma}_i, \hat{\gamma}_j\} = \delta_{i,j}. \tag{56}$$

Consequently, all pairs of different Majorana operators anti-commute. So far, we only generically discussed fermionic operators, but we can transfer this concept to topological superconductors[14]. Let us assume that we have some eigenstate $\psi_+(r)$ with energy ε which has the components

$$\psi_+(r) \equiv \begin{pmatrix} u_\uparrow(r) \\ u_\downarrow(r) \\ v_\downarrow(r) \\ -v_\uparrow(r) \end{pmatrix}. \tag{57}$$

We know that there is a partner state $\psi_-(r)$ with energy $-\varepsilon$ which is connected to $\psi_+(r)$ by the PHS

$$\psi_-(\boldsymbol{r}) = \hat{\mathcal{C}}\psi_+(\boldsymbol{r}) = \begin{pmatrix} v_\uparrow^*(\boldsymbol{r}) \\ v_\downarrow^*(\boldsymbol{r}) \\ u_\downarrow^*(\boldsymbol{r}) \\ -u_\uparrow^*(\boldsymbol{r}) \end{pmatrix}. \tag{58}$$

For a state at zero energy, the situation is more specific. Due to the two states of the pair having the same energy in this case, the space is degenerate. We know therefore that then up to an arbitrary phase that we set to zero for simplicity, they are the same[14], and thus we have for $\sigma \in \{\uparrow, \downarrow\}$

$$v_\sigma(\boldsymbol{r}) = u_\sigma^*. \tag{59}$$

This means that we can build two Majorana wave functions $\varphi_{\sigma,i}(\boldsymbol{r})$ per spin σ out of the state pair at zero energy with

$$\varphi_{\sigma,1}(\boldsymbol{r}) \equiv \frac{1}{\sqrt{2}}(u_\sigma(\boldsymbol{r}) + u_\sigma^*(\boldsymbol{r})) \tag{60}$$

$$\varphi_{\sigma,2}(\boldsymbol{r}) \equiv \frac{i}{\sqrt{2}}(u_\sigma(\boldsymbol{r}) - u_\sigma^*(\boldsymbol{r})) \tag{61}$$

or in vector form with

$$\varphi(\boldsymbol{r}) = \bar{U}\psi_+(\boldsymbol{r}) = \frac{1}{2}\begin{pmatrix} u_\uparrow(\boldsymbol{r}) + u_\uparrow^*(\boldsymbol{r}) \\ u_\downarrow(\boldsymbol{r}) + u_\downarrow^*(\boldsymbol{r}) \\ i(u_\uparrow(\boldsymbol{r}) - u_\uparrow^*(\boldsymbol{r})) \\ i(u_\downarrow(\boldsymbol{r}) - u_\downarrow^*(\boldsymbol{r})) \end{pmatrix} = \begin{pmatrix} \varphi_{\uparrow,1}(\boldsymbol{r}) \\ \varphi_{\downarrow,1}(\boldsymbol{r}) \\ \varphi_{\uparrow,2}(\boldsymbol{r}) \\ \varphi_{\downarrow,2}(\boldsymbol{r}) \end{pmatrix} \tag{62}$$

$$\bar{U} \equiv \frac{1}{2}\begin{pmatrix} 1 & 0 & 0 & -1 \\ 0 & 1 & 1 & 0 \\ i & 0 & 0 & i \\ 0 & i & -i & 0 \end{pmatrix}. \tag{63}$$

Therefore, the topological edge states we encountered in the last section have Majorana character.

2.2.7 Braiding and Computation

While studying quasi-particles with Majorana character in itself can be interesting, the actual importance of MBSes comes from their usage for quantum computing[6,7]. For this, their topological protection would provide an advan-
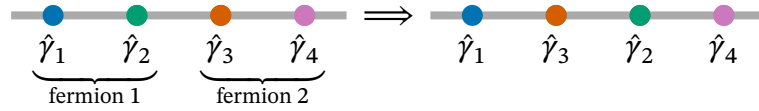
Figure 6: Exchange of two Majoranas in a chain of two fermions.

tage for reducing error rates and increasing stability[6]. This type of quantum computing is called *topological quantum computing*.[14]

To make MBSes usable for quantum computing, we need a way to define operations. As we cannot create and annihilate single Majoranas, this base is not suitable for defining a qubit. We can make use of their statistical properties. Because MBSes are not elemental particles, they do not need to fall into the classification of fermionic and bosonic exchange statistics. In fact, in the following we are going to see that their exchange statistic is *non-abelian*, which means that the order of exchanges is important. Fermions follow *abelian* statistics. This means, if we take two many-particle states which differ only by a permutation of the particles, it does not matter which path we take in between. For example, we always have

$$|2, 1, 3\rangle = -|1, 2, 3\rangle \tag{64}$$

regardless of which permutation path we take between them.

For MBSes, the situation is different. Let us look now a chain of two fermions and therefore four Majoranas (see Figure 6). We want to exchange the middle two Majoranas. Note that, to do this, we need to at least temporarily introduce a second dimension. But for the present discussion, it does not matter how we do this, so we skip over this step. We also assume that this exchange happens adiabatic, meaning that we do it slow enough to prevent exitations to higher energy. In other words, the full braiding process happens fully in the manifold of states around zero energy. This is consisting of $4 = 2^2$ of states[15] because of the two fermions. In general, the size of this space is given by 2^N where N is the number of fermions. We can write down an orthogonal base of this space with occupation numbers as $\{|0\rangle, |01\rangle, |10\rangle, |10\rangle\}$. The first digit denotes the occupation of the first and the second one of the second fermion. Therefore we have

---

[14]This part again follows [70].

[15]When counting here, we ignore the PHS partner states.

$$|10\rangle = \hat{a}_1^\dagger |00\rangle \tag{65}$$

$$|01\rangle = \hat{a}_2^\dagger |00\rangle \tag{66}$$

$$|11\rangle = \hat{a}_1^\dagger \hat{a}_2^\dagger |00\rangle. \tag{67}$$

In general, any evolution like this in quantum mechanics is described by a unitary transformation. To make the calculations simpler, we write this in a space of vectors

$$|\psi\rangle = \sum_{i,j} a_{ij} |ij\rangle \tag{68}$$

$$\psi \equiv \begin{pmatrix} a_{00} \\ a_{10} \\ a_{01} \\ a_{11} \end{pmatrix}. \tag{69}$$

This means that the process of exchanging the middle two Majoranas can be represented by a unitary matrix $\bar{U}_{23}$. We present the Majorana operators as matrices. For this, it is educational to first represent the fermionic operators in this base, which yields[16]

$$\bar{a}_1^\dagger = \begin{pmatrix} 0 & 0 & 0 & 0 \\ 1 & 0 & 0 & 0 \\ 0 & 0 & 0 & 0 \\ 0 & 0 & 1 & 0 \end{pmatrix} \tag{70}$$

$$\bar{a}_2^\dagger = \begin{pmatrix} 0 & 0 & 0 & 0 \\ 0 & 0 & 0 & 0 \\ 1 & 0 & 0 & 0 \\ 0 & -1 & 0 & 0 \end{pmatrix}. \tag{71}$$

From those, we construct the Majorana operators

---

[16]Note the minus sign in $\bar{a}_2^\dagger$, because $\bar{a}_2^\dagger |10\rangle = \bar{a}_2^\dagger \bar{a}_1^\dagger |00\rangle = -|11\rangle$.

$$\bar{\gamma}_1 = \frac{1}{\sqrt{2}}\left(\bar{a}_1 + \bar{a}_1^\dagger\right) = \frac{1}{\sqrt{2}}\begin{pmatrix} 0 & 1 & 0 & 0 \\ 1 & 0 & 0 & 0 \\ 0 & 0 & 0 & 1 \\ 0 & 0 & 1 & 0 \end{pmatrix} \tag{72}$$

$$\bar{\gamma}_2 = \frac{i}{\sqrt{2}}\left(\bar{a}_1 - \bar{a}_1^\dagger\right) = \frac{i}{\sqrt{2}}\begin{pmatrix} 0 & 1 & 0 & 0 \\ -1 & 0 & 0 & 0 \\ 0 & 0 & 0 & 1 \\ 0 & 0 & -1 & 0 \end{pmatrix} \tag{73}$$

$$\bar{\gamma}_3 = \frac{1}{\sqrt{2}}\left(\bar{a}_2 + \bar{a}_2^\dagger\right) = \frac{1}{\sqrt{2}}\begin{pmatrix} 0 & 0 & 1 & 0 \\ 0 & 0 & 0 & -1 \\ 1 & 0 & 0 & 0 \\ 0 & -1 & 0 & 0 \end{pmatrix} \tag{74}$$

$$\bar{\gamma}_4 = \frac{i}{\sqrt{2}}\left(\bar{a}_2 - \bar{a}_2^\dagger\right) = \frac{i}{\sqrt{2}}\begin{pmatrix} 0 & 0 & 1 & 0 \\ 0 & 0 & 0 & -1 \\ -1 & 0 & 0 & 0 \\ 0 & 1 & 0 & 0 \end{pmatrix}. \tag{75}$$

Every unitary matrix can be written as $\exp(i\bar{O})$ with a Hermitian matrix $\bar{O}$. It is reasonable to assume that the transformation only affects the Majoranas involved in the braiding process. And as we cannot operate with single Majoranas, it has to depend on the product of both[70]. With that we can write

$$\bar{U}_{23} = \exp(2\varphi\bar{\gamma}_2\bar{\gamma}_3) = \bar{\mathbb{1}}_2\cos(\varphi) + \bar{\gamma}_2\bar{\gamma}_3\sin(\varphi). \tag{76}$$

Because we swapped the two Majoranas, $\bar{\gamma}_2$ after the braid needs to be acting like $\bar{\gamma}_3$ before and vice versa. Consequently, we can calculate the angle φ from that with

$$\bar{\gamma}_2 = e^{i\beta}\bar{U}_{23}\bar{\gamma}_3\bar{U}_{23}^\dagger \tag{77}$$

where $\beta \in \mathbb{R}$ is an arbitrary phase. We could do the same with $\bar{\gamma}_2$ and $\bar{\gamma}_3$ reversed, but that would only give a redundant equation. With the ansatz for $\bar{U}_{23}$ from above, the remaining equations to solve are

$$\cos(2\varphi) = 0 \tag{78}$$
$$\sin(2\varphi) = e^{i\beta} \tag{79}$$

which is solved by

$$\varphi = \pm\frac{\pi}{4} \tag{80}$$

$$\beta = \pi \tag{81}$$

$$\Rightarrow \bar{U}_{23} = \exp\!\left(\pm\frac{\pi}{4}\bar{\gamma}_2\bar{\gamma}_3\right). \tag{82}$$

In fact, this procedure works for exchanging any pair of Majoranas and any size of chain so we have

$$\bar{U}_{nm} = \exp\!\left(\pm\frac{\pi}{4}\bar{\gamma}_n\bar{\gamma}_m\right). \tag{83}$$

The main takeaways here are, that there are two solutions and as well that these matrices do not commute for different pairs of Majoranas. The two solutions correspond to clockwise and counterclockwise braiding of the two Majoranas and the non-commutivity is what makes them *non-abelian*. It can be shown, that it is possible to design a universal quantum computer with just braiding operations on the Majoranas[80].

2.3 Micromagnetics

In this section, we discuss some basic principles of magnetic systems that are necessary to understand the formation of the domain walls. Before going into the details of the domain wall formation as discussed in Ref. [81], we introduce the general formalism. As we are interested in small-scale textures that are still significantly larger than the atomic scale, the description happens on the level of classical continuous micromagnetics. The basics are described in many sources, we follow Refs. [82,83].

The main assumption is that the magnet is composed of classical magnetic moments, that can only rotate and not change in size. The length is also assumed to be the same everywhere. It is possible to include length variations, but this is not necessary for the present context. This combines to a description in terms of the continuous magnetisation

$$\boldsymbol{M}(\boldsymbol{r}) = M_0\boldsymbol{n}(\boldsymbol{r}), \tag{84}$$

where $\boldsymbol{n}(\boldsymbol{r})$ is the unit vector pointing into the direction of the magnetisation. The goal is to derive an effective model and use it to calculate the resulting texture. This is done by minimising the Gibbs free energy; hence, we are discussing

different effects and their energy contribution in the following. In general, we both elaborate on spins, which are located on atoms, and the magnetisation, which is continuous and measured by volume. Each spin S has a corresponding magnetic moment

$$\boldsymbol{\mu} = -g\mu_{\mathrm{B}}\boldsymbol{S} \tag{85}$$

where μ_{B} is the Bohr magneton and a constant and $g \approx 2$ the Laundé factor. Moving from discrete spins to a material with a number density of N, the magnetisation is given by

$$\boldsymbol{M}(\boldsymbol{r}) = N\boldsymbol{\mu}(r) = -gN\mu_{\mathrm{B}}\boldsymbol{S}(\boldsymbol{r}) \,. \tag{86}$$

Note that here, the spin is also interpolated. We describe the magnet using a free energy functional $\mathcal{F}(\boldsymbol{n}(\boldsymbol{r}))$ and determine the texture by minimising this energy. In the following, we explore the relevant contributions to our system. In general, there are more possible contributions, for example dipolar or Dzyaloshinskii–Moriya interaction, but those are either accounted by the present terms[81,84] or not necessary to provide 2π domain walls.

2.3.1 Exchange Energy

Despite treating the magnetisation as a classical vector field, we still have to account for some quantum mechanical effects. This is the case for the exchange energy, which stems from the exchange statistics of fermions. Fermionic wave functions are antisymmetric under the exchange of two particles. Thus, it is impossible to have two fermions in the same state, which also includes the position and, of special importance here, spin. This principle is also referred to as *Pauli exclusion*. Therefore, if we take two electrons, their wave functions will look different depending on whether their spin is aligned or not. If their spin is different, there is no resulting effect of *Pauli exclusion*. For electrons of the same spin, though, they avoid being in the same location, leading to the wave function favouring a larger distance between the particles. This has an effect on the Coulomb energy, which is lower due to the effectively larger distance. For two spins, the exchange energy can be written as

$$E_{\mathrm{ex},ij} = -\mathcal{J}_{ij}\boldsymbol{S}_i\boldsymbol{S}_j \,. \tag{87}$$

The prefactor $\mathcal{J}_{ij}$ is called exchange integral and typically decreases exponentially with the distance of sites. and is typically only considered on neighbouring sites. We consider this on a square lattice with lattice constant a and assume that $\mathcal{J}_{ij} = \mathcal{J}$ is the same for all pairs of neighbours. The resulting contribution of the exchange energy density in the continuum is

$$
\begin{aligned}
E_{\text{ex}}(\boldsymbol{r}) = -\frac{\nu\mathcal{J}}{2a^3}\, \boldsymbol{S}(\boldsymbol{r})\Big(&\boldsymbol{S}(\boldsymbol{r} + a\boldsymbol{e}_x) + \boldsymbol{S}(\boldsymbol{r} - a\boldsymbol{e}_x) \\
&+\boldsymbol{S}(\boldsymbol{r} + a\boldsymbol{e}_y) + \boldsymbol{S}(\boldsymbol{r} - a\boldsymbol{e}_y) \\
&+\boldsymbol{S}(\boldsymbol{r} + a\boldsymbol{e}_z) + \boldsymbol{S}(\boldsymbol{r} - a\boldsymbol{e}_z)\Big) + \text{const,}
\end{aligned} \tag{88}
$$

with the number of atoms per unit cell ν and divided by 2 to count every pair only once. We added a constant for now, as a constant shift in energy is not relevant here because it does not affect the resulting texture. As we assumed that the continuum approximation is justified, we can expand with a Taylor series around $\boldsymbol{r}$. For the x-direction, for example, the terms result in

$$
\boldsymbol{S}(\boldsymbol{r})\boldsymbol{S}(\boldsymbol{r} \pm a\boldsymbol{e}_x) = \boldsymbol{S}(\boldsymbol{r})\Big(\boldsymbol{S}(\boldsymbol{r}) \pm a\partial_x\boldsymbol{S}(\boldsymbol{r}) + \frac{1}{2}a^2\partial_x^2\boldsymbol{S}(\boldsymbol{r})\Big) + \mathcal{O}(a^3). \tag{89}
$$

Putting this together with Equation (88) and absorbing the constant terms $\boldsymbol{S}(\boldsymbol{r})^2 = S^2$ results in[17]

$$
E_{\text{ex}}(\boldsymbol{r}) = -\frac{\nu\mathcal{J}}{a}\boldsymbol{S}(\boldsymbol{r})(\Delta\boldsymbol{S}(\boldsymbol{r})). \tag{90}
$$

Note, that the linear derivatives cancel and only the second derivative with the Laplace operator $\Delta = \partial_x^2 + \partial_y^2 + \partial_z^2$ survived. We rewrite this in terms of the magnetisation and obtain

$$
E_{\text{ex}}(\boldsymbol{r}) = -\frac{\nu\mathcal{J}M_0^2}{aN^2g^2\mu_{\text{B}}^2}\boldsymbol{n}(\boldsymbol{r})(\Delta\boldsymbol{n}(\boldsymbol{r})). \tag{91}
$$

We can further simplify this by making use of the fact that the direction of the magnetisation $\boldsymbol{n}(\boldsymbol{r})$ is normalized and thus $\boldsymbol{n}(\boldsymbol{r})^2 = 1$, which gives us the relation

---

[17]Technically, this is only approximately true while neglecting terms of $O(a^3)$, but we just write $=$ here.

$$0 = \sum_j \partial_i^2\big(n_j(\boldsymbol{r})^2\big) = 2\sum_j \partial_i n_j(\boldsymbol{r})(\partial_i n_j(\boldsymbol{r}))$$

$$= 2\sum_j \big((\partial_i n_j(\boldsymbol{r}))^2 + n_j(\boldsymbol{r})\partial_i^2 n_j(\boldsymbol{r})\big) \qquad (92)$$

$$\partial_i\big(\underbrace{\boldsymbol{n}\partial_i\boldsymbol{n}}_{=0}\big) = (\partial_i\boldsymbol{n})^2 + \boldsymbol{n}\,\partial_i^2\boldsymbol{n} = 0 \qquad (93)$$

$$\Rightarrow \boldsymbol{n}(\boldsymbol{r})(\partial_i^2\boldsymbol{n}(\boldsymbol{r})) = -(\partial_i\boldsymbol{n}(\boldsymbol{r}))^2 \qquad (94)$$

with $i, j \in \{x, y, z\}$. Combining this with Equation (91) and introducing the exchange constant, also called stiffness, A, we have

$$E_{\mathrm{ex}}(\boldsymbol{r}) = \underbrace{\frac{\nu\mathcal{J}M_0^2}{aN^2g^2\mu_{\mathrm{B}}^2}}_{A}\big((\boldsymbol{\nabla}n_x(\boldsymbol{r}))^2 + (\boldsymbol{\nabla}n_y(\boldsymbol{r}))^2 + (\boldsymbol{\nabla}n_z(\boldsymbol{r}))^2\big). \qquad (95)$$

This expression energetically favours a spatially constant field distribution. The cause for this is that the derivatives are squared, and thus their contributions are minimal when they vanish. Henceforth, the exchange energy alone would cause a field-polarized (FP) ground state. As we want more complex domain walls, we need other contributions that we will discuss in the following.

2.3.2 Anisotropy

Exchange interaction only considers the relative angle of neighbouring sites. There are other effects, though, which take the orientation relative to the crystal and other effects that depend on orientation into account and are therefore anisotropic. These terms are typically derived by making an expansion and taking the symmetry of the crystal into account. One example is *cubic anisotropy* that, depending on the values of the constants, favours or disfavours the magnetisation being aligned to one of the crystal axes. This can be expressed in first non-vanishing order as

$$E_{\mathrm{cubic}}(\boldsymbol{r}) = K_{\mathrm{cubic}}\big(n_x(\boldsymbol{r})^2 n_y(\boldsymbol{r})^2 + n_x(\boldsymbol{r})^2 n_z(\boldsymbol{r})^2 + n_y(\boldsymbol{r})^2 n_z(\boldsymbol{r})^2\big). \qquad (96)$$

The sign of K_{cubic} determines, whether alignment is energetically beneficial or not. This will not result in the domain walls we desire, so we need to look further. The relevant anisotropy is an *uniaxial* one, which depends on the angle

between the magnetisation and a certain axis. This axis is called $\boldsymbol{e}_{\text{ani}}$ in the following, and in our system will be aligned to the y-axis, as we will later see. In first order, the energy can be written as

$$E_{\text{ani}} = K(\boldsymbol{n}(\boldsymbol{r})\boldsymbol{e}_{\text{ani}})^2 . \tag{97}$$

If K is positive, the magnetisation is pushed into the layer perpendicular to the axis and the term is called *easy-plane anisotropy*. The opposite case of negative K leads to a magnetisation, which is aligned to the axis, having the lower energy, yielding *easy-axis anisotropy*.

2.3.3 Zeeman Energy

So far, all contributions were stemming from internal factors. But, we also have to include an external magnetic field, both because it is necessary to get a tunable domain wall[81] and also because, as discussed in Section 3.3, it is the parameter used to tune the topological properties. For a single dipole moment $\boldsymbol{\mu}$ in a field $\boldsymbol{B}$, the energy is given by

$$E_{\text{Z}} = -\boldsymbol{\mu}\boldsymbol{B} . \tag{98}$$

This is called Zeeman[85] energy. The resulting energy density from this is

$$E_{\text{Z}}(\boldsymbol{r}) = -M_0\boldsymbol{n}(\boldsymbol{r})\boldsymbol{B} . \tag{99}$$

This is minimal, when the magnetisation is aligned to the external field. With that, we have collected all necessary contributions to discuss the domain wall situation.

2.3.4 Magnetic in-Plane Domain Walls

Combining the terms we discussed so far, the free energy density reads

$$\begin{aligned}\mathcal{F}[\boldsymbol{n}(\boldsymbol{r})] = A\Big(\big(\boldsymbol{\nabla}n_x(\boldsymbol{r})\big)^2 + \big(\boldsymbol{\nabla}n_y(\boldsymbol{r})\big)^2\Big) + \big(\boldsymbol{\nabla}n_z(\boldsymbol{r})\big)^2 \\ + K_1 n_z^2 - K_2 n_y^2 - BM_0 n_y . \end{aligned} \tag{100}$$

Here, the easy-plane anisotropy with $K_1 \gg A$ forces the magnetisation to stay in the x-y-plane. Therefore, all z-components and derivatives in z-direction vanish. This is necessary to prevent breaking the superconductivity due to the

high required fields. Taking the limit of K_1 to infinity results in $n_z = 0$, as any finite value would add a lot of energy. Then, we can parametrize the unit vector $\boldsymbol{n}(\boldsymbol{r})$ using polar coordinates

$$\boldsymbol{n}(\boldsymbol{r}) = \begin{pmatrix} -\sin(\theta(\boldsymbol{r})) \\ \cos(\theta(\boldsymbol{r})) \\ 0 \end{pmatrix}. \tag{101}$$

Inserting this into the free energy, we get a new functional in terms of the angle $\theta(\boldsymbol{r})$

$$\mathcal{F}[\theta(\boldsymbol{r})] = 2A\left(\boldsymbol{\nabla}\theta(\boldsymbol{r})\right)^2 - K_2\cos(\theta(\boldsymbol{r}))^2 - BM_0\cos(\theta(\boldsymbol{r})). \tag{102}$$

We choose the direction of the gradient along the x-direction. In reality, this would be fixed by boundary conditions and the shape of the magnet, but we skip over this discussion here. To minimise the energy, we solve the corresponding Euler-Lagrange equation

$$\mathcal{F}[\theta(x)] = A\left(\theta'(x)\right)^2 - K_2\cos(\theta(x))^2 - BM_0\cos(\theta(x)) \tag{103}$$

$$\frac{\mathrm{d}}{\mathrm{d}x}\frac{\partial F}{\partial \theta'} = \frac{\partial F}{\partial \theta}$$

$$2A\theta''(x) = 2K_2\sin(\theta(x))\cos(\theta(x)) + BM_0\sin(\theta(x))$$

$$2A\theta''(x) = K_2\sin(2\theta(x)) + BM_0\sin(\theta(x)). \tag{104}$$

We can simplify this equation by rescaling the constants and the coordinate[35]

$$x = \xi\sqrt{\frac{A}{K_2}} \tag{105}$$

$$\Rightarrow \theta''(x) = \frac{K_2}{A}\theta''(\xi) \tag{106}$$

$$BM_0 = 2K_2 b. \tag{107}$$

This rescaling reduces the Euler-Lagrange equation from Equation (104) to an equation of one effective field b

$$\theta''(\xi) = \frac{1}{2}\sin(2\theta(\xi)) + b\sin(\theta(\xi)), \tag{108}$$

---

[18]The double sine-Gordon equation is named after the similar sine-Gordon equation whose name is a pub on the Klein-Gordon equation.
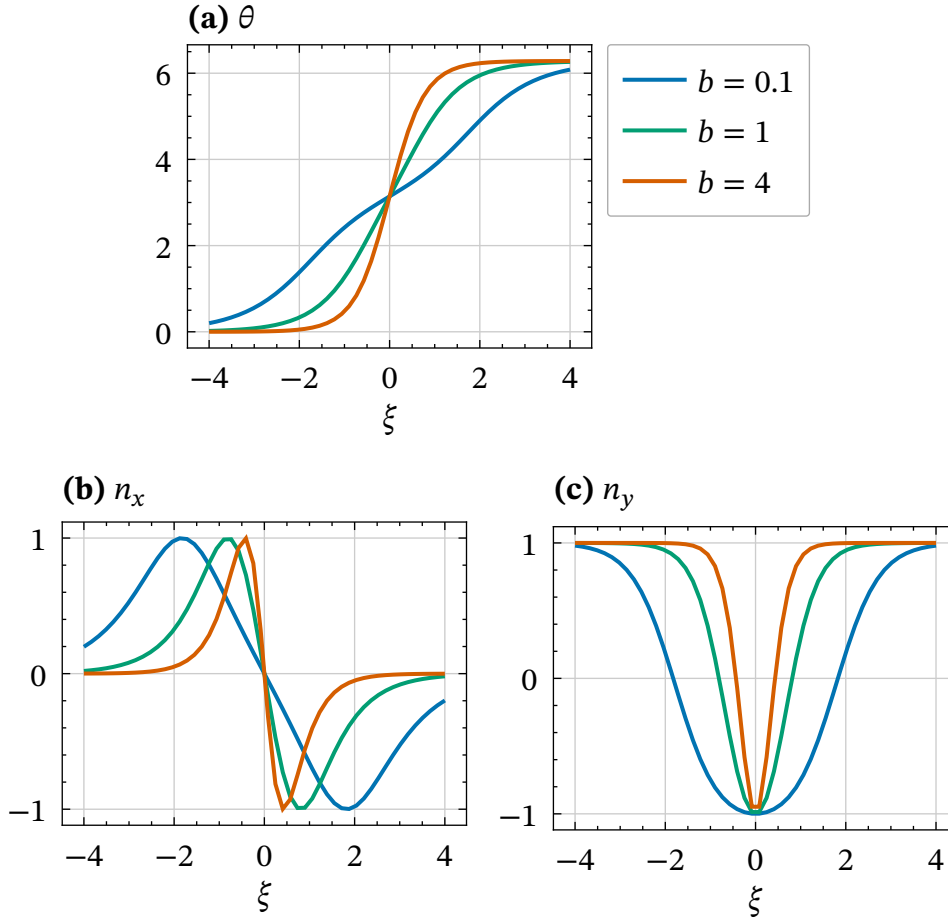
Figure 7: Double kink solution to the double sine-Gordon equation for different parameter values over the rescaled coordinate. Shown are the angle ((**a**)) and the two in-plane components ((**b**) and (**c**)).

which is the well-studied[86,87] double sine-Gordon equation[18]. There are many known solutions to this equation. We are interested in the soliton solution[81]

$$\theta(\xi) = 2\arctan\left(\sqrt{\frac{b}{b+1}}\,\sinh\left(\sqrt{b+1}\,\xi\right)\right) - \pi\,. \tag{109}$$

This profile is shown in Figure 7, where we can see that the parameter b defines the width of the wall in this rescaled coordinate system. For us, the magnetic details are less relevant than the features of the profile. Therefore, we rewrite the profile with different parameters. Additionally, we need to move back to the original coordinate x in order for the profile to be helpful. We choose the form

$$\theta(x) = 2\arctan\left(\frac{\sinh\left(\frac{x}{x_0}\right)}{\sinh\left(\frac{w}{x_0}\right)}\right) - \pi \tag{110}$$

where w describes the width of the domain wall and x_0 the scale on which the rotation happens and therefore the steepness. By comparing this with the previous expression, we can express these geometric parameters in terms of the magnetic parameters. From this we obtain

$$x_0 = \sqrt{\frac{2A}{BM_0 + 2K_2}} \tag{111}$$

$$w = x_0 \operatorname{arcsinh}\left(\frac{b}{b+1}\right)$$

$$= \sqrt{\frac{2A}{BM_0 + 2K_2}} \operatorname{arcsinh}\left(\frac{BM_0}{BM_0 + 2K_2}\right). \tag{112}$$

Thus, by choosing a material with appropriate anisotropy and stiffness it is possible to tune the shape of the magnetisation profile for a given external field. This is necessary because the field is restricted by requiring the superconductor to be topological.

2.4 Dynamical Systems

The second part of this work is concerned with dynamical features. Thus, we discuss here general concepts that are used to evaluate time-dependent behaviours.

2.4.1 Adiabatic Approximation

In the adiabatic approximation, the behaviour of the system is described using the instantaneous eigenstates.[19] Those are defined by the solutions of the instantaneous eigenvalue equation

---

[19]The topic is discussed in many textbooks, we follow the formulation in [88].

$$\hat{\mathcal{H}}(t)|\chi_n;t\rangle = E_n(t)|\chi_n;t\rangle, \tag{113}$$

where the time t is merely treated as a parameter. Note that those are *not* eigenstates of the Hamiltonian. We switched to a braket notation for conciseness as it currently is not necessary to specifically write everything in real space. But the approximation made in the adiabatic limit is that the system is well described by them. They do, however, form a complete orthogonal base. Thus, we expand the initial state of the system in this basis and write

$$\begin{aligned}
\psi(\mathbf{r},t) &= \sum_n c_n(t)\chi_n(\mathbf{r},t) \\
&= \sum_n c_n(t)\langle \mathbf{r}|\chi_n;t\rangle.
\end{aligned} \tag{114}$$

The time evolution of these is still described by the full time-dependent Schrödinger equation. The instantaneous states can be obtained by solving Equation (113). Consequently, instead of examining the full states, we shift our focus to the time-dependent coefficients $c_n(t)$. We start by taking the time derivative of Equation (113) and considering that the time dependence of $\psi(\mathbf{r},t)$ is given by the time-dependent Schrödinger equation. This yields

$$\begin{aligned}
&\sum_m c_m(t)E_m(t)|\chi_m;t\rangle \\
&= \mathrm{i}\partial_t \sum_m c_m(t)|\chi;t\rangle \\
&= \mathrm{i}\sum_m (\dot{c}_m(t)|\chi;t\rangle + c_m(t)|\dot{\chi}_m;t\rangle).
\end{aligned} \tag{115}$$

We make use of the orthogonality of the instantaneous states by taking the scalar product from the left with $\langle \chi_n;t|$. With that, we can isolate $\dot{c}_n(t)$ and therefore obtain the different equations which govern the time evolution of the coefficients. This reads

$$\dot{c}_n(t) = -\mathrm{i}E_n(t)c_n(t)E_n - \sum_m \langle \chi_n;t|\dot{\chi}_m;t\rangle c_m(t). \tag{116}$$

So far, no approximation has been made, and the equation is exact. But now we need to evaluate the matrix elements $\langle \chi_n;t|\dot{\chi}_m;t\rangle$ in more detail. To achieve this, we take the time derivative of Equation (113). Why this is useful is difficult to see, but will become more clear after taking yet again the scalar product with $\langle \chi_n;t|$ and a rearrangement of the terms. We get

$$\langle\chi_n;t|\dot{\hat{\mathcal{H}}}(t)|\chi_m;t\rangle + \langle\chi_n;t|\hat{\mathcal{H}}(t)|\dot{\chi}_m;t\rangle$$
$$= \langle\chi_n;t|\dot{\hat{\mathcal{H}}}(t)|\chi_m;t\rangle + E_n(t)\langle\chi_n;t|\dot{\chi}_m;t\rangle$$
$$= \dot{E}_m(t)\langle\chi_n;t|\chi_m;t\rangle + E_m(t)\langle\chi_n;t|\dot{\chi}_m;t\rangle$$
$$= \dot{E}_n(t)\delta_{n,m} + E_m(t)\langle\chi_n;t|\dot{\chi}_m;t\rangle . \tag{117}$$

For the case where $n \neq m$, we can simplify this further and get

$$\langle\chi_n;t|\dot{\chi}_m;t\rangle = -\frac{\langle\chi_n;t|\dot{\hat{\mathcal{H}}}(t)|\chi_m;t\rangle}{E_n(t) - E_m(t)} \quad (n \neq m). \tag{118}$$

We insert this matrix element into the differential equation for the coefficient $c_n(t)$ (Equation (116)). Some care has to be taken to not ignore the term in the sum with $n = m$. In total the differential equation turns into

$$\dot{c}_n(t) = \mathrm{i}(-E_n(t) + \mathrm{i}\langle\chi_n;t|\dot{\chi}_n;t\rangle)c_n(t)$$
$$+ \sum_{m\neq n} \frac{\langle\chi_n;t|\dot{\hat{\mathcal{H}}}(t)|\chi_m;t\rangle}{E_n(t) - E_m(t)} c_m(t). \tag{119}$$

So far, we have not gained any simplification, but now the approximation of an adiabatic process comes into play. For a slowly changing and gapped Hamiltonian, we neglect the sum. This decouples the differential equations and leads to an oscillating solution for the coefficients. The two remaining terms provide two different phases. The solution for the coefficients read

$$c_n(t) = c_n(0)\mathrm{e}^{\mathrm{i}\theta_n(t)}\mathrm{e}^{\mathrm{i}\gamma_n(t)} \tag{120}$$

$$\theta_n(t) \equiv -\int_0^t \mathrm{d}t'\, E_n(t') \tag{121}$$

$$\gamma_n(t) \equiv \mathrm{i}\int_0^t \mathrm{d}t'\, \langle\chi_n;t|\dot{\chi}_n;t\rangle \tag{122}$$

with the dynamical phase $\theta_n(t)$ and the geometric phase $\gamma_n(t)$.

2.5 Numerical Methods

In addition to physical concepts, numerical considerations are also important as many calculations in this work have been carried out with the help of software.

2.5.1 Large Eigenvalue Problems

Most of the numerical calculations in this work are solving large eigenvalue problems. Additionally, only a few eigenvalues and corresponding eigenvectors around zero are needed, as this is where the MBSes appear and also where the relevant topology happens.

Due to the large, but luckily very sparse, matrices a straightforward dense matrix diagonalization is not feasible. The typical matrix in this work has, as a rough estimate, around $320\,000^2 = 102\,400\,000\,000$ complex entries, which corresponds to a size of around $800\,\text{TB}$ with single precision floats. This is not feasible to hold in memory, especially considering that this is only the space required for the matrix itself and does not include the space for the calculation and the output. Consequently, a sparse matrix format is needed. Sparse matrices do not consist of a list of all entries like dense matrices, but instead hold information where non-zero entries are to be found. There are different approaches to this, that have different advantages and drawbacks, but for the discussion here, the storage format of the matrices is not relevant. Instead, we focus on the eigenvalue solver as here, the specifics of our problem play a role and have to be considered (see Section 3.5.3 for a discussion). Those will not solve the problem exactly, but find a good approximation of the solution.

Krylov Subspace

The main idea behind the most used algorithms for large sparse eigenvalue problems is the concept of the so called *Krylov subspace*[89]. It is built on a simple observation. We take a matrix $\bar{M} \in \mathbb{C}^{N \times N}$ which has, to us unknown, eigenvector $\boldsymbol{v}_i$ with corresponding eigenvalues λ_i and some vector $\boldsymbol{\varphi} = \sum_{i=1}^{N} a_i \boldsymbol{v}_i$ that is a linear combination of some eigenvectors. If we then repeatably multiple $\boldsymbol{\varphi}$ with the matrix $\bar{M}$, the contribution of the eigenvector with the largest eigenvalue that has a non-zero coefficient a_i will grow with each iteration:

$$\varphi = \sum_{i=1}^{N} a_i \boldsymbol{v}_i \tag{123}$$

$$\bar{M}\varphi = \sum_{i=1}^{N} a_i \lambda_i \boldsymbol{v}_i \tag{124}$$

$$\vdots \tag{125}$$

$$\bar{M}^n \varphi = \sum_{i=1}^{N} a_i \lambda_i^n \boldsymbol{v}_i \tag{126}$$

To avoid the growing length of the vector, we normalize it at each step and obtain the procedure

$$\boldsymbol{b}_0 = \varphi \tag{127}$$

$$\boldsymbol{b}_{i+1} = \frac{\bar{M}\boldsymbol{b}_i}{|\bar{M}\boldsymbol{b}_i|} . \tag{128}$$

Thus, this schema converges to an eigenvector of the matrix, and we already have a very limited, but simple way to find an eigenvector of a matrix. This simple method, called *power iteration* or *von Mises method*[90], already shows a crucial, but not that obvious, advantage. Note, that nowhere we specifically use the matrix itself, but only needed to know what happens when we multiply a vector with the matrix. This might seem irrelevant, but circumvents the issue of having to hold the full matrix in memory and is also suitable for usage with sparse matrices.

More advanced methods extend this, by building a k-dimensional subspace spanned by the vectors $\{\varphi, \bar{M}\varphi, ..., \bar{M}^{k-1}\varphi\}$. This subspace is called the *order-k Krylov subspace* of the matrix $\bar{M}$. By solving in this smaller subspace, the calculation is less intense. k is typically an input parameter to the methods and can be used as a tuning parameter. The higher k is, the more memory and time the calculation will take, but the more eigenvalues can be calculated (as the subspace is bigger) and the more accurate the approximation is. To be more precise, the used libraries are calling ARPACK[91], which implements a variation of the *Arnoldi* method[92] called *implicitly restarted Arnoldi*[93,94], which improves the results without needing a huge subspace. We only discussed eigenvalues, as calculating eigenvectors is a separate step afterward anyway.

Solving for Small Eigenvalues

As we have seen, the methods discussed so far are working well for finding eigenvalues with large absolute value[20]. This is the opposite of what we require in this work as the MBSes have zero energy and their approximations in the numerics energies are very close to zero. We very much simplified the discussion before and ARPACK actually supports different criteria to select eigenvalues, among which is also one for *smallest absolute value*.[21] So, technically, we are done here and can just use this setting.

There is a trick, though, that comes with some additional computation, but resolves this issue. If we have an invertible matrix $\bar{M}$ that has eigenvalues λ_i, its inverse $\bar{M}^{-1}$ has eigenvalues λ_i^{-1}. The matrix being invertible might sound like a contradiction to our problem, MBSes are at zero energy after all. But here, the system being finite is beneficial as, which we will discuss later, this leads to the energy not being exactly zero, just very close. This means that eigenvalues of $\bar{M}$ close to zero map to eigenvalues with a large absolute value of $\bar{M}^{-1}$. Therefore, we can apply the previously discussed methods on $\bar{M}^{-1}$ to obtain eigenvalues and then just invert them.

But, we cannot just invert the matrix, as the inverse of a sparse matrix is not necessarily sparse as well. Thus, a simple inversion could blow up the memory usage and make the method impractical again. Recalling an earlier statement, we do not actually need to know the matrix we want to diagonalize, only knowing, what happens when multiplying it with a vector is sufficient. Multiplying a vector with the inverse of a matrix

$$\boldsymbol{b} = \bar{M}^{-1}\boldsymbol{a} \tag{129}$$

is equivalent to solving the linear equation system

$$\bar{M}\boldsymbol{b} = \boldsymbol{a} \tag{130}$$

for the vector $\boldsymbol{b}$, which again is possible to approximately do for sparse systems. While not relevant for our current work, it is interesting to note that this scheme

---

[20]The following discussion assumes that the matrix is hermitian and hence all eigenvalues are real. The idea also works for the more general case of complex eigenvalues, but this is not of relevance here.

[21]How this actually works requires digging too deep into the numerical methods, so for more explanation about this, refer to the numerical papers[91,93,94].

also works for values close to some other value ν and not just zero by shifting the matrix by subtracting $\nu\mathbb{1}$ in addition to inverting it. This is also why settings related to this are typically referred to *shift invert* in numerical libraries.

Magnet Superconductor Hybrids 3

Superconductor magnet hybrids are thin layer systems consisting of a superconducting and a magnetic layer. They have been proposed for a wide range of different platforms, in the context of Majoranas [20,30–32,95–99], but also for more general investigations about the interplay of magnets and superconductors [100–102]. As, in this work, we are interested in Majoranas, we will only focus on those. There are proposals in a few different directions, utilizing different mechanisms.

One class of proposals focuses on coupling skyrmions in the magnetic layers with vortices in the superconductor[31,99,103]. In this setup, it is possible to get a pair of Majoranas, where one is located in the centre of the skyrmion-vortex pair and the other one on the edge of the system. A very similar one deals with skyrmions with even winding numbers[31]. There, the location of the Majoranas is the same as with Skrymion-vortex pairs.

Another, for us, more relevant, class deals with using a spatially varying magnetic field to restrict the topological region. For a more detailed description of this concept, see Section 3.3.7. If restricted in a suitable way, it is possible to obtain an effectively one-dimensional region that can host zero-dimensional MBSes. The proposals go in different directions here, depending on the source of topology.

One approach utilizes pairs of circular skyrmions[31,99,103,104] or alternatively skyrmions with even winding numbers[31,105]. This can lead to a localised MBS in the centre of the pair. As MBSes have to always appear in pairs, there is another one present in the system, but located at the edge and therefore for an infinite system at infinity. Thus, it differs from the approach discussed here where we get zero-dimensional MBSes at the edge of an (effectively) one-dimensional region. skyrmions can also be utilized differently by using elongated skyrmions[30]. Another approach is to use a chain of magnetic adatoms[26,96,97,106–111]. This is a simple and experimentally accessible, but lacks features for controlling the Majoranas.

To combine the benefits of the various approaches, we propose the usage of a multi-layer system like in the case of skyrmions, where the magnetic layer hosts a 2π domain wall. Such a system is easier to realise in experiments than a skyrmion based one, while making dynamical features accessible. This is facilitated by the
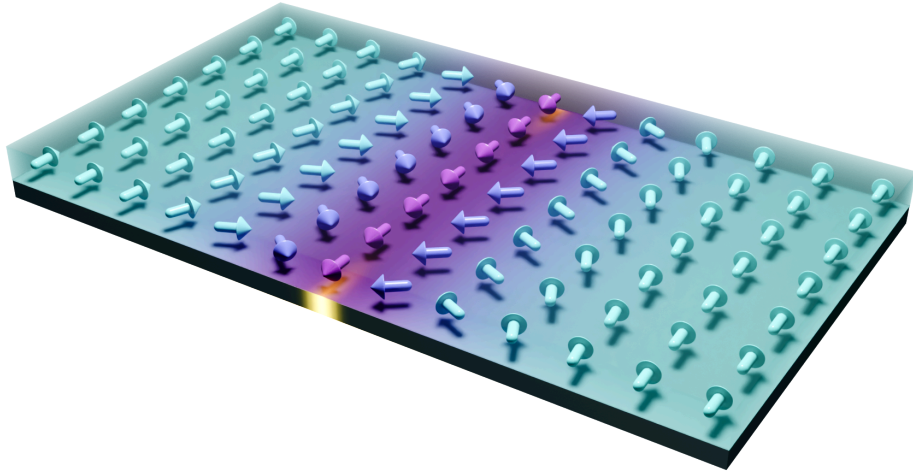
Figure 8: Visualization of the setup. A magnetic layer containing a 2π domain wall is coupled to a superconducting layer. Not shown is an additional uniform background field. All fields are in the plane. In the superconducting layer, Majorana bound states are found and denoted by glowing.

fact that the domain walls can be moved[40]. Access to dynamics is essential for many use cases, especially topological quantum computers. For computations, dynamical venues are needed to achieve a braiding of Majoranas[112]. Part of this chapter was published under Ref. [44].

3.1 Why 2π Domain Walls?

While discussed before, we shortly motivate again the usage of magnetic domain walls. For MSHes, there are several proposed setups which can host MBSes and were mentioned before in the introduction of this part. The two for this work most relevant ones use elongated skyrmions[33] or magnetic adatoms[26,96,97,106–111]. These are very similar in the sense that they use the same topological mechanism, but they differ widely regarding experimental concerns and also their dynamical possibilities. Magnetic adatom chains are approachable in experiments, but are static and cannot easily be moved. Elongated skyrmions, on the other hand, are difficult to obtain experimentally and are also suffering from the fact that fields are mostly out-of-plane. Due to the high

strength of required fields, this would break the superconductivity. However, skyrmions are movable with spin-currents, hence offering more dynamic possibilities. Magnetic 2π domain walls are easier to realise experimentally than elongated skyrmion and retain the dynamical access. Additionally, in-plane field configurations are possible, circumventing the out-of-plane issues.

3.2 Model

The system is described on the level of a BdG Hamiltonian, with the magnetic layer providing a magnetic field via a Zeeman coupling. See Section 2.1.2 for an introduction to the formalism. The Hamiltonian is given by

$$\hat{H} = \left(-\frac{\hat{\mathbf{\nabla}}^2}{2m} - \mu\right)\bar{\tau}_z + \Delta\bar{\tau}_x - J\mathbf{M}(x) \cdot \bar{\mathbf{\sigma}} + B\bar{\sigma}_y + i\alpha(\hat{\mathbf{\nabla}} \times \bar{\mathbf{\sigma}})\bar{\tau}_z \quad (131)$$
$$\bar{\sigma}_i = \bar{\bar{\mathbb{1}}}_2 \otimes \bar{\Sigma}_i$$
$$\bar{\tau}_i = \bar{\Sigma}_i \otimes \bar{\bar{\mathbb{1}}}_2 \,.$$

Here, $\bar{\tau}_i$ and $\bar{\sigma}_i$ are 4×4 Pauli matrices in particle-hole and spin space and $\bar{\Sigma}_i$ the usual 2×2 Pauli matrices[22]. There are many parameters here, so let us go through each of them. Δ describes the superconducting gap and gives an upper bound on how large the topological gap can be. It also introduces an energy scale, allowing us to later discuss all energies relative to Δ. For a more in-depth discussion of units and the scales in the model, refer to Chapter A. The mass m and chemical potential μ describe the dispersion without the superconductivity. There are two sources of magnetic fields. The magnetisation texture $\mathbf{M}(x)$ provides a spatially varying field, relayed through the interlayer coupling J. Note, that it depends solely on the x coordinate. This, as we will see in the next section, provides an effectively one-dimensional channel that allows for MBSes as zero-dimensional edge states. Additionally, an external uniform field B puts the channel into the topological regime, while the background stays trivial (see next section). All fields are in-plane, with the z-axis pointing out of the plane. Finally, SOC, given here in the form of a Rashba coupling with strength α, is required for the topology.

The interlayer coupling J is positive, resulting in an antiferromagnetic coupling of the layers. This is necessary to stabilize the magnetic texture at the same time as having topology in the superconductor, meaning the inside of the

---

[22]Here denoted in a non-standard notation due to the already existing common use of $\bar{\sigma}$.
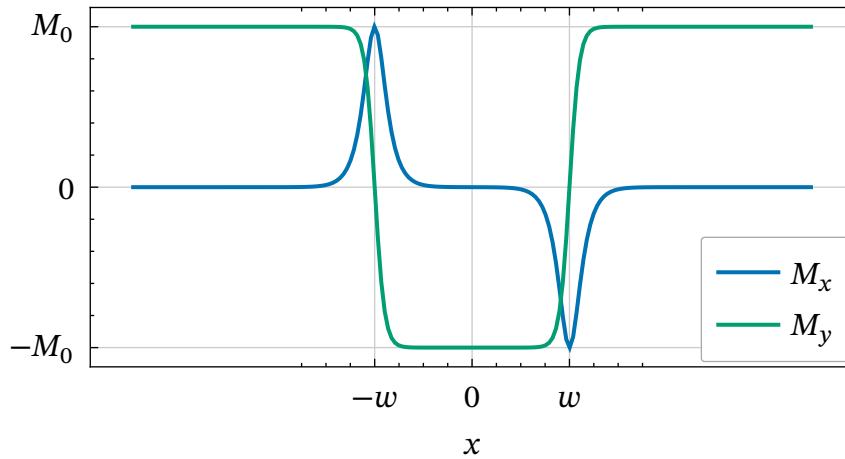
Figure 9: Components of the magnetisation profile with a width w, steepness $x_0 = 0.1w$, and amplitude M_0.

domain wall has to align with the external field, while for the magnetic layer, the energy of the field polarised background has to be minimised.

3.2.1 Magnetic Texture

The magnetic texture, as mentioned before, is given in the form of a 2π domain wall. The form is given by[35,81]

$$\boldsymbol{M}(x) = M_0 \begin{pmatrix} \sin(\theta(x)) \\ \cos(\theta(x)) \\ 0 \end{pmatrix} \tag{132}$$

$$\theta(x) = 2\arctan\left(\frac{\sinh\left(\frac{x}{x_0}\right)}{\sinh\left(\frac{w}{x_0}\right)}\right) - \pi . \tag{133}$$

See Figure 9 for a sketch of the shape. Three new parameters have been introduced here. The first one is the amplitude of the magnetisation M_0. The two lengths determine the shape of the domain wall. w is the width and signifies the distance from the centre, at which the magnetisation completely points into the x-direction. x_0, on the other hand, describes how quick the rotation happens. The smaller the value of x_0, the closer the shape is to a box. Refer to Section 2.3 for a discussion of how these geometrical parameters arise from the magnetic material parameters.

3.3 Topology of the System

Explaining the topology of the full system is a quite complicated endeavor. Thus, we first start with a conceptual discussion of general topological systems. From this point, we show a path to obtain zero-dimensional states, which the MBSes are, in a two-dimensional system.

Afterwards, the application of these concepts to our more concrete situation. For this, we start from the case of one-dimensional edge states with out-of-plane fields. Then we extend this to the — as discussed before, necessary — in-plane situation. Finally, we introduce magnetic texture as our chosen tool to get zero-dimensional edge states. Because the system is a topological superconductor, these states have Majorana character (see Section 2.2.6).

3.3.1 Topological Scheme

Let us assume that we are given a two-dimensional physical system, which has some tuning parameter λ that allows us to tune it between a topological and a trivial phase. The topological phase is existent above a critical value λ_c, the trivial one below it. Those phases can be classified using a topological invariant (see Section 2.2). This invariant is a property of the *bulk* system, meaning an infinite system described by a Hamiltonian $\hat{H}(\boldsymbol{k}; \lambda)$. Bulk-edge correspondence (see Section 2.2.5) now tells us that we can expect a bound state on an interface between topologically different regions. This state has a certain localisation length associated with it, which can depend on various parameters. Typically, it is mostly governed by the topological gap.

The easiest way to achieve this is to use a sample of finite size. Then we have an interface between the system, whose topology depends on the choice of λ, and the trivial vacuum around. Thus, by tuning λ, we can create and destroy an edge state on this interface. In Figure 10, this is schematically drawn. For a choice of $\lambda < \lambda_c$ (Figure 10 (a)), the edge of the system is an interface between two trivial and therefore topologically equivalent regions, and hence no edge state exists. In the regime of $\lambda > \lambda_c$ (Figure 10 (b)), the sample is topological though and consequently not equivalent to the surrounding vacuum. This leads to an in-gap state, that is localised around the edge. As the edge of a two-dimensional system is one-dimensional, this state is also one-dimensional. While these states can
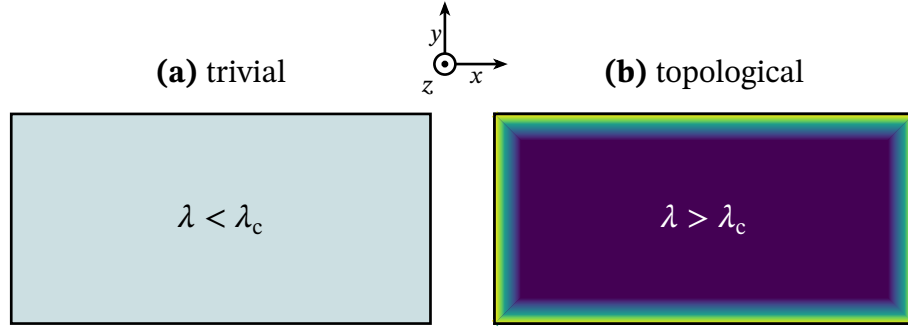
Figure 10: Two-dimensional topological rectangular sample in **(a)** the trivial and **(b)** the topological regime. For the topological case, the arising edge state is schematically shown.

pose interesting subjects for study, in the present work the focus is on MBSes. And those states are not one-, but zero-dimensional. Thus, we need some way to reduce the dimensionality of the problem.

3.3.2 Effective One-Dimensional Region

While there are other methods of obtaining this goal, we will achieve this by restricting the topology to a small region, that is effectively one-dimensional[23]. For this, we now let the parameter λ not be a constant any more, but have it vary in space. This can, in general, influence the topology which is dictated by the dependence of the Hamiltonian on spatial derivatives of λ. We assume for now that this effect is small and that the general topological properties are not changed by this. Using this assumption, the topological classification can be performed locally, meaning that we can individually label each location with the topological phase information.

Our aim is still to reduce the dimensionality to an effectively one-dimensional system. Thus, we choose a arbitrary direction for now and vary λ in such a way that it only exceeds the critical value of λ_c. This is visualized in Figure 11. If the width of this region becomes small compared to the localisation length the sides hybridize, and we are left with zero-dimensional edge states, hence achieving our goal.

---

[23]We will return later to the question, what this actually means. The impatient reader can jump to Section 3.3.7 for this.
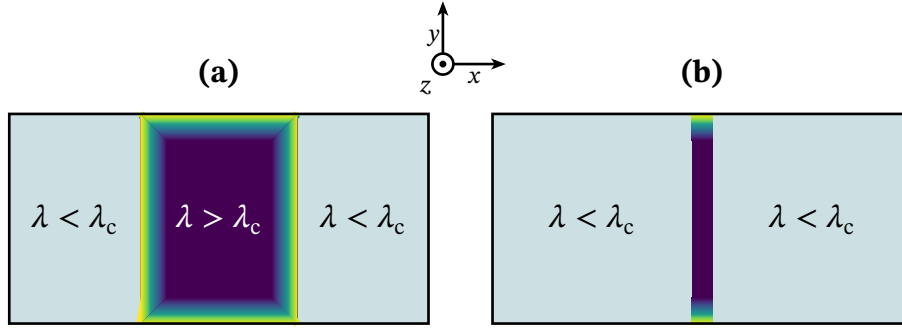
Figure 11: Restriction of the topological region from a smaller rectangle **(a)** up to an effectively one-dimensional region **(b)**.

In the following sections, we show how this rather abstract concept can be applied to our concrete system. We will also see how this discussion over-simplifies the picture for the case of in-plane fields. As a start, though, we introduce the situation arising from out-of-plane fields.

3.3.3 Constant Fields in a Superconducting Wire

We come back to a more specific example and examine a Hamiltonian that is very similar to the one from our model (Equation (131)), but for now in one-dimension, here oriented along the y-axis. We ignore the magnetic texture for now and just apply a field in z-direction, which is different from the in-plane field in our system, which we will discuss in the following section. The Hamiltonian is given in $\boldsymbol{k}$-space by

$$\bar{H}_{1\mathrm{d},z} = \left(\frac{k_y^2}{2m} - \mu\right)\bar{\tau}_z + \Delta\bar{\tau}_x + B\bar{\sigma}_z - \alpha k_y\bar{\sigma}_x\bar{\tau}_z\,. \tag{134}$$

This system is well studied and found to exhibit a critical field of $B_\mathrm{c} = \sqrt{\Delta^2 + \mu^2}$. If the absolute value of the field exceeds this value, the system is in a topological phase[17,113,114]. For simplicity, we assume that $B \geq 0$ as the direction is irrelevant. Therefore, the field B plays the role of our parameter λ from before.

The Hamiltonian from Equation (134) has four bands as it acts on a four-component Nambu spinor. As we already mentioned before, B is our topological tuning parameter. It is not immediately obvious, why we would need the additional SOC, described with the Rashba coupling α. We know from Section 2.2 that a topological transition can only occur when the gap closes and opens again.
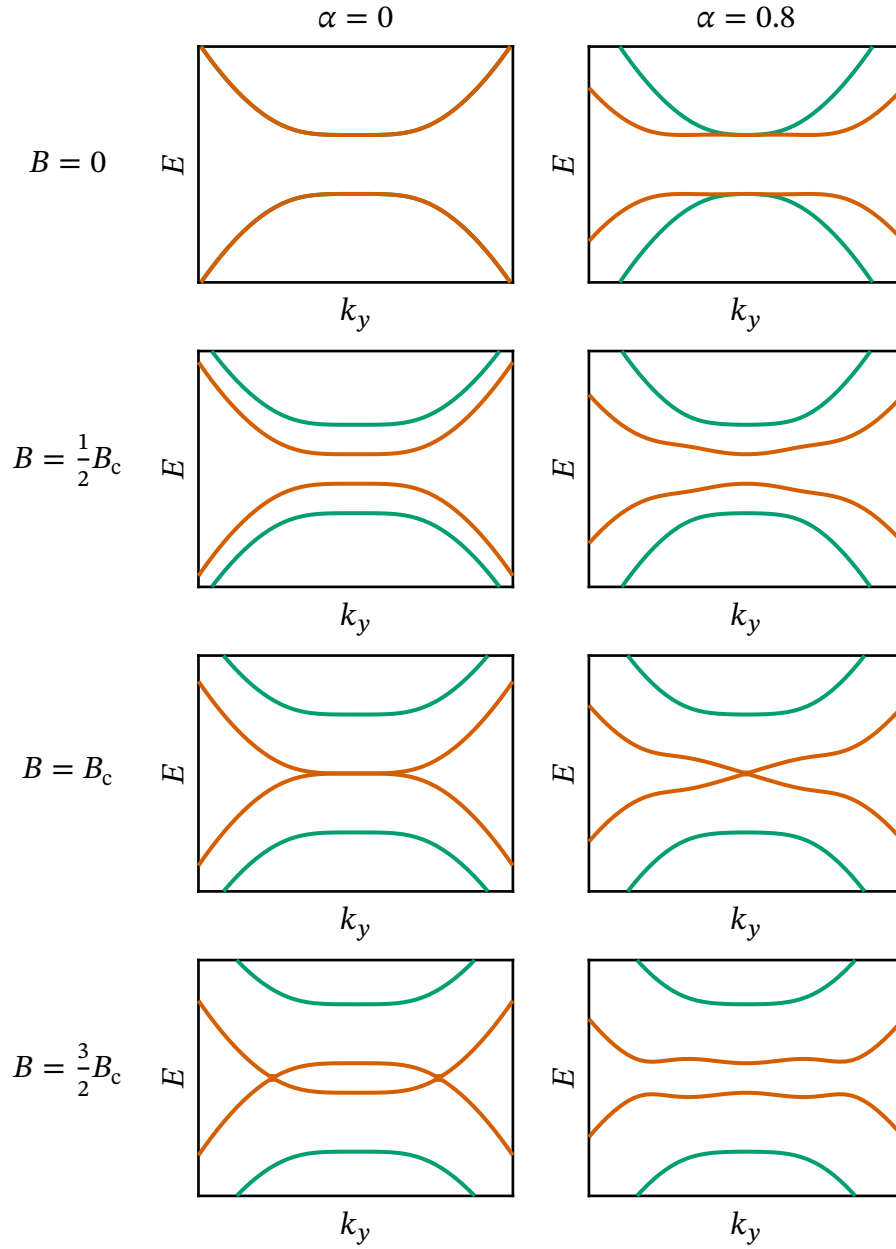
Figure 12: Spectrum of a one-dimensional s-wave superconductor along the y-axis in a constant Zeeman field in z-direction, described by Equation (134) with $\Delta = 0$, $m = 1$ and $\mu = 0$. From top to bottom the field is increased and the spectra with (right column) and without (left column) SOC are compared. This shows that without SOC, the gap does not open up again, hence no topology can be observed. The lower pair of bands that is responsible for the topology is marked in orange, the outer ones in green.

Thus, we have a look at the spectrum of $\bar{H}_{1d,z}$ and examine a sweep over the parameter B. In Figure 12, the resulting spectra for a certain set of parameters is presented both with and without SOC. It is directly visible that, at least for the chosen set of parameters, the system without SOC cannot exhibit topological behaviour as the gap never reopens after being closed.

But is this statement also true in general? For arbitrary values of the parameters, the eigenvalues of $\bar{H}_{1d,z}$ are given by

$$E_{\pm\pm} = \pm\sqrt{B^2 + k_y^2\alpha^2 + \Delta^2 + \varepsilon_{k_y}^2 \pm 2\sqrt{B^2\left(\Delta^2 + \varepsilon_{k_y}^2\right) + k_y^2\alpha^2\varepsilon_{k_y}^2}} \quad (135)$$

$$\varepsilon_{k_y} = \frac{k_y^2}{2m} - \mu. \quad (136)$$

We now set $\alpha = 0$ and look at the squared energy. This is enough, as the spectrum is symmetric around 0, and we are only interested in whether there is a gap around 0 or not. This leaves us with

$$E_{\pm\pm}^2\Big|_{\alpha=0} = B^2 + \Delta^2 + \varepsilon_{k_y}^2 \pm 2\,|B|\,\sqrt{\Delta^2 + \varepsilon_{k_y}^2}$$

$$= \Bigg(\underbrace{B \pm \sqrt{\Delta^2 + \varepsilon_{k_y}^2}}_{A_\pm}\Bigg)^2. \quad (137)$$

As $\varepsilon_{k_y} \in [-\mu, \infty)$, the second term is limited by $\sqrt{\Delta^2 + \varepsilon_{k_y}^2} \in [B_c, \infty)$. The lower bound is just the previously mentioned critical field of $B_c \equiv \sqrt{\Delta^2 + \mu^2}$. We restricted ourselves to positive B, A_+ is always further away from 0 than A_-. Thus, it is sufficient to only investigate A_- when discussing the existence or non-existence of a gap. In fact, the range that A_- spans for the set of possible k-values contains 0 if and only if there is a gap. From the above discussed bounds on terms, it follows that A_- is unbounded from above, hence 0 is exactly then in the range when the minimum is $\min_k A_- \leq 0$. With the ranges discussed before, this minimum is given by $\min_k A_- = B - B_c$, which is ≤ 0 exactly when $B \leq B_c$. This means that the feature that we observe for $\alpha = 0$ in Figure 12 for a single set of parameters is indeed general, and the gap closes at $B = B_c$ and does not open again.

As we already saw in the example in Figure 12, for $\alpha \neq 0$ it is possible for the gap to reopen again. This alone does not prove that there is topology to be found here, which is a problem that we will tackle later in this section. But first,

we discuss the question of generality here as well. There are multiple questions arising here:

1. Is the gap always closed at $B = B_c$?
2. Is the gap always reopening?

For the specific set shown in Figure 12, the answer to both of those is yes. Just like before, we use the fact that due to the existing PHS, it is sufficient to look at the squared energy, which reads

$$
\begin{aligned}
E_{\pm\pm}^2 &= B^2 + k_y^2\alpha^2 + \Delta^2 + \varepsilon_{k_y}^2 \pm 2\sqrt{B^2\left(\Delta^2 + \varepsilon_{k_y}^2\right) + k_y^2\alpha^2\varepsilon_{k_y}^2} \\
&= \left(B \pm \sqrt{\Delta^2 + \varepsilon_{k_y}^2\left(1 + \frac{k_y^2\alpha^2}{B^2}\right)}\right)^2 + k_y^2\alpha^2\left(1 - \frac{\varepsilon_{k_y}^2}{B^2}\right).
\end{aligned}
\tag{138}
$$

We can now examine what happens at the points, where the gap is closed for $\alpha = 0$ if we turn on SOC. Those points are given by the roots of Equation (137) in terms of k_y, which are determined by $\varepsilon_{k_y,0\pm} = \pm\sqrt{B^2 + \Delta^2}$. Solving this for k_y yields

$$
k_{0\pm} = \sqrt{2m\left(\mu \pm \sqrt{B^2 - \Delta^2}\right)}
\tag{139}
$$

as a positive solution and $-k_{0\pm}$ as another one. These do not exist for all possible parameter values, so we will have to determine some conditions. But it already allows us to answer the first question from above. At $B = B_c$ there is always a band that crosses 0 at $k_y = 0$. This means that not only the gap is indeed closed at $B = B_c$, it is always closed at $k_y = 0$, which we also observe in the example in Figure 12. From Equation (139), a first straightforward condition can be extracted: the field has to be larger than the superconducting gap[24]. Above this limit, k_{0+} is always real, k_{0-} on the other hand, only until B exceeds B_c. Knowing this, we insert these solutions into Equation (137) and expand around $\alpha = 0$ to examine what happens when we turn on SOC. As ε_{k_y} only enters quadratically, we obtain

---

[24]Remember that we chose B to be positive, which is allowed for symmetry reasons without loss of generality.

$$E_{0-\pm,\pm} = \pm k_{0\pm} \frac{\Delta}{B} \alpha + \mathcal{O}(\alpha^2) \tag{140}$$

$$E_{0+\pm,\pm} = \pm 2B + \mathcal{O}(\alpha^2). \tag{141}$$

We can immediately discard the outer bands $E_{0+\pm,\pm}$ as they will never cross 0. The inner bands $E_{0-\pm,\pm}$ can, for finite SOC α, only close the gap if $k_{0,\pm} = 0$. Thus, our questions are answered for small values of α: The gap only closes exactly at $B = B_c$ and is open otherwise, answering both our questions with "yes". Additionally, the opened gap, which is the topological gap if the state is topological, is proportional to α.

While the specific results do not extend to arbitrary values of α, the existence and closing points of the gap hold true for arbitrary values. We can see this, by examining the roots of Equation (138) for general α. For this, we obtain the conditions

$$\varepsilon_{k_y} = \pm \sqrt{B^2 + \left(k_y \alpha \pm i\Delta\right)^2}. \tag{142}$$

As ε_{k_y} is real and so are all the parameters in the equation, this can only be solved if $k_y \alpha = 0$. This is trivially solved for $\alpha = 0$, but for finite α, this can only be satisfied at $k_y = 0$ or in the limit of $k_y \to \pm\infty$. In the infinite limit, the left-hand side of the equation is of $\mathcal{O}(k_y^2)$ while the right-hand side scales with $\mathcal{O}(k_y)$, ruling out that option. Thus, also for arbitrary finite values of α the gap only closes at $k_y = 0$ and $B = B_c$.

Now that we know that there is a gap closing at this point and got some intuition about it, we move forward to the analysis of the topology itself. To understand more about this, we need to look at the symmetries of the system. Refer to Section 2.2.4 to read about the general idea and also Refs. [79,114]. The first step is to look for remaining unitary symmetries that would allow us to write the Hamiltonian in a strictly block-diagonal form. This is also the point where it plays a role whether the SOC parameter α is finite or not.

Vanishing Spin-Orbit Coupling

From our spectrum analysis before, we already know that without SOC, there is no gap and therefore also no topology. But, as a preparation for the following

discussion, it is educational to approach this from the point of the underlying symmetry classification.

If there is no SOC, spin- and particle-hole-space are completely uncoupled. Thus, we have this additional symmetry and can write the Hamiltonian as two blocks — one for each spin direction along the field direction. Each of the blocks has the form

$$\bar{H}_{1d,z,0,\pm} = \left(\frac{k_y^2}{2m} - \mu\right)\bar{\Sigma}_z + \Delta\bar{\Sigma}_x \pm B\,\bar{\mathbb{1}}_2 \tag{143}$$

where $\bar{\Sigma}_i$ are again the usual 2×2 Pauli matrices. The first property of note is that the Hamiltonian is completely real. Hence, complex conjugation $\hat{\mathcal{K}}$ is an antiunitary operator commuting with the Hamiltonian, thus acting as a form of TRS with sign $\hat{\mathcal{K}}^2 = +1$. But as we are not looking at the full Hamiltonian any more, we have to also check PHS. Here, the field B prevents the PHS from existing. This can be intuitively understood through the spectrum. PHS causes the spectrum to be symmetric around zero, as the states can always be grouped into pairs with energies of opposite sign. The field term is proportional to the identity matrix, though, and thus causes the full spectrum to be shifted up or down by B. This leads to the spectrum no longer being symmetric. Alternatively, we can also directly see the effect of a PHS operator on this term. Any PHS operator $\hat{\mathcal{C}}$ can be written as complex conjugation $\hat{\mathcal{K}}$ combined with a unitary matrix $\bar{U}_C$. This operator commutes with the term $B\,\bar{\mathbb{1}}_2$ as the identity matrix commutes with any operator, and the complex conjugation does nothing either due to everything being real.

Summarizing the relevant symmetries, we only have TRS with a positive sign. This puts us in class AI, which is indeed always trivial both in one and two dimensions according to the periodic table of topological matter (see Table 2).

Finite Spin-Orbit Coupling

SOC couples the different spin directions with each others, thus breaking the symmetry that makes the Hamiltonian block diagonal in spin-space. Hence, the proper level to analyse the topology is the full 4×4 Hamiltonian

$$\bar{H}_{1\text{d},z} = \left(\frac{k_y^2}{2m} - \mu\right)\bar{\tau}_z + \Delta\bar{\tau}_x + B\bar{\sigma}_z - \alpha k_y \bar{\sigma}_x \bar{\tau}_z \,. \tag{134}$$

p. 49

This has by construction a PHS with

$$\hat{\mathcal{C}} = \bar{\sigma}_y \bar{\tau}_y \hat{\mathcal{K}} \tag{144}$$

$$\hat{\mathcal{C}}^2 = +\bar{\mathbb{1}}_4 \,. \tag{145}$$

Additionally, just like in the case without SOC, there is a TRS. But as there is a linear term in momentum, it is not just given by complex conjugation. Instead we have

$$\hat{\mathcal{T}} = \bar{\sigma}_x \hat{\mathcal{K}} \tag{146}$$

$$\hat{\mathcal{T}}^2 = +\bar{\mathbb{1}}_4 \,. \tag{147}$$

Combining this and referring to Table 2, we conclude that this system belongs to class BDI, which can have topology in one dimension with a $\mathbb{Z}$ invariant. Due to the presence of both TRS and PHS, the system also has a CS. With this information, we can refer to the literature in Ref. [79] where we find that the invariant is given by a winding number.[25] The chiral symmetry makes it possible to write the Hamiltonian in a block-*off*-diagonal form

$$U\bar{H}_{1\text{d},z}(k_y)U^\dagger = \begin{pmatrix} 0 & A(k_y) \\ A^\mathrm{T}(-k_y) & 0 \end{pmatrix} \tag{148}$$

$$U = \exp\left(-\mathrm{i}\frac{\pi}{4}\bar{\sigma}_x\bar{\tau}_x\right) \tag{149}$$

$$A = \mathrm{i}\begin{pmatrix} -k\alpha - \mathrm{i}\Delta & \frac{k^2}{2m} - \mu + B \\ \frac{k^2}{2m} - \mu - B & -k\alpha - \mathrm{i}\Delta \end{pmatrix} \tag{150}$$

by a unitary transformation U with a real matrix $A(k) \in \mathbb{R}^{2\times 2}$. This transformation is not unique, but this freedom does not affect the topological classification. The invariant is then given by[114] the winding of the determinant of $A(k_y)$ in the complex plane. For our choice of transformation, the determinant is given by

---

[25]We follow [114] for this discussion.

$$\det(A(k_y)) = \left(\frac{k_y^2}{2m} - \mu\right)^2 + \Delta^2 - B^2 - k_y^2\alpha^2 - 2ik_y\alpha\Delta\,. \tag{151}$$

We can extract some more information about the direction of this in the complex plane from the fact that all parameters are real. The only term contributing to the imaginary part $-2ik_y\alpha\Delta$ is linear in k_y. Thus, the determinant has a positive imaginary part, exactly if k is positive and vice versa. From this, it follows that the winding number can only ever be 0 or 1. The two points of highest symmetry are $k_y = 0$ and $k_y = \pm\infty$. In fact, we contract the k_y-space to form a circle S_1 instead of a line, which can be understood from starting at a lattice, whose k_y-space is the first Brillouin zone and thus periodic. We keep this periodicity, that makes k_y-space a circle, and make the continuum limit, which takes the lattice constant to zero and hence the edge of the Brillouin zone to infinity. Looking at the two high symmetry points, normalizing the determinant yields

$$\frac{\det(A(0))}{|\det(A(0))|} = \frac{\Delta^2 + \mu^2 - B^2}{|\Delta^2 + \mu^2 - B^2|} = \operatorname{sign}(\Delta^2 + \mu^2 - B^2) \tag{152}$$

$$\lim_{k_y \to \pm\infty} \frac{\det(A(k_y))}{|\det(A(k_y))|} = 1\,. \tag{153}$$

So, in summary, how often the determinant winds around the origin on the path from $-\infty$ to $+\infty$ is only determined by the value at zero. For fields larger than the critical field $B_c = \sqrt{\Delta^2 + \mu^2}$, it winds once, otherwise zero times.

3.3.4 Field Orientation

So far, the field in the wire is pointing strictly in z-direction. A natural extension of the discussion is a generalization for an arbitrary direction. The only part of the Hamiltonian from Equation (134) that depends on the orientation in spin-space is the SOC term, which is proportional to $\bar{\sigma}_z$. Therefore, we can apply a rotation along this axis by some angle φ with $\bar{S}_\varphi \equiv \exp(i\varphi\bar{\sigma}_x)$. Consequently, any field in the y-z-plane can be mapped to the Hamiltonian from Equation (134). As $\bar{S}_\varphi$ is a unitary transformation, it cannot change the topology (see the symmetry discussion in Section 2.2.3) and hence all fields in the y-z-plane exhibit the topology discussed before.

A field in x-direction, on the other hand, is different. Before going into the more complicated symmetry analysis, it is insightful to once again start by examining the spectrum. The Hamiltonian is given by

$$\bar{H}_{1\mathrm{d},x} = \left(\frac{k_y^2}{2m} - \mu \right) \bar{\tau}_z + \Delta \bar{\tau}_x + B \bar{\sigma}_x - \alpha k_y \bar{\sigma}_x \bar{\tau}_z \tag{154}$$

and has the eigenvalues

$$E_x = sB \pm \sqrt{\Delta^2 + \left(\varepsilon_{k_y} - sk_y\alpha \right)^2} \,, \ s = \pm 1 \,. \tag{155}$$

In the same way as before for the z-direction, these spectra are plotted in Figure 13 for some reasonable example values. This is already significantly different to the behaviour with fields perpendicular to the x-direction (like in Figure 12). There is still a gap below B_c that closes, but now it does not reopen. This means that, at least for the presented set of parameters, there is no topology here anymore. We again can pose similar questions as before:

1. Is the gap always closed at $B = B_\mathrm{c}$?
2. Is the gap always closed above?

The first one is simple to answer by looking at $k_y = 0$. There we get from Equation (155)

$$E_x \Big|_{k_y=0} = sB \pm \sqrt{\Delta^2 + \mu^2} \,, \tag{156}$$

which indeed goes to zero at $B = B_\mathrm{c}$. Thus, the answer to the first question is indeed "yes". The second part can be solved by looking at the intervals in which the terms lie, just like before. As we are above B_c, B is always larger than the minimum of the root $\sqrt{\Delta^2 + \left(\varepsilon_{k_y} - sk_y\alpha \right)}$ which is at most $\sqrt{\Delta^2 + \mu^2}$ as this is the value at $k_y = 0$. Thus, combined with the fact that the root describes a continuous function that is unbounded from above, there is always a point where the root takes exactly the same value as B. At this point, the gap is closed. As no part of this argument was dependent on the value of α, the answer to the second question is also "yes".
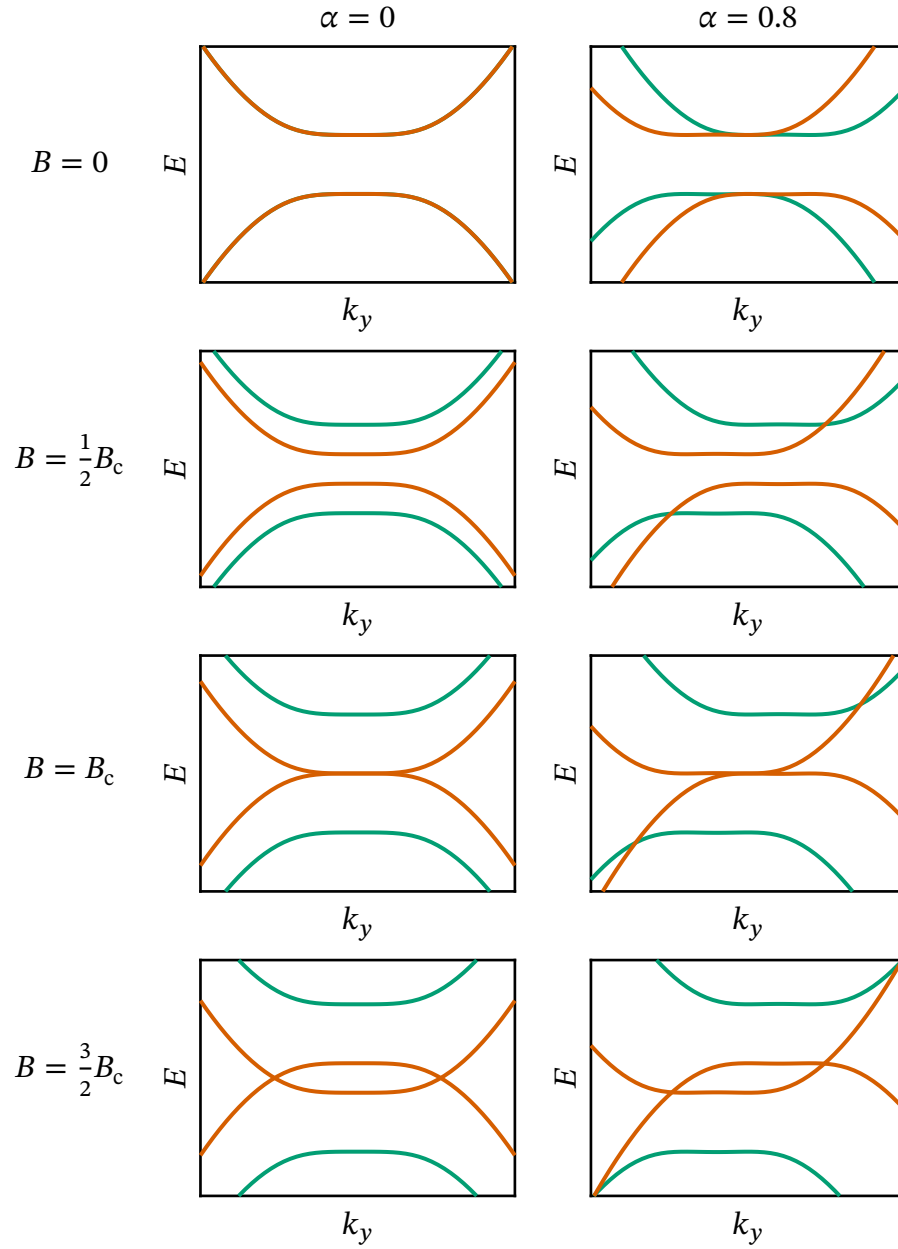
Figure 13: Spectrum of a one-dimensional s-wave superconductor along the y-axis in a constant Zeeman field in x-direction, described by Equation (154) with $\Delta = 0$, $m = 1$ and $\mu = 0$. From top to bottom the field is increased and the spectra with and without SOC are compared. This shows that without SOC, the gap does not open up again, hence no topology can be observed.

While the spectrum analysis was intuitive again, it is also insightful to tackle this problem from a symmetry viewpoint. The Hamiltonian is still given by

$$\bar{H}_{1d,x} = \left(\frac{k_y^2}{2m} - \mu\right)\bar{\tau}_z + \Delta\bar{\tau}_x + B\bar{\sigma}_x - \alpha k_y \bar{\sigma}_x \bar{\tau}_z \qquad (154)$$

Due to the field lying in the plane, there is only one spin Pauli matrix $\bar{\sigma}_x$ appearing. This means, we can, similar to the case with the field in the y-z-plane, but without SOC, write the Hamiltonian as a block-diagonal matrix in the eigenspace of $\bar{\sigma}_x$. The blocks are

$$\bar{H}_{1d,x,\pm} = \left(\frac{k_y^2}{2m} - \mu \mp k_y \alpha\right)\bar{\Sigma}_z + \Delta\bar{\Sigma}_x \pm B\bar{\mathbb{1}}_2 . \qquad (157)$$

This matrix has no PHS, but TRS with a sign of $+1$, which puts it into the in one dimension trivial class AI.

So, in conclusion, the superconducting s-wave wire along the y-axis with SOC in x-direction and a Zeeman field has a topological phase only if this field is perpendicular to the SOC direction in spin-space.

3.3.5 Extension to Two Dimensions

While wires are interesting, this work is concerned with two-dimensional materials. Thus, we need to extend this discussion to two dimensions, which can be imagined like a stacking of the wires from the previous section. This is only an aid, though, as we still stay in a continuum picture. The coupling in this additional direction should look the same as the one along the wire, and also contain SOC, hence resulting in the Hamiltonian

$$\bar{H}_{2d} = \left(\frac{k_x^2 + k_y^2}{2m} - \mu\right)\bar{\tau}_z + \Delta\bar{\tau}_x + \boldsymbol{B}\cdot\bar{\boldsymbol{\sigma}} + \alpha(k_x\bar{\sigma}_y - k_y\bar{\sigma}_x)\bar{\tau}_z \tag{158}$$

$$\bar{\boldsymbol{\sigma}} = \begin{pmatrix}\bar{\sigma}_x \\ \bar{\sigma}_y \\ \bar{\sigma}_z\end{pmatrix}. \tag{159}$$

Here, we have not fixed the direction of the field yet. We only need to distinguish two cases: in-plane and out-of-plane fields in relation to the x-y-plane. This stems from the fact that the Hamiltonian in Equation (158) is rotational invariant around the z-axis.[26] The kinetic term depends solely on the amplitude of the wave vector in this plane. For SOC, this is also true and easier to see, when we rewrite it as $\alpha\left(\boldsymbol{k}\times\bar{\boldsymbol{\sigma}}\right)\boldsymbol{e}_z$. Thus, we can rotate in the x-y-plane without affecting the problem. Without loss of generality, we choose to analyse a field in y- and z-direction to cover both cases.

Out-of-Plane Fields

We start with the, as we will soon see, simpler case of out-of-plane fields. No matter in which direction of the plane we look here, the system looks the same as the topological wire from before. The eigenvalues are given by

$$\begin{aligned}E_{\pm\pm}&\Big|_{\boldsymbol{B}=B_z\boldsymbol{e}_z}\\ &= \pm\sqrt{B^2 + k^2\alpha^2 + \Delta^2 + \varepsilon_k^2 \pm 2\sqrt{B^2\left(\Delta^2 + \varepsilon_k^2\right) + k^2\alpha^2\varepsilon_k^2}} \end{aligned} \tag{160}$$

$$\varepsilon_k = \frac{k^2}{2m} - \mu \tag{161}$$

$$k = \sqrt{k_x^2 + k_y^2}. \tag{162}$$

These have the same form as the ones from Equation (135), just with the magnitude of the wave vector, hence allowing us to apply the results of the one-dimensional discussion about the spectrum. Thus, the system has a gap, that closes at $|B_z| = \sqrt{\Delta^2 + \mu^2}$ and opens in both directions around this point. From now on, we again assume that $B_z > 0$. Symmetry-wise, the Hamiltonian

---

[26]The rotation has to be transformed both for real and spin space.

only has a PHS, because making it completely real is impossible due to the appearance of all three spin Pauli matrices $\bar{\sigma}_i$. Thus, we are in class D, which has a $\mathbb{Z}$ invariant in two dimensions (see Table 2). Following Ref. [79], this invariant is the Chern number

$$\mathrm{Ch} = -\frac{\mathrm{i}}{2\pi} \sum_{E_n<0} \int \mathrm{d}\boldsymbol{k} \, \varepsilon_{ijl}\partial_{k_j}\left(\boldsymbol{\psi}_n^{\dagger}(\boldsymbol{k})\,\partial_{k_l}\boldsymbol{\psi}_n(\boldsymbol{k})\right). \tag{163}$$

where the sum is going over occupied states, which correspond in this case to states with negative energy. The eigenstates of this Hamiltonian are complicated, so we perform this calculation numerically. Directly evaluating the expression is too unstable numerically. Thus, we instead calculate the Chern number by summing over plaquets. Assuming a discretisation of the $\boldsymbol{k}$-space on a lattice with spacing κ and size $N \times N$, the Chern number can also be obtained with[115]

$$\mathrm{Ch} = -\frac{1}{2\pi} \sum_{E_n<0} \sum_{i_x=1}^{N-1} \sum_{i_y=1}^{N-1} \arg\left(B_{n;i_x,i_y}\right) \tag{164}$$

$$B_{n;i_x,i_y} \equiv \left(\boldsymbol{\psi}_{n;i_x,i_y}^{\dagger}\boldsymbol{\psi}_{n;i_x+1,i_y}\right)\left(\boldsymbol{\psi}_{n;i_x+1,i_y}^{\dagger}\boldsymbol{\psi}_{n;i_x+1,i_y+1}\right)$$

$$\left(\boldsymbol{\psi}_{n;i_x+1,i_y+1}^{\dagger}\boldsymbol{\psi}_{n;i_x,i_y+1}\right)\left(\boldsymbol{\psi}_{n;i_x,i_y+1}^{\dagger}\boldsymbol{\psi}_{n;i_x,i_y}\right) \tag{165}$$

$$\boldsymbol{\psi}_{n;i_x,i_y} \equiv \boldsymbol{\psi}_n(\kappa(i_x\boldsymbol{e}_x + i_y\boldsymbol{e}_y)). \tag{166}$$

We evaluate this for $\Delta = 1, \alpha = 0.3, m = 1$ and a lattice in k-space of size 80×80 with a step size of 80. The results are shown in Figure 14, where the topological phase above $B_c = 1$ is characterized by a Chern number of 1 and the trivial one by a value of 0. Therefore, the numerical calculation shows the behaviour that we expected from the gap analysis.

In-Plane Fields

This leaves us with the in-plane field situation. Here, we also stack one-dimensional wires along the x-direction, but this time with a field in y-direction. The cuts of the Hamiltonian, and thus also of the spectrum, along $k_x = 0$ and $k_y = 0$ look, up to a rotation in spin-space, exactly like the one-dimensional wires we discussed before. Especially, as the cut along $k_y = 0$ has the same form as the trivial Hamiltonian from Section 3.3.4, the two-dimensional system also has to be trivial and gapless.
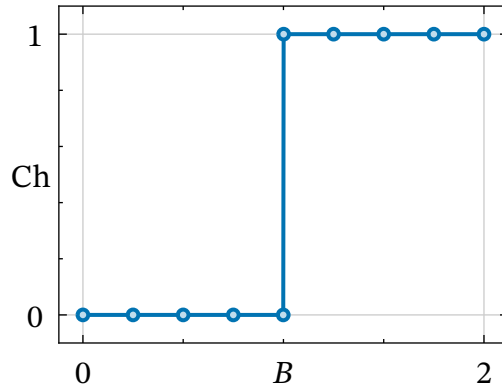
Figure 14: Chern numbers for a constant out-of-plane field for $\Delta = 1$, $\alpha = 0.3$, $m = 1$ and a lattice in k-space of size 80×80 with a step size of 80.

But this does not mean that there are no topological effects and no edge states at all. Instead, we can treat this setup by applying the concept of *weak topology*[72]. The name is a bit misleading, as it originates from the belief that this class of systems is unstable regarding all disorder[72]. This later turned out to be wrong[116,117] and a more appropriate distinction between the two cases is their anisotropy[117]. The naming still stayed, though, and thus we are also using it in this work. From the point of anisotropy, the connection to our problem is more straightforward. If we put the field inside the plane of the layers, we break the rotational invariance around the z-axis we had with out-of-plane fields, leading to a different behaviour parallel and perpendicular to the field direction.

From our discussion before, we know that the system is gapless. Therefore, there is no strong topology to be found. Weak topology can be analysed in a very similar way to strong topology, but by going down one dimension. This means, we get two weak topological indices, ν_x and ν_y, which correspond to the strong indices of one-dimensional wires, that are "stacked". The respective Hamiltonians are obtained by setting $k_x = 0$ for ν_y and $k_y = 0$ for ν_x. We can directly conclude that $\nu_x = 0$ as it is exactly the Hamiltonian from Equation (154) discussed in Section 3.3.4. Equivalently, ν_y is the invariant from Section 3.3.3. Thus, if the field is above the critical field $B_c = \sqrt{\Delta^2 + \mu^2}$, the system shows *weak* topology in y-direction. This does result in edge states in a finite system, but only at edges that are perpendicular to the y-direction (see Figure 15). This means, we have to slightly adapt the scheme portrayed in Section 3.3.2. In Figure 15, the updated scheme depending on the field direction is visualized.
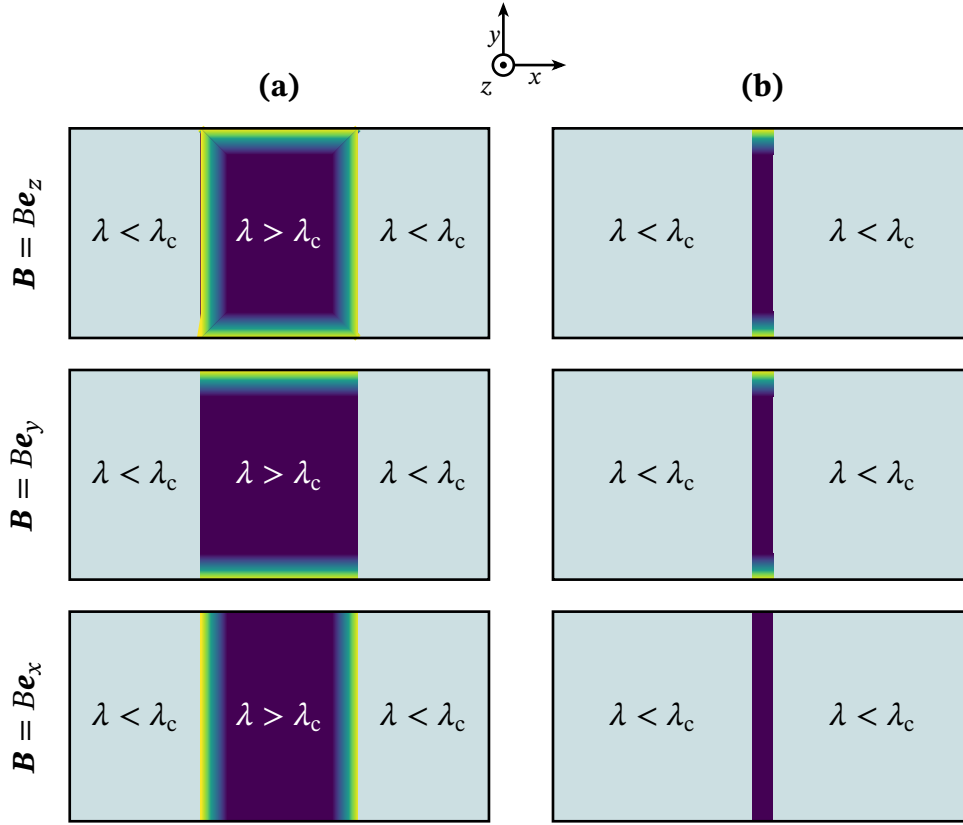
Figure 15: Restriction of the topological region from a smaller rectangle
(a) up to an effectively one-dimensional channel (b) for different field
directions. For out-of-plane (z, first row) and y-direction, the channel
can host edge states, but not for x-oriented fields.

Due to the anisotropic nature of the weak topology with in-plane fields, it is
essential to choose the orientation appropriately, namely in y-direction (middle
row in Figure 15). This means that the fields are parallel to the domain wall itself.
Otherwise, with fields in-plane, but perpendicular to the domain wall (bottom
row in Figure 15), the edge states of the two-dimensional region hybridize in
the process of making the region thinner and effectively one-dimensional.

Physical Implications

In reality, out-of-plane fields are problematic, because of the need of rather
large fields. Due to the critical Zeeman energy being at least as large as the
superconducting gap, there is a big risk of destroying the superconducting
state[118,119]. Moreover, the superconductor would create screening currents

and thus shield the magnet from the fields. Because of this, in-plane fields are desired and even have been argued to be necessary for observing topological features[119,120]. Contrary to the proposals involving skyrmions, 2π domain walls can be flipped in-plane. As we have seen before, we can still get topology with in-plane fields. But their orientation is a crucial factor. Thus, when taking all factors into account, the only possible solution for finding MBSes is with in-plane fields, which are parallel to the domain wall.

3.3.6 Necessary Field Conditions

Now that we understand the topology of the regions in Figure 11, we can make some basic restrictions of the parameter space without making specific assumptions about the origin of these regions, which we do in the following sections. To shortly summarize the result of the previous sections, the parameter λ, which tunes the system between topological and trivial regimes, is here the Zeeman field and has a critical value of $B_{\mathrm{c}} = \sqrt{\Delta^2 + \mu^2}$.

While there are many parameters in the system, the most interesting ones are the strength of the external field and the amplitude of the field coming from the magnetisation as those are the main sources of switching the topology.

The invariant discussed before, just like the eigenvalues, -vectors and gap, can only be calculated numerically. Therefore, the aim is to simplify the problem to get a more intuitive, but also only rough, restriction on the parameter range. For this, we ignore the effects coming from gradients and only apply the topology arguments we discussed for constant fields before, locally. This means that we assume that the topology is not affected at all by effects of the rotation of the field. We will discuss at the end of the section with the help of a spin-alignment transformation (SAT), which effects are neglected by this.

The Hamiltonian is still given by

$$\hat{H} = \left(-\frac{\hat{\mathbf{V}}^2}{2m} - \mu\right)\bar{\tau}_z + \Delta\bar{\tau}_x - J\boldsymbol{M}(x)\cdot\bar{\sigma} + B\bar{\sigma}_y + i\alpha(\hat{\mathbf{V}}\times\bar{\sigma})\bar{\tau}_z \quad (131)$$

$$\bar{\sigma}_i = \bar{\bar{\mathbb{1}}}_2 \otimes \bar{\Sigma}_i$$

$$\bar{\tau}_i = \bar{\Sigma}_i \otimes \bar{\bar{\mathbb{1}}}_2$$

$$\boldsymbol{M}(x) = M_0\begin{pmatrix} \sin(\theta(x)) \\ \cos(\theta(x)) \\ 0 \end{pmatrix} \quad (132)$$

$$\theta(x) = 2\arctan\left(\frac{\sinh\left(\frac{x}{x_0}\right)}{\sinh\left(\frac{w}{x_0}\right)}\right) - \pi. \quad (133)$$

To repeat the most important result of the previous result, the system is topological when the Zeeman field, which is here the total compound of the external field B and a contribution from the magnetic layer $-J\boldsymbol{M}(x)$, surpasses $B_c = \sqrt{\Delta^2 + \mu^2}$. We do want the region inside the wall to be topological, while everything far away from it should be trivial. Examining the profiles, we have for the field in the center (B_0) and far away (B_∞)

$$B_0 = \lim_{x\to 0} B - JM_y(x) = B + JM_0 \quad (168)$$

$$B_\infty = \lim_{x\to\pm\infty} B - JM_y(x) = B - JM_0, \quad (169)$$

where we neglected the other components, as they vanish anyway. Combining these with the knowledge of the critical field results in the following restrictions

$$\text{(I)} \quad |B + JM_0| > B_c \quad (170)$$

$$\text{(II)} \quad |B - JM_0| < B_c. \quad (171)$$

It is important to note, that condition (II) is much stronger than condition (I), as we have made no assumptions. Condition (I) depends on additional effects from field rotations and gradients that are neglected here.

Visually, they result in the region presented in Figure 16 (a) forming a half-infinite rectangle. Importantly, this is not the actual phase boundary, which, as we will see later from numerical calculations, is more complicated, but completely contained in the region shown here.

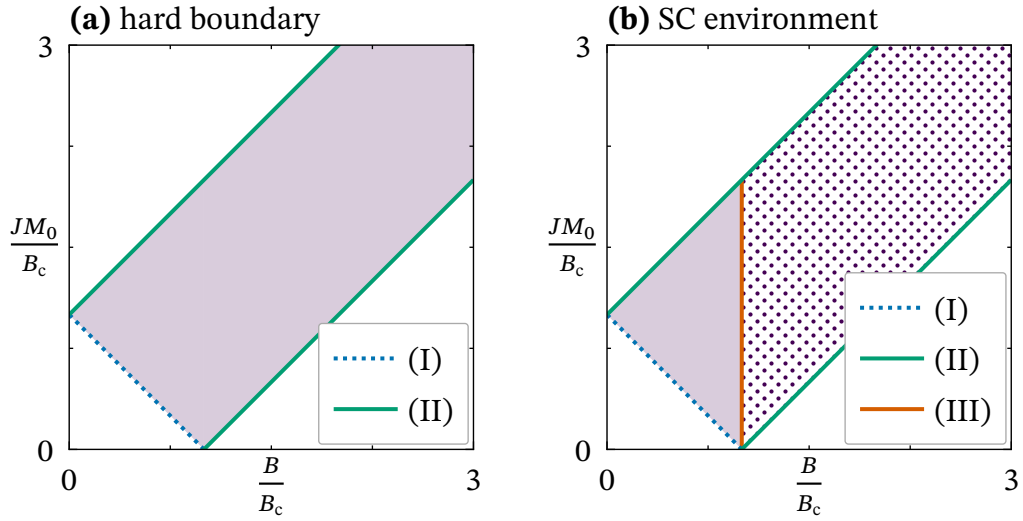**(a)** hard boundary   **(b)** SC environment

Figure 16: Estimated constraints on the topological region with hard boundaries **(a)** and with a superconducting environment **(b)**. The lines represent the results of requiring the total field to be larger than the critical field inside the wall ((I), Equation (170)) and below outside ((I), Equation (171)). The resulting overlap is shaded and represents the region where it is possible to find topology. With the superconducting environment in **(b)** the region where the environment is topological is patterned. This region is a result of condition (III) from Equation (172).

From this viewpoint, we can also discuss the effect of a superconducting environment. This is basically equivalent to a large superconducting sample with a smaller magnet on top. See Figure 17 for a visualization of the setup. This causes a potential problem at high external fields. If the external field B exceeds the critical field B_c, this environment becomes topological as well and the wire does not have a boundary with a trivial state any more, thus preventing zero-dimensional MBS from existing. Instead, one-dimensional edge states would form in the environment. Therefore, we can formulate a third condition which is only relevant in the presence of a superconducting environment which reads

$$\text{(III)} \quad |B| < B_c. \tag{172}$$

In Figure 16 (b), the resulting region is marked as well. This means, that with a superconducting environment, the possible topological region is severely restricted.
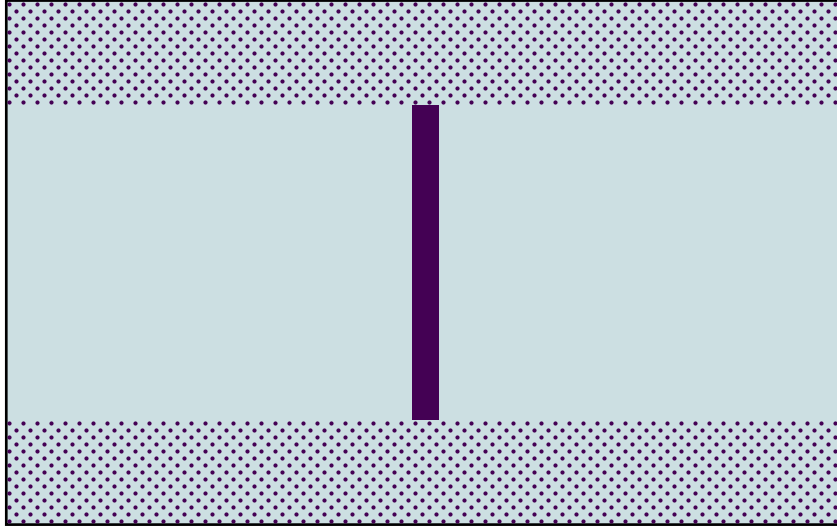
Figure 17: Sketch of the setup with a superconduction environment, which is marked with a dot-pattern. In the environment, the magnet has no effect and the external field B is the only contribution to the Zeeman term.

Field Rotation Effects

We also want to shortly comment on the effect of the so far neglected effects of the rotation of the fields. For this, we apply a SAT, which is a method that has been applied to similar systems in the literature[19,32,121–124]. The idea behind it is to locally rotate the field to a certain axis and thus shift the position dependent part away from the field to other quantities. We apply this to the magnetisation profile

$$\boldsymbol{M}(x) = M_0 \begin{pmatrix} \sin(\theta(x)) \\ \cos(\theta(x)) \\ 0 \end{pmatrix} \tag{132}$$

$$\theta(x) = 2\arctan\left(\frac{\sinh\left(\frac{x}{x_0}\right)}{\sinh\left(\frac{w}{x_0}\right)} \right) - \pi. \tag{133}$$

We already have the angle $\theta(x)$ in the x-y-plane. Therefore, if we rotated by $-\theta(x)$ around the z-axis in spin-space, the magnetisation will point into the positive z-direction everywhere. But we do not just have the magnetisation, but also the external field, which we also need to consider. Consequently, we need to rotate by the angle, that the total field exhibits. We thus get

$$\boldsymbol{B}_{\mathrm{tot}}(x) \equiv B\boldsymbol{e}_y - J\boldsymbol{M}(x) \equiv B_{\mathrm{tot}}(x)\begin{pmatrix} \sin(\vartheta(x)) \\ \cos(\vartheta(x)) \\ 0 \end{pmatrix} \tag{174}$$

$$\vartheta(x) = \arctan\left(\frac{B - JM_0\cos(\theta(x))}{JM_0\sin(\theta)}\right). \tag{175}$$

With this, we have the proper angle for the transformation, which can be represented with the unitary matrix

$$\bar{S} = \exp\left(-\frac{\mathrm{i}}{2}\vartheta(x)\bar{\sigma}_z\right). \tag{176}$$

In addition to the more straightforward rotation of the spin-space matrices $\bar{\sigma}_i$, the more interesting effects arise from the derivative terms. The only relevant derivative is the one in x-direction, which transforms as

$$\bar{S}\partial_x\bar{S}^\dagger = \partial_x\bar{\mathbb{1}}_4 + \bar{S}(\partial_x\bar{S}^\dagger) = \partial_x\bar{\mathbb{1}}_4 + \frac{\mathrm{i}}{2}\vartheta'(x)\bar{\sigma}_z. \tag{177}$$

With this knowledge, we can transform the Hamiltonian and analyse the form of the extra terms appearing. The transformed Hamiltonian reads[19]

$$\hat{\bar{H}}_{\mathrm{SAT}} = \left(-\frac{\hat{\boldsymbol{\nabla}}^2}{2m} - \mu_{\mathrm{eff}}\right)\bar{\tau}_z + \Delta\bar{\tau}_x + B_{\mathrm{tot}}(x)\bar{\sigma}_y + (\hat{\boldsymbol{s}}_{\mathrm{eff}}\,\bar{\boldsymbol{\sigma}})\bar{\tau}_z \tag{178}$$

$$B_{\mathrm{tot}} \equiv |B\boldsymbol{e}_y - J\boldsymbol{M}(\boldsymbol{r})| \tag{179}$$

$$\mu_{\mathrm{eff}} \equiv \mu - \frac{1}{8m}\vartheta'(x)^2 \tag{180}$$

$$\hat{\boldsymbol{s}}_{\mathrm{eff}} \equiv +\mathrm{i}\alpha\begin{pmatrix} -\cos(\vartheta(x))\partial_y - \sin(\vartheta(x))\partial_x \\ \cos(\vartheta(x))\partial_x - \sin(\vartheta(x))\partial_y \\ 0 \end{pmatrix}$$

$$\frac{\mathrm{i}}{2}\vartheta'(x)\begin{pmatrix} \alpha\cos(\vartheta(x)) \\ \alpha\sin(\vartheta(x)) \\ -\frac{1}{m} \end{pmatrix}. \tag{181}$$

As we have learned before, that the SOC is not relevant for the existence of the topology as long as it is finite, the correction to the chemical potential is more relevant as it influences the critical field. Because we have an analytic expression for the profile of the magnetic texture, we can evaluate this more concretely. Differentiating yields

$$\vartheta'(x) = JM_0\theta'(x)\frac{JM_0 - B\cos(\theta(x))}{B^2 + JM_0^2 - 2BJM_0\cos(\theta(x))} \tag{182}$$

$$\theta'(x) = \frac{2}{x_0}\frac{\cosh\left(\frac{x}{x_0}\right)\mathrm{csch}\left(\frac{h}{x_0}\right)}{1 + \mathrm{csch}\left(\frac{h}{x_0}\right)^2\sinh\left(\frac{x}{x_0}\right)^2}. \tag{183}$$

For simplicity, we restrict most of our analysis to the case of $x_0 \ll h$. In this limit, the correction to the chemical potential vanishes exponentially, justifying our previous discussion of necessary conditions. In section Section 3.6, we will present a short numerical evaluation of other limits.

3.3.7 Topology With a Magnetic Texture

Now that we developed some intuition about the topological idea of this proposal, we are ready to analyse the topology more rigorously. We assume that the texture only changes in the x-direction (also refer to Section 2.3) and that the system in periodical in the y-direction. The aim is still to get MBSes in the system, meaning we have a zero-dimensional edge state. One possible angle to look at it is in terms of a two-dimensional system, which would be hosting what is typically referred to as *higher-order topology* because the edge state is more than one dimension — in this case two — lower than the dimensionality of the system.

Another, more convenient way for us, is to view the x-direction as an artificial dimension and just a big unit cell. To really get what this means, it is educational to discuss a discretized version of the problem. In Figure 18, the resulting grid is visualized. We have N_x points — here 11 — in the x-direction, resulting in a unit cell size of N_x. With that, we can only describe topology in y-direction, which is our goal anyway. But this makes it possible to just analyse it in the framework of the strong topology of a one-dimensional system instead of a higher-order topology of a two-dimensional system, which is much simpler.
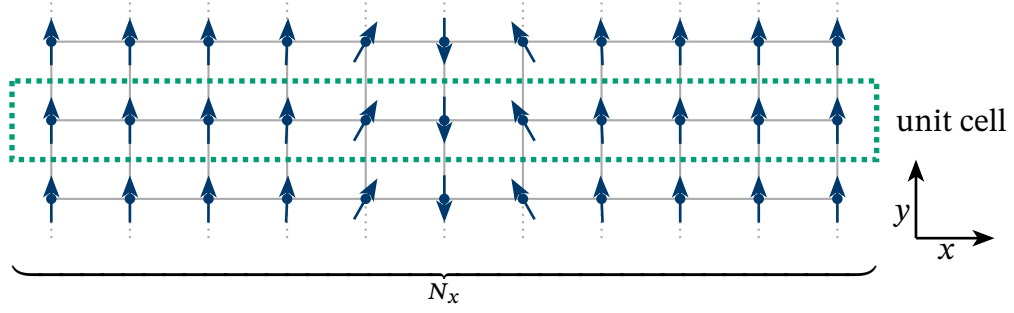
Figure 18: Schematic representation of a discretized system with a texture that only changes in the x-direction and is translational invariant in the y-direction. This can be described as a one dimensional system with a unit cell of size N_x.

Writing down the Hamiltonian in k_y-momentum space, we get

$$\hat{H}_{\text{tex}}(k_y) = \left(\frac{k_y^2 - \partial_x^2}{2m} - \mu\right)\bar{\tau}_z + \Delta\bar{\tau}_x - J\boldsymbol{M}(x) \cdot \bar{\boldsymbol{\sigma}} + B\bar{\sigma}_y$$
$$-\alpha(\mathrm{i}\partial_x\bar{\sigma}_y + k_y\bar{\sigma}_x)\bar{\tau}_z \tag{184}$$

The only relevant symmetry here is the usual PHS with $\hat{\mathcal{C}} = \bar{\sigma}_y\bar{\tau}_y\hat{\mathcal{K}}$ and thus $\hat{\mathcal{C}}^2 = +1$. Consequently, we are in symmetry class D, which has a $\mathbb{Z}_2$ invariant in one-dimension[79]. Following the literature, this invariant is given by[27]

$$\nu = \text{sign}\left(\text{Pf}\left(\hat{H}_{1,\text{bulk}}(0)\right)\right)\left(\lim_{k_y \to \infty} \text{sign}\left(\text{Pf}\left(\hat{H}_{1,\text{bulk}}(k_y)\right)\right)\right) \tag{185}$$

$$\hat{H}_{1,\text{bulk}} \equiv \bar{U}\hat{H}_{\text{bulk}}(0)\bar{U}^\dagger \tag{186}$$

$$\bar{U} \equiv \frac{1}{2}\begin{pmatrix} 1 & 0 & 0 & -1 \\ 0 & 1 & 1 & 0 \\ \mathrm{i} & 0 & 0 & \mathrm{i} \\ 0 & \mathrm{i} & -\mathrm{i} & 0 \end{pmatrix}. \tag{187}$$

The unitary matrix $\bar{U} \in \mathbb{C}^{4\times4}$ is meant to be acting on sites separately and rotates the Hamiltonian into a skew symmetric form $\hat{H}_{1,\text{bulk}}^{\mathrm{T}} = -\hat{H}_{1,\text{bulk}}$. The transformation is physically representing a transformation into the Majorana

---

[27]In the referenced literature, the Hamiltonian is evaluated at the border of the Brillouin zone. Here, we took the limit of lattice spacing to zero and thus evaluate it at $k_y \to \infty$.

basis (see Section 2.2.3).[28] For this form, a Pfaffian can be calculated. The Pfaffian is a quantity similar to the determinant of a matrix, but only defined for skew symmetric matrices. In a certain sense, the Pfaffian can be seen as a square root of the determinant because squaring it yields the determinant. It can defined recursively for a skew symmetric matrix $\bar{A} \in \mathbb{R}^{2N \times 2N}$ [125]

$$\mathrm{Pf}(\bar{A}) = \sum_{i=2}^{2N} (-1)^i a_{1,i} \, \mathrm{Pf}(\bar{A}_{1,i}) \,. \tag{188}$$

The notation $\bar{A}_{i,j}$ represents the matrix $\bar{A}$ without rows and columns i and j. In general, calculating a Pfaffian of a large matrix is computational expensive and runs into the risk of numerical overflow. For this reason, the optimized library `pfapack`[125] is used. Additionally, the number of points in real space has to be limited in cases where numerical issues arise.

3.4 One-Dimensional Bound States

The basis of the one-dimensional channel is formed by the bound states on the domain wall in the bulk system. In this section, we have a deeper look into their structure. As a first step, we analyse the decay far away from the wall. There, the effect of the domain wall is negligible, and we can just assume that the field is given by B_∞ (Equation (169)). As we are in the bulk system, the bound states can be written as $\varphi_n(x, k_y)$, and we can treat k_y just as a parameter. In this limit, the Hamiltonian is given by

$$\hat{H}_\infty = \left(\frac{k_y^2 - \partial_x^2}{2m} - \mu \right) \bar{\tau}_z + \Delta \bar{\tau}_x$$
$$+ \alpha (k_y \bar{\sigma}_x + i\alpha \partial_x \bar{\sigma}_y) \bar{\tau}_z + B_\infty \bar{\sigma}_y \,. \tag{189}$$

In this regime, the system is basically translationally invariant in x-direction, warranting a plane wave ansatz $\varphi_n(x, k_y) = \exp(i k_x x) \varphi_{n,0}$. With that, we can examine the eigenvalue equation for the bound state and obtain a relation between the energy of the bound state ε_b and the wave vector k_x. The bound state energy still needs to be obtained through numerical means. From this, we can extract a length scale λ for the decay

---

[28]Some references, for example Ref. [114], define $\hat{H}_{1,\mathrm{bulk}} = \hat{H}_{\mathrm{bulk}} \bar{\tau}_x$.

$$\lambda = \left| k_{x,\infty} \right|^{-1} . \tag{190}$$

We are not concerned about the sign as only one will be valid on either end to have normalizable states.

As an example, we look at $\mu = 0$, which is what we use in all numerics anyway, and $k_y = 0$ as those restriction allow us to obtain analytical results. In this limit with the plane wave ansatz, the eigenvalue equation reads

$$\left(\frac{k_x^2}{2m} \bar{\tau}_z + \Delta \bar{\tau}_x - \alpha k_x \bar{\sigma}_y \bar{\tau}_z + B_\infty \bar{\sigma}_y \right) \varphi_{b,0} = \varepsilon_b \varphi_{b,0} . \tag{191}$$

Diagonalizing the right hand side yields

$$\varepsilon_b = a B_\infty + b \sqrt{ \left(\frac{k_x^2}{2m} \right)^2 + a \frac{\alpha k_x^3}{m} + \alpha^2 k_x^2 + \Delta^2 } \tag{192}$$

$$a = \pm 1 \tag{193}$$
$$b = \pm 1 . \tag{194}$$

We do not know which of the four eigenvalues correspond to the bound state, but we also do not have to resolve this issue at this stage. Instead, we solve this equation for k_x and use two things for selecting the right solution. First, we are looking for bound states, so the wave vector has to have an imaginary part. Secondly, the bound state is inside the gap, and hence we can use the fact that $\varepsilon_b < \Delta$. Additionally, we assume that ε_b is positive. We could also perform the same analysis for the negative energy partner, but due to the particle-hole symmetry in the system, this would not provide any additional information. Because of the square root, Equation (192) is difficult to analyse. Therefore, we rearrange and square both side to arrive at

$$(\varepsilon_b - a B_\infty)^2 = \left(\frac{k_x^2}{2m} \right)^2 + a \frac{\alpha k_x^3}{m} + \alpha^2 k_x^2 + \Delta^2 , \tag{195}$$

where there is no dependence on b anymore, reducing the amount of selection we have to perform. This is a fourth order polynomial in k_x with real coefficients, so by looking for roots, we find the solutions for k_x. In general, fourth order polynomials are analytically solvable, but the expressions are lengthy. Luckily, though, in this case the solutions are simpler because we can rewrite Equation (195) to have the form

$$0 = k_x^4 + 4c_0 k_x^3 + 4c_0^2 k_x^2 + c_1 \tag{196}$$

$$c_0 \equiv am\alpha \tag{197}$$

$$c_1 \equiv 4m^2\big(\Delta^2 - (\varepsilon_b - aB_\infty)^2\big). \tag{198}$$

The four possible solutions to this can be written as

$$k_{x,\infty} = -c_0 \pm \sqrt{c_0^2 \pm i\sqrt{c_1}}$$

$$= -am\alpha \pm m\sqrt{\alpha^2 \pm 2i\sqrt{\Delta^2 - (\varepsilon_b - aB_\infty)^2}}. \tag{199}$$

As mentioned before, to describe a bound state, the imaginary part of this has to be non-vanishing. c_0 is real, which is why the imaginary part has to come from the square root term. In general, the imaginary part of a square root of a complex number z can be written, with $r = |z|$ and $\varphi = \arg(z)$ norm and argument of z, as

$$\Im\big(\sqrt{r}\big) = \pm\sqrt{r}\,\Im\big(\exp\big(i\tfrac{\varphi}{2}\big)\big) = \pm\sqrt{r}\sin\big(\tfrac{\varphi}{2}\big)$$

$$= \pm\sqrt{r}\sqrt{\tfrac{1}{2}(1 - \cos(\varphi))}$$

$$= \pm\sqrt{\tfrac{1}{2}(|z| - \Re(z))}. \tag{200}$$

The complex number in this case is the radicant $c_0^2 \pm i\sqrt{c_1}$. From this, we need to know the location in the complex plane, for which we look at a different case.

$c_1 < 0$

For negative c_1, the radicant $c_0^2 \pm i\sqrt{c_1}$ is completely real. The condition of negative $c_1 < 0$ physically means that the field is large enough such that $|\varepsilon_b - aB_\infty| > \Delta$. To have a non-vanishing imaginary part of the wave vector, it has to be negative. Hence, a necessary condition to get a localised state is that

$$(\varepsilon_b - aB_\infty)^2 > \Delta^2 + \frac{m^2\alpha^4}{4} \tag{201}$$

and only the negative sign of the radicant is possible. For reasonable values of $\alpha < 0$, which is true for all values considered in this work, this is not restricting

the parameter range much further than positive c_1 already does. But, as the system has to be in the trivial phase there, the field cannot exceed the critical field of $B_c = \Delta$. As we fixed both ε_b and B_∞ to be positive, Equation (201) can only be satisfied for $a = -1$. This means that the field has to be in the range

$$\sqrt{\Delta^2 + \frac{m^2\alpha^4}{4}} - \varepsilon_b < B_\infty < \Delta. \tag{202}$$

which is only possible for a large enough bound state energy of

$$\varepsilon_b > \sqrt{\Delta^2 + \frac{m^2\alpha^4}{4}} - \Delta. \tag{203}$$

If all these conditions are satisfied, we can get a decay length scale of

$$\begin{aligned}\lambda^{-1} &= \sqrt{-c_1 - c_0^2} \\ &= 2m\sqrt{(\varepsilon_b + B_\infty)^2 - \Delta^2} - m^2\alpha^2. \end{aligned} \tag{204}$$

$c_1 \geq 0$

This corresponds to the physical case of $|\varepsilon_b - aB_\infty| < \Delta$. As the bound state is always inside the gap, this is fulfilled for small enough total fields, which is compatible with the topological arguments because the system should be in the trivial regime which is the case for small total fields. Then $\sqrt{c_1}$ is strictly negative and we have

$$|c_0^2 \pm i\sqrt{c_1}| = \sqrt{c_0^4 + c_1} \tag{205}$$
$$\Re\left(c_0^2 \pm i\sqrt{c_1}\right) = c_0^2. \tag{206}$$

With this, we have

$$\begin{aligned}\lambda^{-1} = |\Im(k_{0,\infty})| &= \sqrt{\frac{1}{2}\left(\sqrt{c_0^4 + c_1} - c_0^2\right)} \\ &= m\alpha\sqrt{\frac{1}{2}\left(\sqrt{1 + \frac{4}{\alpha^4}\left(\Delta^2 - (\varepsilon_b \pm B_\infty)^2\right)} - 1\right)}. \end{aligned} \tag{207}$$

This case is relevant for the topological regime. Therefore, we use this result later for the comparison with the numerical results in Section 3.6.1.

3.5 Exact Diagonalization

In addition to the analytical considerations before, we also performed more brute force numerical calculations. These are done by performing exact diagonalization (ED) on a discretized version of the BdG Hamiltonian (Equation (131)). For simplicity, this discretisation is performed by using finite differences on a square lattice. Refer to Section B.1 for a guide on how to use the software developed for this purpose.

3.5.1 Discretisation

The model Hamiltonian, which was given by

$$\hat{H} = \left(-\frac{\hat{\mathbf{\nabla}}^2}{2m} - \mu\right)\bar{\tau}_z + \Delta\bar{\tau}_x - J\boldsymbol{M}(x)\cdot\bar{\boldsymbol{\sigma}} + B\bar{\sigma}_y + i\alpha(\hat{\mathbf{\nabla}}\times\bar{\boldsymbol{\sigma}})\bar{\tau}_z \quad (131)$$

$$\bar{\sigma}_i = \bar{\bar{\mathbb{1}}}_2 \otimes \bar{\Sigma}_i$$

$$\bar{\tau}_i = \bar{\Sigma}_i \otimes \bar{\bar{\mathbb{1}}}_2$$

$$\boldsymbol{M}(x) = M_0\begin{pmatrix} \sin(\theta(x)) \\ \cos(\theta(x)) \\ 0 \end{pmatrix} \quad (132)$$

$$\theta(x) = 2\arctan\left(\frac{\sinh\left(\frac{x}{x_0}\right)}{\sinh\left(\frac{w}{x_0}\right)}\right) - \pi, \quad (133)$$

p. 45, p. 46

is now put onto a lattice. The relevant space-dependent parts are on the one hand the magnetisation, and on the other hand the derivatives in the kinetic and SOC terms. Let us assume a lattice of size $N_x \times N_y$ with lattice spacing a. On all edges hard boundary conditions are used. We then use indices $i_x \in [0, N_x)$ and $i_y \in [0, N_y)$ to denote the quantities on the lattice. As a first step, vectors in this discretized space no longer consist of four components[29], each of which is a continuous function over real-space. Now, they have $4N_xN_y \equiv D$ complex

---

[29]The number components comes from the fact that we have two spin and two particle-hole options.

components and hence can be represented by elements of $\mathbb{C}^D$. Consequently, the discretized Hamiltonian can be represented as a hermitian matrix $\mathbb{C}^{D \times D}$. Here already the greatest challenge of the numerical calculations becomes evident. When we scale the system size up by a factor f, the number of matrix elements already scales as f^4. This can be somewhat mitigated by using sparse matrices because, as we will see in the following, many elements are indeed zero. Additionally, the fact that we do not need the full spectrum is very helpful as it allows for a faster calculation of eigenvalues. But, we come back to these implementation details later. While we can just work in the D-dimensional space and use indices $i_D \in [0, D)$, for readability we still write separate indices for the Nambu (i_N) and spacial parts (i_x, i_y). They can be converted from and to the flattened version with

$$i_D \equiv 4(i_x + N_x i_y) + i_N \tag{209}$$

$$i_N \equiv i_D \bmod 4 \tag{210}$$

$$i_x \equiv \left\lfloor \frac{i_D}{4} \right\rfloor \bmod N_x \tag{211}$$

$$i_y \equiv \left\lfloor \frac{i_D}{4N_x} \right\rfloor, \tag{212}$$

which counts first Nambu, then in x- and then in y-diretion. Here, $a \bmod b$ is the remainder of the integer division $\frac{a}{b}$ and $\lfloor x \rfloor$ is the largest integer less or equal than x. This order is arbitrary and can also be chosen differently. In total, we have, with yet to determined kinetic ($\bar{T} \in \mathbb{C}^{N_x N_y \times N_x N_y}$), SOC ($\bar{S} \in \mathbb{C}^{D \times D}$) and magnetisation ($\bar{M} \in \mathbb{R}^{3 \times N_x N_y \times N_x N_y}$) terms

$$\bar{h} \psi_n = E_n \psi_n \tag{213}$$

$$
\begin{aligned}
h_{i_D, j_D} \equiv h_{i_N i_x i_y, j_N j_x j_y} = {} & T_{i_x i_y, j_x j_y} \bar{\tau}_{z; i_N, j_N} \\
& + \Delta \delta_{i_x, j_x} \delta_{i_y, j_y} \bar{\tau}_{x; i_N, j_N} \\
& - J \sum_{k=1}^{3} M_{k; i_x i_y} \delta_{i_x, j_x} \delta_{i_y, j_y} \bar{\sigma}_{k; i_N, j_N} \\
& + B \delta_{i_x, j_x} \delta_{i_y, j_y} \bar{\sigma}_{y; i_N, j_N} \\
& + S_{i_N i_x i_y, j_N j_x j_y} .
\end{aligned} \tag{214}
$$

The magnetisation is the most straightforward part to transfer to the lattice, as we just take the value of the magnetisation at the location of the respective lattice point. Thus, we have

$$M_{i;i_x i_y} \equiv M_i(i_x a). \tag{215}$$

The other two quantities (T and S) contain derivatives. We quantize those using first order symmetric finite difference, which approximates derivatives as

$$\partial_x f(x) = \frac{f(x+a) - f(x-a)}{2a} + \mathcal{O}\!\left(\frac{1}{a^2}\right). \tag{216}$$

For the second derivative, we have

$$\partial_x^2 f(x) = \frac{f(x+a) + f(x-a) - 2f(x)}{a^2} + \mathcal{O}\!\left(\frac{1}{a^3}\right). \tag{217}$$

Importantly, we apply this to a vector on the grid, so we have in the cases where we can ignore the boundary

$$(\partial_x \psi)_{i_N i_x i_y} \approx \frac{1}{2a}\left(\psi_{i_N(i_x+1)i_y} - \psi_{i_N(i_x-1)i_y}\right) \tag{218}$$

$$(\partial_x^2 \psi)_{i_N i_x i_y} \approx \frac{1}{a^2}\left(\psi_{i_N(i_x+1)i_y} + \psi_{i_N(i_x-1)i_y} - 2\psi_{i_N(i_x)i_y}\right) \tag{219}$$

and similar statements for the derivatives in y. In the following, we define $\bar{T}$ and $\bar{S}$ such, that this approximation is already applied. With that, we can write

$$
\begin{aligned}
T_{i_x i_y, j_x j_y} = {}& \frac{1}{2ma^2} \underbrace{\delta_{i_y,j_y}\left(\delta_{i_x+1,j_x} + \delta_{i_x-1,j_x} - 2\delta_{i_x,j_x}\right)}_{\approx \partial_x^2} \\
& + \frac{1}{2ma^2} \underbrace{\delta_{i_x,j_x}\left(\delta_{i_y+1,j_y} + \delta_{i_y-1,j_y} - 2\delta_{i_y,j_y}\right)}_{\approx \partial_y^2} \\
& - \mu \delta_{i_x,j_x} \delta_{i_y,j_y} \\
= {}& t \underbrace{\delta_{i_y,j_y}\left(\delta_{i_x+1,j_x} + \delta_{i_x-1,j_x} - 2\delta_{i_x,j_x}\right)}_{\bar{D}_{x;N_x,N_y}} \\
& + t \underbrace{\delta_{i_x,j_x}\left(\delta_{i_y+1,j_y} + \delta_{i_y-1,j_y} - 2\delta_{i_y,j_y}\right)}_{\bar{D}_{y;N_x,N_y}} \\
& - \tilde{\mu} \delta_{i_x,j_x} \delta_{i_y,j_y} \tag{220} \\
\bar{T} = {}& t\left(\bar{D}_{x;N_x,N_y} + \bar{D}_{y;N_x,N_y}\right) - \tilde{\mu}\bar{\mathbb{1}}_d, \tag{221}
\end{aligned}
$$

where we introduced

$$t \equiv \frac{1}{2ma^2} \tag{222}$$

$$\tilde{\mu} \equiv \mu - 4t. \tag{223}$$

This means that the matrix $\bar{T}$ has non-zero entries only on the main and four secondary diagonals. Those four are offset by 4 and $4N_x$ in either direction as a step in x-direction (y-direction) corresponds to a step of 4 ($4N_x$) in the index. Hard boundary conditions make this construction not as straightforward, though, as not all entries along those diagonals are the same. This is caused by the fact, that not every step of 4 in the index is also a single step in x-direction, but instead can wrap around to the next row. For example, for $N_x = 3$, $N_y = 4$, we have

$$\bar{T} = \begin{pmatrix}
\tilde{\mu} & t & 0 & 0 & t & 0 & 0 & 0 & 0 & 0 & 0 & 0 \\
t & \tilde{\mu} & t & 0 & 0 & t & 0 & 0 & 0 & 0 & 0 & 0 \\
0 & t & \tilde{\mu} & t & 0 & 0 & t & 0 & 0 & 0 & 0 & 0 \\
0 & 0 & t & \tilde{\mu} & 0 & 0 & 0 & t & 0 & 0 & 0 & 0 \\
t & 0 & 0 & 0 & \tilde{\mu} & t & 0 & 0 & t & 0 & 0 & 0 \\
0 & t & 0 & 0 & t & \tilde{\mu} & t & 0 & 0 & t & 0 & 0 \\
0 & 0 & t & 0 & 0 & t & \tilde{\mu} & t & 0 & 0 & t & 0 \\
0 & 0 & 0 & t & 0 & 0 & t & \tilde{\mu} & 0 & 0 & 0 & t \\
0 & 0 & 0 & 0 & t & 0 & 0 & 0 & \tilde{\mu} & t & 0 & 0 \\
0 & 0 & 0 & 0 & 0 & t & 0 & 0 & t & \tilde{\mu} & t & 0 \\
0 & 0 & 0 & 0 & 0 & 0 & t & 0 & 0 & t & \tilde{\mu} & t \\
0 & 0 & 0 & 0 & 0 & 0 & 0 & t & 0 & 0 & t & \tilde{\mu}
\end{pmatrix} = tD_{x;4,3} + tD_{y;4,3} + \tilde{\mu}\bar{\mathbb{1}}_{12}. \tag{224}$$

The contributions of the *x-derivative* and *y-derivative* are respectively marked with colors. The same method can be applied to the SOC term, which yields

$$S_{i_N i_x i_y, j_N j_x j_y} = S_{x;i_x i_y, j_x j_n}\left(\bar{\sigma}_y \bar{\tau}_z\right)_{i_N, j_N} - S_{y;i_x i_y, j_x j_n}\left(\bar{\sigma}_x \bar{\tau}_z\right)_{i_N, j_N} \tag{225}$$

$$S_{x;i_x i_y, j_x j_y} = i\tilde{\alpha}\delta_{i_y, j_y}\left(\delta_{i_x+1, j_x} - \delta_{i_x-1, j_x}\right) \tag{226}$$

$$S_{y;i_x i_y, j_x j_y} = i\tilde{\alpha}\delta_{i_x, j_x}\left(\delta_{i_y+1, j_y} - \delta_{i_y-1, j_y}\right) \tag{227}$$

$$\bar{S} = i\tilde{\alpha}\left(\bar{D}_{x;N_x, N_y} \otimes \bar{\sigma}_y \bar{\tau}_z - \bar{D}_{y;N_x, N_y} \otimes \bar{\sigma}_x \bar{\tau}_z\right) \tag{228}$$

$$\tilde{\alpha} \equiv \frac{\alpha}{2a}. \tag{229}$$

Putting all together, we write the discretized Hamiltonian as

$$\bar{h} = \bar{T} \otimes \bar{\tau}_z + \bar{\mathbb{1}}_{N_x N_y} \otimes (\Delta \bar{\tau}_x + B \bar{\sigma}_y) - J \sum_{k=1}^{3} M_k \bar{\sigma}_k + \bar{S}$$

$$= \underbrace{\bar{\mathbb{1}}_{N_x N_y} \otimes (\tilde{\mu} \bar{\tau}_z + \Delta \bar{\tau}_x + B \bar{\sigma}_y) - J \sum_{k=1}^{3} M_k \bar{\mathbb{1}}_{N_x N_y} \otimes \bar{\sigma}_k}_{\bar{h}_0}$$

$$+ \underbrace{D_{x;N_x,N_y} \otimes (t \bar{\mathbb{1}}_4 + i \tilde{\alpha} \bar{\sigma}_y) \bar{\tau}_z}_{\bar{h}_x} + \underbrace{D_{y;N_x,N_y} \otimes (t \bar{\mathbb{1}}_4 - i \tilde{\alpha} \bar{\sigma}_x) \bar{\tau}_z}_{\bar{h}_y} \,. \quad (230)$$

This is now a matrix $\mathbb{C}^{D \times D}$, which can be diagonalized numerically.

3.5.2 Bulk System

For the effectively one-dimensional bulk system, we apply a similar scheme. The system is an infinite extension in y-direction and hence is translational invariant in this direction, which we can utilize by making a plane wave ansatz. This is a similar idea to the one we used in Section 3.3. Therefore, instead of the $D \times D$-dimensional matrix with $D = 4 n_x n_y$, we end up with a significantly smaller $D_1 \times D_1$-dimensional matrix, where $D_1 = 4 n_x$, but have the wave vector k_y as a parametric dependence. Again, somewhat arbitrarily, we introduce the index counting pattern

$$i_{D_1} \equiv 4 i_x \quad (231)$$

$$i_N \equiv i_{D_1} \bmod 4 i_x \equiv \left\lfloor \frac{i_{D_1}}{4} \right\rfloor \,. \quad (232)$$

There is a less obvious, but crucial, difference in the kinetic energy. In two dimensions, the chemical potential got a correction $\tilde{\mu} = \mu - 4t$ (see Equation (220) to Equation (223)). To this, both the x- and y-derivatives contributed $2t$ each. Thus, in the one dimensional case, we have $2t$ only, which manifests through

$$T_{1;i_x,j_x} = \underbrace{\frac{1}{2ma^2}}_{t} \underbrace{(\delta_{i_x+1,j_x} + \delta_{i_x-1,j_x} - 2\delta_{i_x,j_x})}_{\approx \partial_x^2} - \mu \delta_{i_x,j_x} \delta_{i_y,j_y}$$

$$\hspace{12cm} (233)$$

$$\bar{T}_1 = t \bar{D}_{x;N_x,1} - \tilde{\mu}_1 \bar{\mathbb{1}}_d \quad (234)$$

$$\tilde{\mu}_1 \equiv \mu - 2t \,. \quad (235)$$

Additionally, we get a constant $\frac{k_y^2}{2m}\bar{\tau}_z$ term. The other affected term is SOC, where the y-derivative is replaced with a constant $-\mathrm{i}k_y$ as well. Hence, for SOC we use

$$\bar{S}_1 = \mathrm{i}\underbrace{\frac{\alpha}{2a}}_{\tilde{\alpha}}\bar{D}_{x;N_x,1} \otimes \bar{\sigma}_y\bar{\tau}_z - \alpha k_y\bar{\sigma}_x\bar{\tau}_z\,. \tag{236}$$

So, in total, we have

$$
\begin{aligned}
\bar{h}_1(k_y) &= \bar{T}_1 \otimes \bar{\tau}_z + \bar{\mathbb{1}}_{N_xN_y} \otimes (\Delta\bar{\tau}_x + B\bar{\sigma}_y) - J\sum_{k=1}^{3} M_k \cdot \bar{\mathbb{1}}_{N_xN_y} \otimes \bar{\sigma}_k + \bar{S}_1 \\
&= \underbrace{\bar{\mathbb{1}}_{N_xN_y} \otimes \left(\left(\tilde{\mu}_1 + \frac{k_y^2}{2m}\right)\bar{\tau}_z + \Delta\bar{\tau}_x + B\bar{\sigma}_y - \alpha k_y\bar{\sigma}_x\bar{\tau}_z\right)}_{\bar{h}_{1;0}} \\
&\quad - J\sum_{k=1}^{3} M_k \cdot \bar{\mathbb{1}}_{N_xN_y} \otimes \bar{\sigma}_k + \underbrace{\bar{D}_{x;N_x,1} \otimes (t\bar{\mathbb{1}}_4 + \mathrm{i}\tilde{\alpha}\bar{\sigma}_y)\bar{\tau}_z}_{\bar{h}_{1;x}}\,. \tag{237}
\end{aligned}
$$

We can now diagonalize this matrix separately for different values of k_y. Technically, we could build a full block diagonal matrix of size $D_1N_{k_y} \times D_1N_{k_y}$, where N_{k_y} is the desired number of points in the sampled k_y range, but this is not feasible. As it turned out, the necessary number of points in k_y is usually much larger than the needed resolution in y-direction for the two-dimensional case. Thus, a separate calculation is both simpler to parallelize and also better regarding memory usage.

3.5.3 Implementation Considerations

There are several circumstances that make it necessary to use many points and a fine lattice. The feature we are looking for, MBSes, are highly localised, thus requiring a fine resolution. This is also enhanced by the fact, that the domain wall has to be as thin as possible to provide the one-dimensional channel. But, on the other hand, we require a large system to avoid overlaps between the MBSes and for the dynamical part also to have enough one-dimensional states to work with. For that reason, the lattice for the spacing a of the discretisation cannot be chosen too small, especially for the time-dependent calculations in

the next section. It is important to select a value of a smaller than the domain wall width w. If we select a bigger or in the order of magnitude of x_0, the domain wall is not really a smooth 2π domain wall, but rather a double Ising wall. Nevertheless, this is the limit in which we work for the most part to make the numerical analysis feasible, with the exception of Section 3.6.4. There we numerically evaluate the smoother limit of the domain wall shape.

3.6 Numerical Results

Equipped with the methods, we can now run the ED numerics for various sets of parameters of interest. Just like before, we divide this discussion into two parts. The first one discusses the bulk system, which is infinite in y-direction. From this viewpoint, we can examine gap closings and calculate the topological invariant. But, as the system has no edge in the relevant direction, we cannot examine the MBS directly or any boundary effect. Thus, we additionally solve for the eigensystem of the finite Hamiltonian.

3.6.1 Bulk System

The bulk system, meaning the extent in y is infinite and there is no edge, is obtained from Equation (131) using a plane wave ansatz

$$\psi(\boldsymbol{r}) = \exp(\mathrm{i}k_y y)\varphi(x) \tag{238}$$

$$\hat{H}_{\mathrm{bulk}}(k_y) = \left(\frac{k_y^2 - \partial_x^2}{2m} - \mu\right)\bar{\tau}_z + \Delta\bar{\tau}_x - J\boldsymbol{M}(x)\cdot\bar{\boldsymbol{\sigma}} + B\bar{\sigma}_y$$
$$+ \alpha(\mathrm{i}\partial_x\bar{\sigma}_y + k_y\bar{\sigma}_x)\bar{\tau}_z , \tag{239}$$

which is essentially the same as Equation (184), except that we now specify the texture explicitly, which is

$$\boldsymbol{M}(x) = M_0 \begin{pmatrix} \sin(\theta(x)) \\ \cos(\theta(x)) \\ 0 \end{pmatrix} \tag{132}$$

$$\theta(x) = 2\arctan\left(\frac{\sinh\left(\frac{x}{x_0}\right)}{\sinh\left(\frac{w}{x_0}\right)}\right) - \pi\,. \tag{133}$$

This can be considered a one-dimensional Hamiltonian with k_y as a parameter. As we discussed in Section 3.3.7, the topology can be analysed using a Pfaffian invariant

$$\nu = \operatorname{sign}\left(\operatorname{Pf}\left(\hat{H}_{1,\mathrm{bulk}}(0)\right)\right)\left(\lim_{k_y \to \infty} \operatorname{sign}\left(\operatorname{Pf}\left(\hat{H}_{1,\mathrm{bulk}}(k_y)\right)\right)\right) \tag{185}$$

$$\hat{H}_{1,\mathrm{bulk}} \equiv \bar{U}\hat{H}_{\mathrm{bulk}}(0)\bar{U}^\dagger \tag{186}$$

$$\bar{U} \equiv \frac{1}{2}\begin{pmatrix} 1 & 0 & 0 & -1 \\ 0 & 1 & 1 & 0 \\ i & 0 & 0 & i \\ 0 & i & -i & 0 \end{pmatrix}. \tag{187}$$

Therefore, for MBSes to exist, the system needs to be gapped and have a suitable invariant. As for the gap only the pair of states closest to zero matters, it is sufficient to examine the lowest positive energy $\varepsilon_0(k_y)$. From the invariant in Equation (185) we know that only $k_y = 0$ and $k_y = \pm\infty$ are important for the decision whether we have topology or not. The behaviour at infinity is independent of all parameters except the mass m, which is always positive anyway. This is evident from the asymptotic behaviour

$$\hat{H}_{\mathrm{bulk}}(k_y) = \frac{k_y^2}{2m}\bar{\tau}_z + \mathcal{O}(k_y)\,. \tag{243}$$

Consequently, gap closings for topological transitions can only happen at $k_y = 0$. Note, that this does not mean that the rest of k_y-space is completely irrelevant as it still has an effect on the shape of the MBSes. Away from the gap closing, the minimal gap is not necessarily at zero any more. And as the gap is the main contributor to the localisation of the MBSes, this is a relevant quantity.
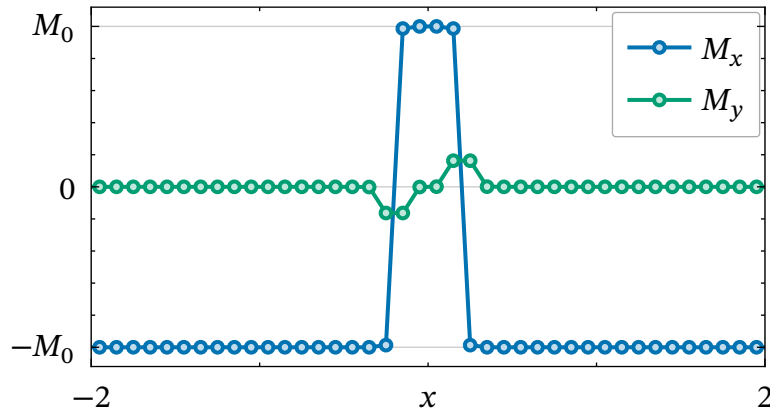
Figure 19: Magnetization profile for $w = 0.2$ and $x_0 = 0.02$ with points visualising the discretisation. The plot is zoomed-in to the range around the center of the wall.

Numerically, we can calculate both the spectrum and the invariant for various sets of parameters. But, as the system has many parameters, it is not possible to numerically cover the full space. We shortly go through all of them to give an overview of which part of the parameter space we discuss and which we do not. There are many parameters, so we select the topologically most crucial ones, which are the magnitude of the fields B and $J\boldsymbol{M}(\boldsymbol{r})$. As we can fix two scales (see Chapter A), we express all energies in terms of the superconducting gap and fix the unitless mass to unity resulting in $\Delta = m = 1$. We also restrict ourselves to $\mu = 0$ for simplicity for the most part, as this is common in the literature. But we comment in Section 3.7 on other values. For now, also the domain wall profile is fixed at $w = 0.2$ and $x_0 = 0.02$, but in Section 3.6.3, we will expand on this. The lattice parameter for the discretisation is $a = 0.1$. This is larger than the scale x_0, which leads to the domain wall basically turning into an unsmooth Ising wall (see Figure 19). For a good description of a 2π domain wall, a higher resolution is necessary, but difficult to achieve in the numerical calculations. We later in Section 3.6.4 discuss different limits and show that we find topology in all limits. This leaves only the SOC strength α. In general, we choose $\alpha = 0.3$, but this is also a useful point to discuss the difference between vanishing and finite SOC.

An essential ingredient of the effective one-dimensional channel is the bound state that provides it. In Figure 20, we show the bound states at two different field configurations — one below (**(a)**) and one above (**(b)**) the topological transition. At this point we do not know that this is indeed that case, but we state
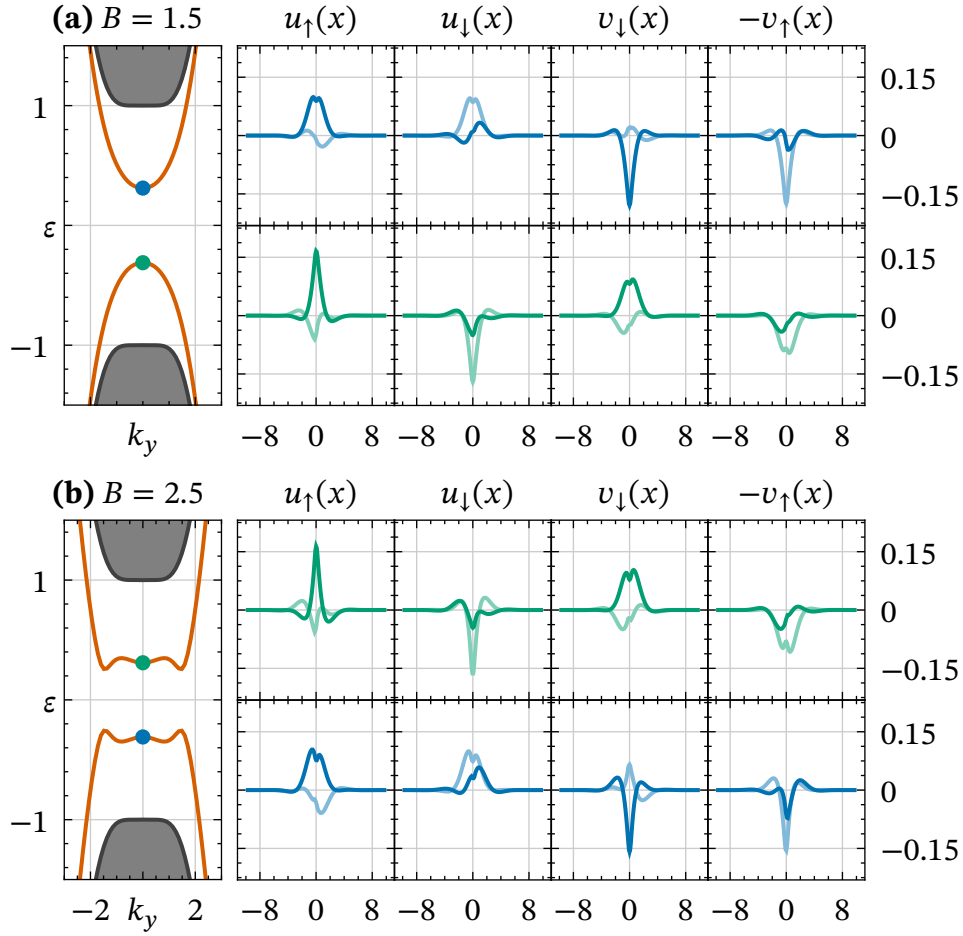
Figure 20: Bound states of the bulk system at zero wavevector and bulk spectra for $\Delta = 1$, $m = 1$, $\mu = 0$, $w = 0.2$, and $x_0 = 0.02$ and $B = JM_0$. The discretisation is perfomed with 201 points with a grid spacing of 0.1. The four Nambu components are shown separately with the real and imaginary part in different shading. The imaginary part is plotted in a lighter colour.

it for now and will later proof it with the calculation of the Pfaffian invariant. The values are chosen in a way to approximately match the energy of the bound states at $k_y = 0$ to make the structure more comparable. In the spectrum, we see that the bound state lives inside the superconducting gap, which is open between the two-dimensional continuum marked in gray. The shape of the in-gap band differs significantly between the two situations. While in the trivial region there is only one local minimum at $k_y = 0$, in the topological case there are two more minima at finite wavevector. As we will later observe, these are providing the global minima in most of the topological parameter space. When
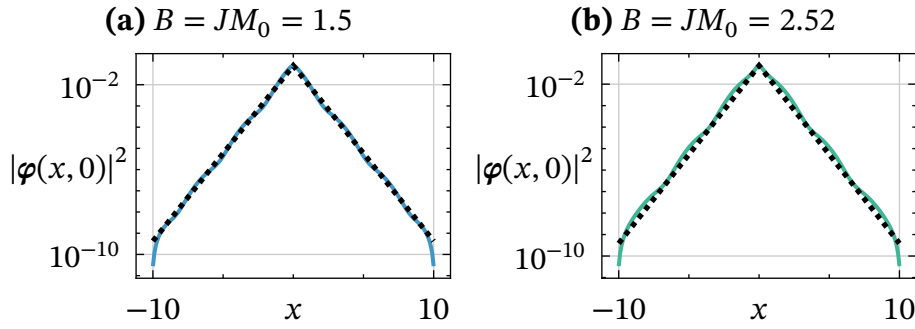
(a) $B = JM_0 = 1.5$ **(b)** $B = JM_0 = 2.52$

Figure 21: Comparison of the asymptotic beaviour of the bulk boundstates at $k_y = 0$ with the expression from Equation (207). The parameters are the same as in Figure 20 and are given by $\Delta = 1, m = 1, \mu = 0, w = 0.2,$ $x_0 = 0.02, a = 0.1,$ and $N = 201$ and $B = JM_0$.

examining the components at zero wavevector, the first observation to note is that due to the shown state pairs being particle hole partner, we see that we have $u_\sigma^*(x) = v_{\sigma(x)}$. In other words, each blue v_σ is the complex conjugate of the corresponding green u_σ and vice versa. Up to a phase, this has to be true by construction and is a resulting of the PHS in the BdG formalism (see Section 2.1.2). More interesting and relevant is the comparison between the different field configurations. There we observe, that the positive energy state in the trivial case (**(a)**) has a very similar shape than the negative energy state in the topological one (**(b)**). For illustration purposes we marked those pairs in the same colour. While not a conclusive proof, this highly suggests that those two configurations are indeed topologically different because the states seem to have swapped places, which requires a gap closing somewhere on the path.

We also examine the asymptotic behaviour of those states to check the analytic expression we obtained in Section 3.4

$$\lambda^{-1} = |\Im(k_{0,\infty})| = \sqrt{\frac{1}{2}\left(\sqrt{c_0^4 + c_1} - c_0^2\right)}$$

$$= m\alpha\sqrt{\frac{1}{2}\left(\sqrt{1 + \frac{4}{\alpha^4}\left(\Delta^2 - (\varepsilon_b \pm B_\infty)^2\right)} - 1\right)}. \qquad (207)$$

p. 74

We find a goood agreement with the numerical results. Consequently, this expression can be used to estimate the required length of the ribbon in y-direction.

This leads us to the results presented in Figure 22. Both for vanishing (**(a)** and **(b)**) and finite (**(c)** and **(d)**) SOC the value of the lowest positive energy $\varepsilon_0(k_y)$ is represented by the two most relevant values over a range of external field strengths B and exchange field JM_0. These two values are the energy at $k_y = 0$ (**(a)** and **(c)**) and the minimum (**(b)** and **(d)**) which is also the gap of the Hamiltonian. We compare both the value at $k_y = 0$ and the minimum of the band. Additionally, for the topological system with finite SOC, the topological invariant ν is presented. With red lines, the necessary conditions from Section 3.3.6 are included. What we observe is that inside this rectangular region, there is a line at which the gap closes, which is marked with a dashed line.

Starting from the value at zero wave vector (**(a)** and **(c)**), as this is the easiest to calculate. It as well illustrates the need to be careful and consider the other quantities as well, as the results of vanishing and finite SOC are basically indistinguishable. In both cases, there is a line at which the energy goes to zero, closing the gap. But, importantly and consistent with the previous topological discussion in Section 3.3 the gap does not reopen for the case without SOC, but instead is always closed somewhere in k_y-space, which we can see in **(b)**, where the gap of the infinite bulk system is plotted. This gap is given by the minimum of the lowest positive energy band. Thus, we can conclude that as we expect from the analytical results in Section 3.3, the Rashba coupling is responsible for reopening that gap. Another observation we can make is that the hard limits we got from Section 3.3.6 by requiring the region outside the domain wall to be trivial, indicated by dashed lines, are indeed providing limits to the topological phase with a gapless phase outside of them. This phase is also contained inside the boundary we got by neglecting rotational effects, shown with a dotted line, but this boundary is far away from the actual phase transition. The phase transition is also indicated by a change of the Pfaffian invariant ν shown in **(e)**, confirming the topological nature of the phase.

Summarizing this, we find a part of the phase diagram, in which we find topology in our quasi one-dimensional bulk system.
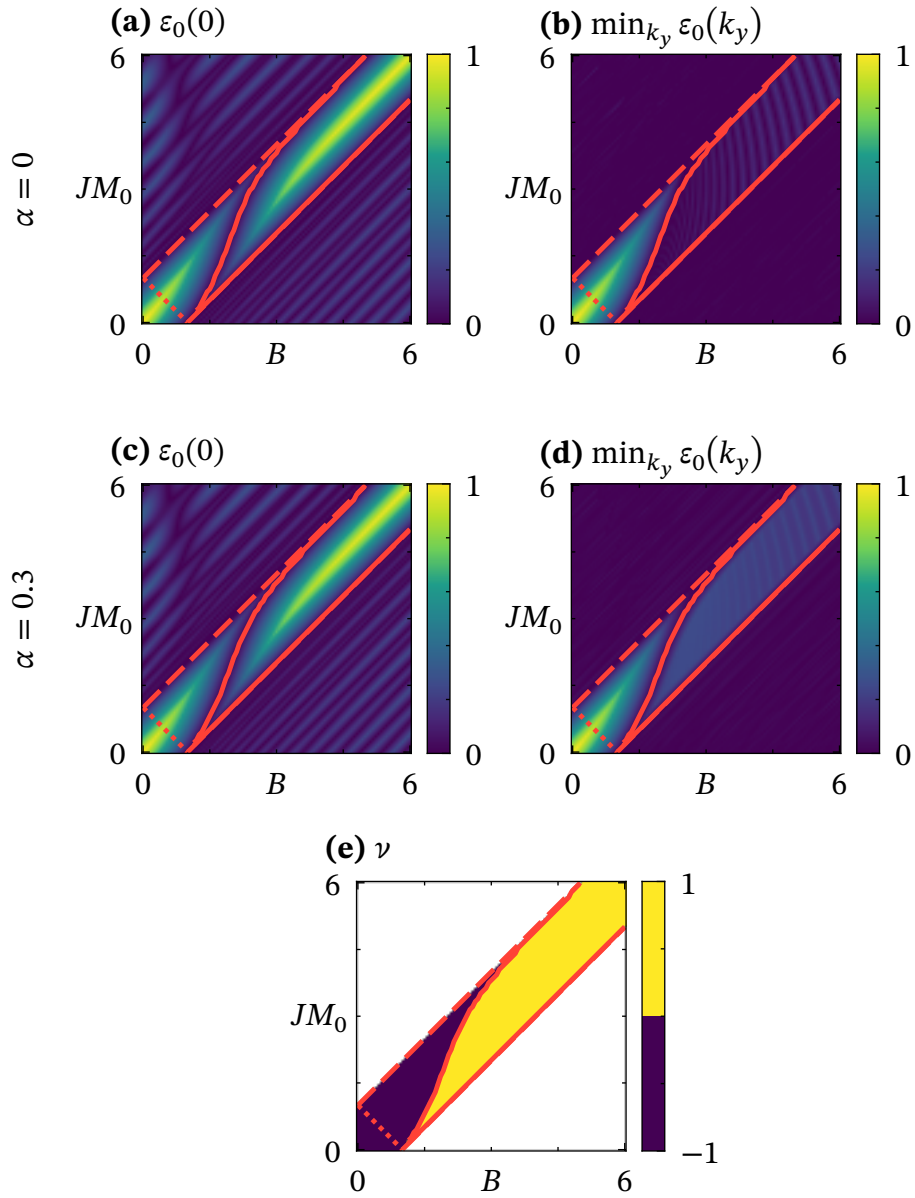
Figure 22: Phase diagram of the infinite (in y-direction) bulk system. The value of the lowest positive energy band bot at $k_y = 0$ (**(a)** and **(c)**) and at the minimum (**(b)** and **(d)**) are compared with (**(c)** and **(d)**) and without (**(a)** and **(b)**) SOC. For finite SOC, the invariant ν is shown as well (**(e)**). The calculation is performed for $\Delta = 1$, $m = 1$, $\mu = 0$, $w = 0.2$, and $x_0 = 0.02$. The discretisation is perfomed with 201 points with a grid spacing of 0.1.

3.6.2 Finite System

In the following, we additionally present results from a numerical diagonal-ization of the finite system. This opens up a path to look directly at the MBSes, which only appear once there is an edge in the y-direction and not in the bulk system. Additionally, we can discuss the effect of the superconducting environment, as the notion of an environment only makes sense once there is an edge that can border an environment. Another quantity we can use to get more indication about the character of the state is the Majorana polarisation[126], which builds on the fact that MBSes are their own PHS partner, up to a global phase, which yields

$$\hat{\mathcal{C}}\psi(\boldsymbol{r}) = e^{i\varphi}\psi(\boldsymbol{r}) \tag{244}$$

$$\Rightarrow \int d\boldsymbol{r}|\psi^{\dagger}(\boldsymbol{r})\hat{\mathcal{C}}\psi(\boldsymbol{r})| = 1. \tag{245}$$

Thus, if we have a MBS, this integral has to evaluate to unity. The complex integrand is also referred to as Majorana polarisation $P(\boldsymbol{r})$

$$P(\boldsymbol{r}) \equiv \psi^{\dagger}(\boldsymbol{r})\hat{\mathcal{C}}\psi(\boldsymbol{r}). \tag{246}$$

We can also express $P(\boldsymbol{r})$ in terms of the components of the wave function and obtain

$$P(\boldsymbol{r}) = 2(u_{\downarrow}^{*}(\boldsymbol{r})v_{\downarrow}^{*}(\boldsymbol{r}) - u_{\uparrow}^{*}(\boldsymbol{r})v_{\uparrow}^{*}(\boldsymbol{r})) \tag{247}$$

$$\psi(\boldsymbol{r}) \equiv \begin{pmatrix} u_{\uparrow}(\boldsymbol{r}) \\ u_{\downarrow}(\boldsymbol{r}) \\ v_{\downarrow}(\boldsymbol{r}) \\ -v_{\uparrow}(\boldsymbol{r}) \end{pmatrix}. \tag{248}$$

It is not a hard condition like the invariant, though, so it only gives a necessary, but not sufficient condition. Furthermore, due to numerical inaccuracies, the value can deviate from 1, even for a MBS.

We choose the same subset of parameters as for the bulk system before with the exception that we only consider finite $\alpha = 0.3$. Investigating the case of vanishing SOC does not give any more insight. The existence of an edge in the system facilitates the formation of the MBSes as edge states. Thus, it is useful to not only consider the lowest, but also the second-lowest positive energy here.
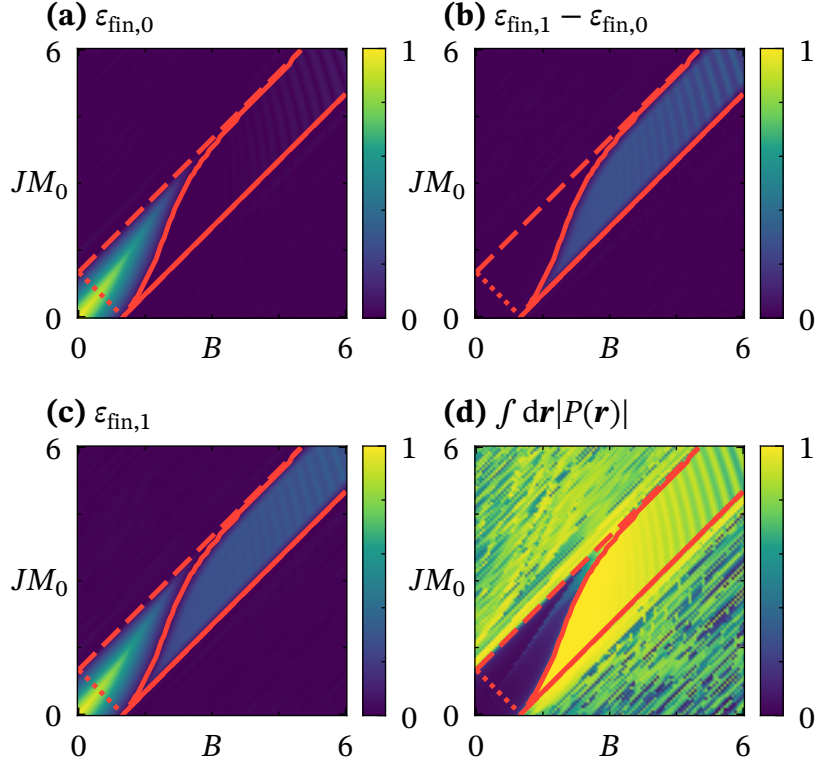
Figure 23: Phase diagram of the finite system. The value of the lowest ((**a**)) and second lowest ((**c**)) positive energy are shown in addition to the topological gap ((**b**)), which is just the difference of the two energies, and the integrated Majorana polarisation ((**d**)). The calculation is performed for $\Delta = 1$, $m = 1$, $\mu = 0$, $w = 0.2$, $x_0 = 0.02$, and $\alpha = 0.3$. The discretisation is perfomed with 201×301 points with a grid spacing of 0.1.

We expect in the topological regime to have one zero energy state with a gap, the topological gap Δ_{top}, to the next highest one.

In Figure 23, a similar phase diagram to the one for the bulk system in Figure 22 is presented. The lines mark the necessary conditions from Section 3.3.6: dashed for the strong condition forcing the background to be trivial and dotted for the weaker condition obtained from the centre of the domain wall. The topological region is outlined with a solid line. Plotted are the lowest ((**a**)) and second-lowest ((**c**)) energy, their difference ((**b**)) and the integrated Majorana polarisation ((**d**)). In the topological region, there is indeed an almost zero energy state with a minimum energy of around $\varepsilon_{\text{fin},0} \approx 1.17 \cdot 10^{-9} \Delta$. The gap to the next state reaches around $\Delta_{\text{top}} \approx 0.35 \Delta$ at the highest point and is thus many orders of magnitude higher than the energy of the MBS. Additionally, the

integrated polarisation also confirms the Majorana character. At higher fields, the integrated polarisation is not strictly one any more, which we attribute to finite-size and discretisation effects. Furthermore, in the gapless region outside the area from Section 3.3.6 it is non-vanishing as well. This is expected for the following reason. In this part, the whole sample is topological, which is why we have topological bands of one-dimensional states instead of a single pair of zero-dimensional states. Those cross zero energy, resulting in states around zero that have Majorana character. But as the band forms a continuum,[30] the numerical states are very nearby in energy, the lowest state is not forced to be at zero energy. Any deviation from zero energy or some overlap with other states causes a non-perfect integration to unity. Therefore, in general, the Majorana polarisation is only useful in addition to other checks, for example calculating the gap or the invariant.

It is also insightful to examine the states directly. In Figure 24, the two lowest positive energy states are visualized. The lowest state, the MBS, is well localised at the edge of the effective one dimensional channel provided by the domain wall. It is also about four orders of magnitude lower in energy than the next highest state, which is a bound state in the channel. The separation between those states is the topological gap $\Delta_{\text{top}} \approx 0.27\,\Delta$. The Majorana character of the state is also represented in the Majorana polarisation from Equation (246). For the MBS it numerically integrates to unity as expected for a Majorana state.

Therefore, we can conclude that the topology we found in the bulk system indeed establishes itself in the finite system in the form of zero-dimensional edge states with Majorana character.

3.6.3 Domain Wall Width

As a next step, we examine the influence of the domain wall shape. We stay for now in the limit of an Ising-like wall, which means that we have a rather coarse discretization and a very steep domain wall. The parameter we are investigating in this section is the width of the domain wall while keeping the ratio to the steepness constant at $x_0 = 10w$. To have the effectively one-dimensional channel, the domain wall needs to be thin compared to the length scales of the

---

[30]As the numerical simulation is discrete, the band is not a strict continuum, but rather a discrete collection of many states.
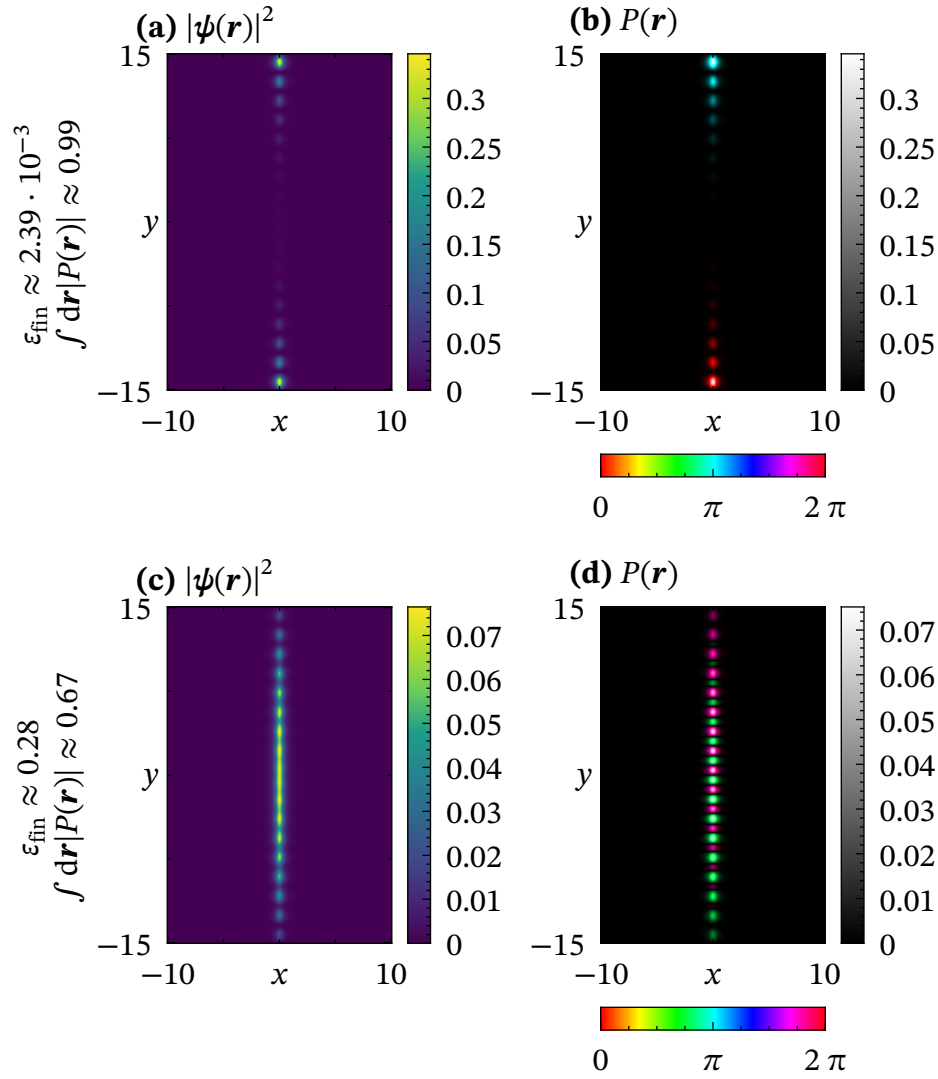
Figure 24: Profiles of the lowest positive two energy states for $\Delta = 1$, $m = 1$, $\mu = 0$, $w = 0.2$, $x_0 = 0.02$, $\alpha = 0.3$, $B = 3$, and $JM_0 = 3$. The discretisation is perfomed with 201×301 points with a grid spacing of 0.1. Plotted are the MBS (**(a)** and **(b)**) and the next highest in energy (**(c)** and **(d)**). For both of them, the local density of state (**(a)** and **(c)**) and the Majorana polarisation (**(b)** and **(d)**), for which the lightness represents the magnitude and the color the complex angle, are show. The Majorana polarisation is only determined up to a global constant.

problem. But this is not a hard limit, so we analyse in the follow how the system behaves when this breaks down. For this, we start by looking at the minimum of the bulk spectrum and the gap from the lowest to the second lowest state
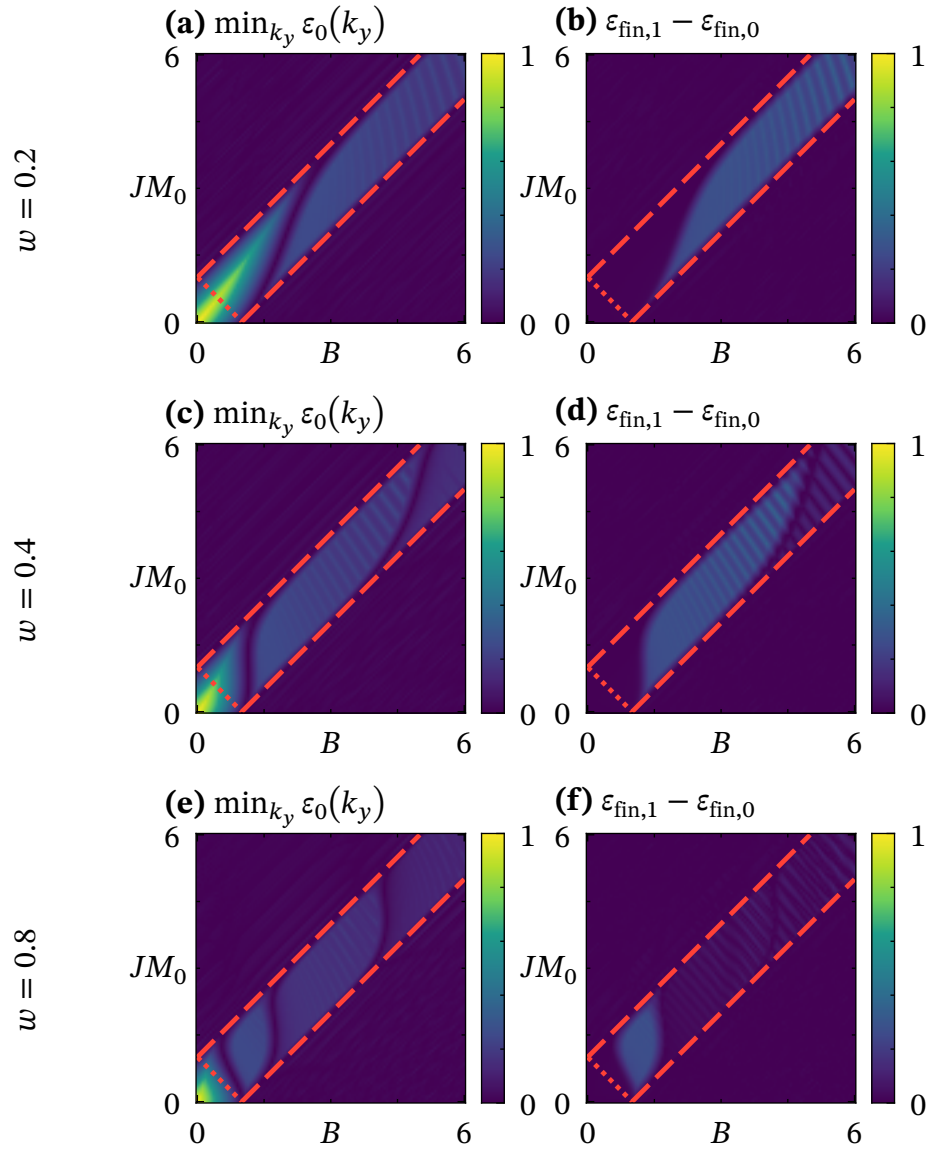
Figure 25: Minumum of bulk spectra (left column) and finite gap (right column) at different domain wall widths for $\alpha = 0.3, m = 1, \Delta = 1$, and $w = 10x_0$ with a lattice constant of $a = 0.1$. and a grid of size 201×301 and a grid of size 201.

in the finite system (see Figure 25). There are several interesting observations here. The first one is that both the upper and lower limit of the region with a signficant gap in the finite system move to lower fields with increasing domain
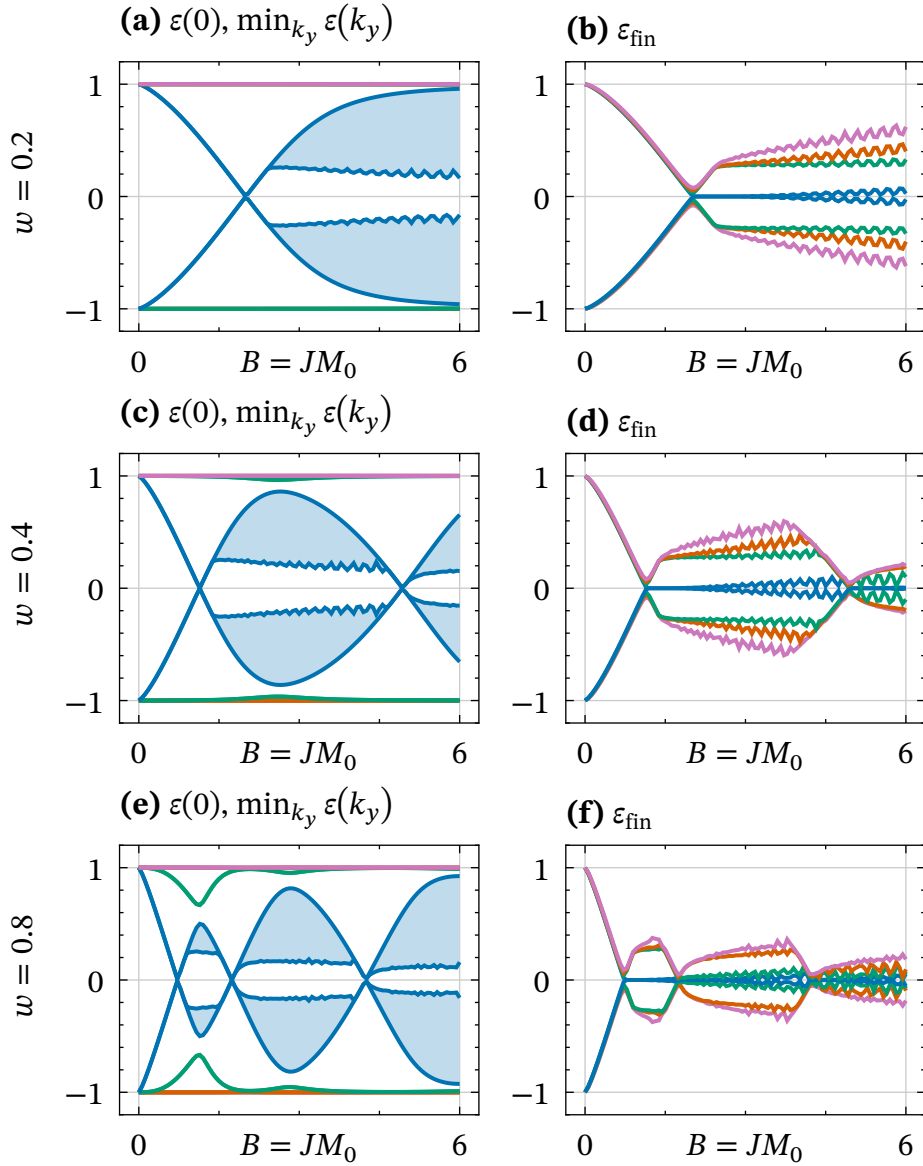
Figure 26: Lowest four pairs of states of the bulk ((a), (c) and (e)) and finite ((b), (d) and (f)) system for different domain wall widths and $B = JM_0$. The calculation is done for $\alpha = 0.3$, $\mu = 0$, $m = 1$, $w = 0.2$, $\Delta = 1.00$ with a lattice constant of $a = 0.1$. and a grid of size 201×301 for the finite and of size 201 for the bulk system. For the bulk system both the minimum and the value at $k_y = 0$ are plotted to visualize the continuum.

wall width with the upper limit doing this more rapidly. Therefore, with wider domain walls, we find topology at lower fields, but also in a much smaller range.

Another observation can be made at fields above this topological region. For wider domain walls there are additional regions appearing with a finite bulk gap, but basically no gap between the lowest two states. This indicates that there are more zero energy states appearing here. But as this is hard to see in two-dimensional plot, we make a cut along the $B = JM_0$ diagonal and examine the lowest eight states of the finite and the lowest eight bands in the bulk system. The results are plotted in Figure 26. We show both the bulk and finite spectra. For the bulk ((**a**), (**c**) and (**e**)), the energy range spanned between the value of the band at zero wavevector and the minimum of the band is shaded. This is presented for the lowest four pairs of bands. The lowest four pairs of eigenvalues of the finite system are plotted in (**b**), (**d**) and (**f**). At lower fields and thinner domain walls, we observe the same behaviour as we have seen before. At a critical field, the bulk gap closes and reopens again. Above this field, a zero energy state[31] forms that is separated by a topological gap to the next highest state. This gap is also given by the minimum of the lowest bulk band. A relevant difference between the domain wall widths is the value of the critical field. Thinner domain walls require a higher critical field. In the bulk model, also the first states of the two-dimensional continuum with energies outside the gap are visible.

But for wider domain wall and higher fields, new phases appear. There is a second and in the case of a domain wall width of $h = 0.8$ even a third critical field. Similar to the first critical field, those as well shift to lower values for wider domain walls. At each of these field values, the bulk gap closes and reopens and anouther pair of in-gap states close to zero appear. This suggests, that the domain wall might be wide enough to provide more than one effectively one-dimensional channel. We cannot provide more insight into the possible topology of these states.

To summarize the results of this discussion, it is in general beneficial to have a thin wall to maximize the topological region. At the same time, this has to be balanced with the fact that thinner walls also require higher fields.

---

[31]Due to numerical limitations, significant osciallatory behaviour is visible in these results. This is a result of the limited system size and discretization. The larger the system, the lower these oszillations.

3.6.4 Resolution and Domain Wall Shape

After only considering sharp Ising-like domain wall (see Figure 19), we need to confirm that the actual 2π domain walls promised in the title share the features we found so far. For this, we increase the resolution to be in the limit, where the lattice constant a is much smaller than both the domain wall width w and the rotation scale x_0 (see Figure 27**(b)**). Due to the higher number of points, not all calculations are feasible any more. Thus, we only look at the value of the lowest band of the bulk model. In Figure 27 **(a)**, the same domain wall with width $w = 0.4$ and steepness $x_0 = 0.04$ we discussed in the previous section (see Figure 25 **(c)** and **(d)**), but now with a much smaller lattice parameter of $a = 0.01$ and a smaller system size to make the calculation possible. Comparing with the previous result of a coarser grid (see Figure 19), the gap closes at the same points. This shows that the rough discretisation we chose before and which led to the domain having Ising character in the simulation does not change the topology. The results are therefore also applicable to the smooth domain walls mentioned in the title of this work.

At this point it is also interesting to examine the influence of the steepness of the domain wall x_0. As a reminder, a small value of x_0 compared to the width w results in a box-like shape and a higher one in a sharper and smoother one (see Figure 27 **(b)**, **(d)** and **(f)**). We examine two additional cases for x_0 that are different from the box-like case we discussed before by increasing x_0 from 0.04 to 0.2 and 0.4. This results in a visible change to gap closing lines. The limits of this region are decreased from the top while the lower limit stays the same. Therefore, a smoother domain wall results in a smaller region of topology.

Thus, we found that our results are generisable to a smaller lattice constant and therefore also apply to 2π domain walls. Additionally, the results indicate that not just the width of the domain wall, but also its shape influences the topological phase region with the impact mostly being restricted to the upper field limit.

3.7 Superconducting Environment

Something that is not accessible purely from the bulk analysis is the effect of an environment. While there are in general many different boundary conditions
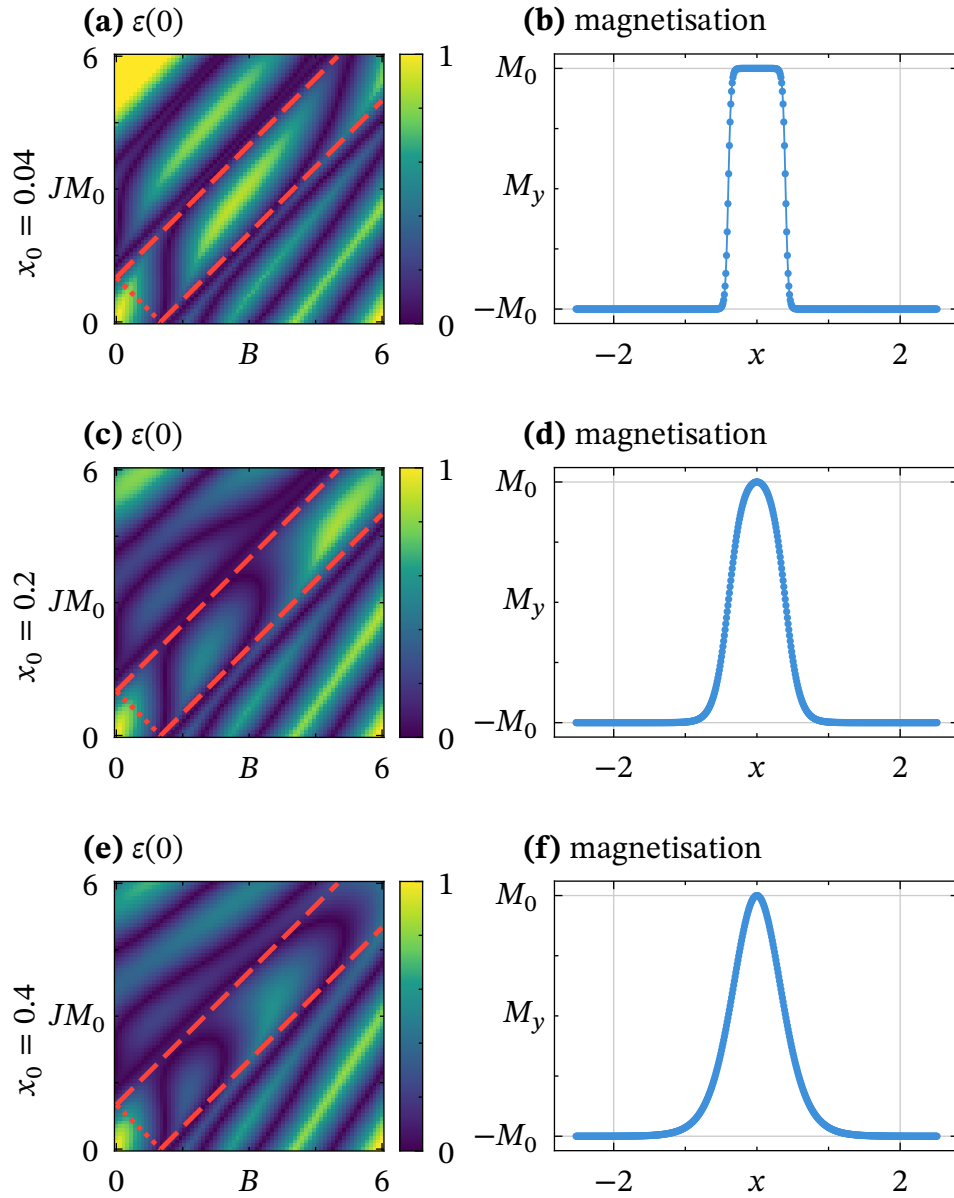
Figure 27: Lowest positive energy band of the bulk system at $k_y = 0$ (**(a)**, **(c)** and **(e)**) and y-component of the magnetisation profile (**(b)**, **(d)** and **(f)**) for different domain wall shapes. For the magnetisation profile, the points represent the lattice sites at which it is samples for the numerical calculation. The calculation is performed for $\Delta = 1$, $m = 1$, $\mu = 0$, $= 0.4$, and $\alpha = 0.3$. The discretisation is perfomed with 505 points with a spacing of 0.01.

that could be investigated, we focus on a superconducting environment because this is a case that might happen in experiments. With *superconducting environ-*
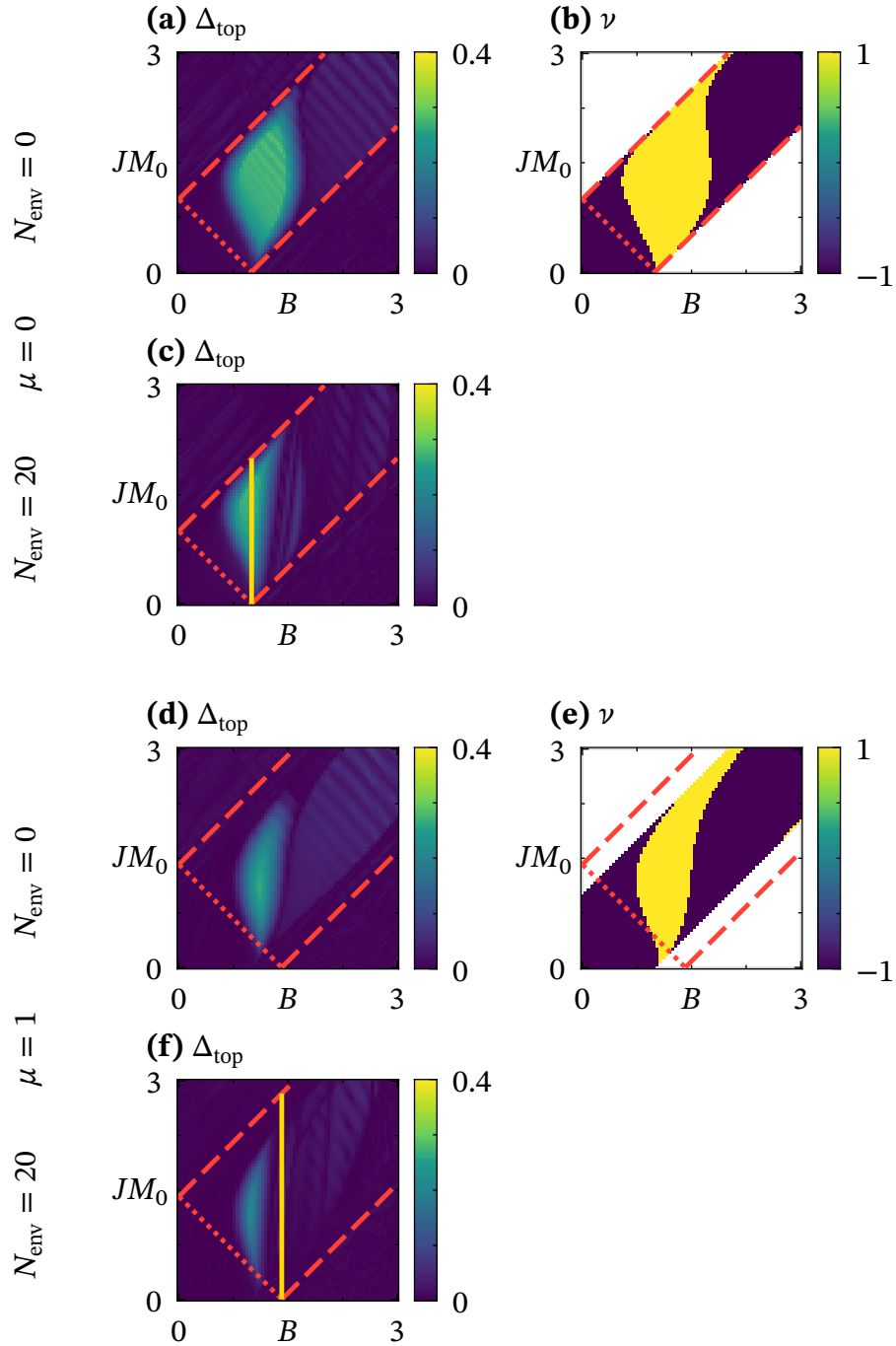
Figure 28: Topological gap (**(a)**, **(c)**, **(d)** and **(f)**) and bulk invariant (**(b)** and **(e)**) for different chemical potentials and environments. The calculation is performed for $\Delta = 1$, $m = 1$, $w = 0.8$, $x_0 = 0.08$, and $\alpha = 0.3$. The discretisation is perfomed with 201×301 points for the finite and 201 points for the bulk invariant, both with a grid spacing of 0.1.

ment we mean that the magnetic layer is a thinner strip than the superconductor (see Figure 17). We touched on this subject in Section 3.3.6, where we concluded that the effect of a superconducting environment is an upper limit on the external field. This is caused by the fact that the environment becomes topological for high external fields, causing the effective wire to not have a boundary with a trivial outside. With the numerical simulations, we have access to the spectrum of the finite system.

As the critical field also scales with the chemical potential and the critical field is relevant for the effect of the environment, this is also a useful point to examine a non-zero chemical potential. In Figure 28, the resulting topological gaps and invariants are shown. As the invariant is calculated on the bulk system, the notion of an environment is not existent there. We also use a wider domain wall as we found this to be helpful and making the differences easier to spot, because as this pushed the lower boundary of the topological region to lower fields as we discussed before.

Let us start with the chemical potential. From the topological discussion we know that the critical field is $B_c = \sqrt{\Delta^2 + \mu^2}$ and therefore rises with increasing chemical potential. This affects the conditions from Section 3.3.6 and therefore the reference lines in Figure 28 shift when changing the chemical potential μ. We also included a yellow line right of which the enviroment becomes topological. When comparing the cases without an environment, but with different chemical potential μ — so Figure 28 **(a)** and **(b)** with **(d)** and **(e)** — we see that the situation is more complicated than the simple analysis in Section 3.3.6 suggests. The wider range between the dashed lines due to a higher critical field does not broaden the topological area, which is still limited to the same extent. This suggests that the existence of a bound state in the bulk system is not changed by the different chemical potential. But the upper limits of the topological regions are restricted on the side of higher fields, resulting in a smaller topological region for the higher chemical potential. The origin of this is not clear yet and needs further investigation.

The existence of a superconducting environment also has a visible effect on the topology. We see that the regime in which the topological gap ((**c**) and (**f**)) is finite is smaller when the enviroment is added. This reduction happens at larger external fields, which is consistent with the results from Section 3.3.6 and is explained be the environment becoming topological and hosting in-gap states itself. The effect of the environment is more evident when looking directly at the states. When we take a point at which the system with no environment
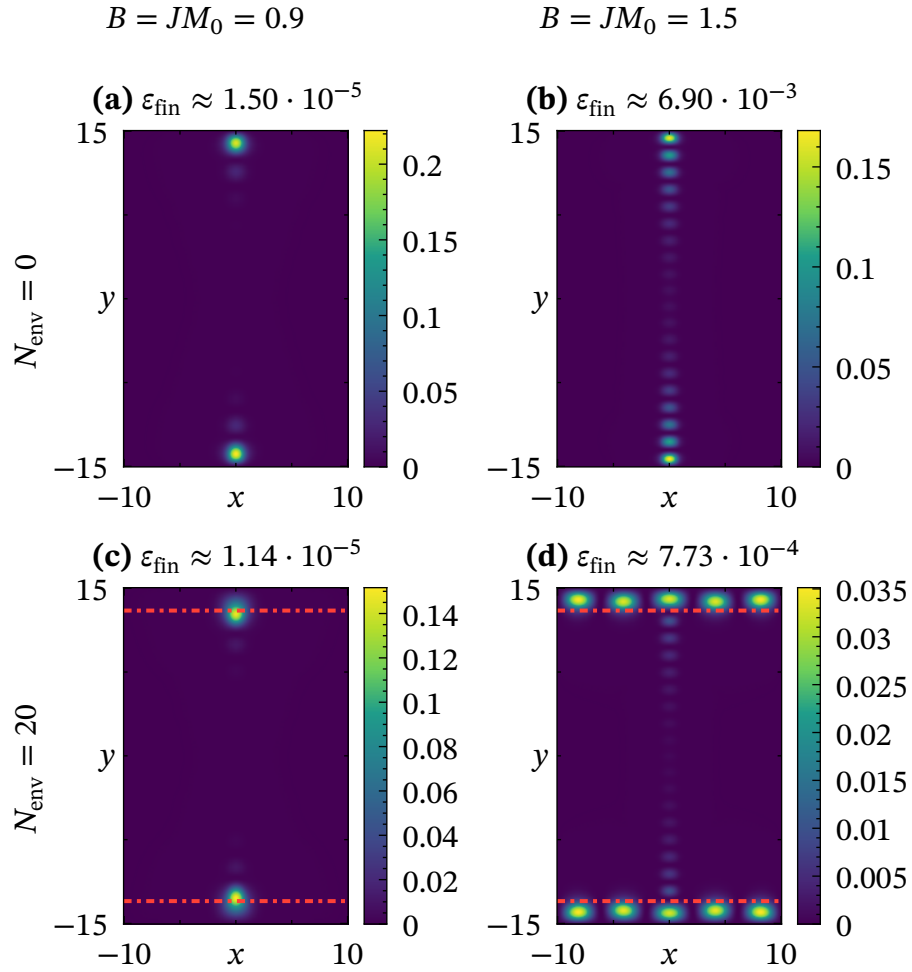
Figure 29: Profiles of the lowest states with ((**c**) and (**d**)) and without ((**a**) and (**b**)) a superconducting environment for $\Delta = 1$, $m = 1$, $\mu = 0$, $w = 0.8$, $x_0 = 0.08$, and $\alpha = 0.3$ and two different field configurations. The discretisation is perfomed with 201×301 points with a grid spacing of 0.1. The superconducting environment is marked with a red line.

shows a topological gap, but one with one does not, the difference becomes very apparent. In Figure 29, we compare the lowest eigenstate of the finite system with different environments at two different field configurations with $B = JM_0$. At the lower field, we find MBSes in both environment configurations, because the environment is topologically trivial here. This changes at the higher field,

where the environment becomes topological. Although the field configuration is still suitable for MBSes as we see from the state in **(b)**, we do not see one in **(d)** with the environment, which is topological now. This causes the effective one-dimensional wire to not border a trivial regime[32], but a topological one. The edge states in the environment couples to the zero energy state in the wire, thus breaking the localization.

Consequently, we confirmed our findings in Section 3.3.6 and have shown that a superconducting environment can be detrimental for MBSes in the case of high enough external fields. The chemical potential also restricts the topological phase, but the results nevertheless suggest, that topology can also be found with non-zero chemical potential, generalizing the previous results to a more realistic case.

---

[32]If there is no environment, the vacuum is also a trivial state.

Dynamical Features

<div style="text-align: right">4</div>

In all the previous sections, everything was static. For computations with the MBSes, dynamics are needed as the goal is to achieve braiding. As the braiding process involves moving two Majoranas around each other, movable Majoranas are a necessity. Thus, dynamical manipulations being possible is one of the major motivations to pursue an approach with magnetic 2π domain walls instead of elongated skyrmions or magnetic adatom chains. The main leverage for dynamics here are movements of the domain wall that then might drag the MBS with it. We aim to estimate how and how fast the MBS can be moved without being destroyed. To gain a more profound understanding, we present different approaches that tackle the problem from different angles. We start by discussing the general model and its time dependence. Afterwards, the case of a suddenly moving domain wall is explored before continuing with a discussion about the application of Fermi's golden rule to the system. We conclude with a numerical simulation, that provides direct access to arbitrary movement profiles and sample shapes.

4.1 Model

We consider the same system as before, but now with a moving domain wall. Thus, the Hamiltonian of the dynamical system reads

$$\hat{H}(t) = \left(-\frac{\hat{\mathbf{\nabla}}^2}{2m} - \mu\right)\bar{\tau}_z + \Delta\bar{\tau}_x + B\bar{\sigma}_y + \mathrm{i}\alpha(\hat{\mathbf{\nabla}} \times \bar{\sigma})\bar{\tau}_z \tag{249}$$

$$-J\mathbf{M}(x - p(t)) \cdot \bar{\sigma} \tag{250}$$

with the same magnetisation profile as before
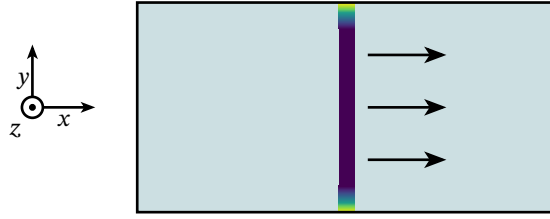
Figure 30: Sketch of the dynamical setup. The domain wall moves along the x-direction. The intent of this procedure is to drag the MBS along with the wall.

$$\boldsymbol{M}(x) = M_0 \begin{pmatrix} \sin(\theta(x)) \\ \cos(\theta(x)) \\ 0 \end{pmatrix} \tag{132}$$

$$\theta(x) = 2\arctan\left(\frac{\sinh\left(\frac{x}{x_0}\right)}{\sinh\left(\frac{w}{x_0}\right)}\right) - \pi. \tag{133}$$

<div align="right">p. 46</div>

The basic idea is that the one-dimensional channel which hosts the MBSes is provided by the magnetisation profile is moved along the x-direction (see Figure 30). Hence, if we move the magnetic domain wall, which is doable by applying spin currents in the magnetic layer[39–43], the MBSes might move with it as well.

4.2 Comoving Frame

As, currently, the time dependence is located in the complicated magnetisation profile, it is beneficial to perform a transformation to simplify the following treatment. The coordinate system is shifted such that the origin ies at the current position of the domain wall. The time-dependent Schrödinger equation of the problem reads with the Hamiltonian from Equation (249)

$$i\partial_t \boldsymbol{\psi}(\boldsymbol{r}, t) = \hat{\bar{H}}(t)\boldsymbol{\psi}(\boldsymbol{r}, t). \tag{252}$$

We now apply a shift in x-direction (perpendicular to the domain wall, see Figure 30) by $-p(t)$ with the unitary translation operator $\hat{T}_p = \mathrm{e}^{\mathrm{i}p(t)\partial_x \bar{\tau}_z}$. Thus, we have

$$i\hat{T}_p\partial_t\boldsymbol{\psi}(\boldsymbol{r},t) = \hat{T}_p\hat{H}(t)\hat{T}_p^\dagger\hat{T}_p\boldsymbol{\psi}(\boldsymbol{r},t) \tag{253}$$

$$i\big(\partial_t + [\hat{T}_p,\partial_t]\hat{T}_p^\dagger\big)\hat{T}_p\boldsymbol{\psi}(\boldsymbol{r},t) = \hat{T}_p\hat{H}(t)\hat{T}_p^\dagger\hat{T}_p\boldsymbol{\psi}(\boldsymbol{r},t) \tag{254}$$

$$i\partial_t\boldsymbol{\varphi}(\boldsymbol{r},t) = \hat{\mathcal{H}}(t)\boldsymbol{\varphi}(\boldsymbol{r},t)\,, \tag{255}$$

where we introduced the new operator and states

$$\hat{\mathcal{H}}(t) \equiv \hat{T}_p\hat{H}(t)\hat{T}_p^\dagger + \hat{H}_1(t) \tag{256}$$

$$\hat{H}_1(t) \equiv -i[\hat{T}_p,\partial_t]\hat{T}_p^\dagger \tag{257}$$

$$\boldsymbol{\varphi}(\boldsymbol{r},t) \equiv \hat{T}_p\boldsymbol{\psi}(\boldsymbol{r},t) = \boldsymbol{\psi}(\boldsymbol{r} - p(t)\hat{\boldsymbol{e}}_x,t)\,. \tag{258}$$

This means that the transformation is no unitary change of basis, but also adds another contribution. We now evaluate this contribution in our specific Nambu base. This yields

$$\begin{aligned}
\hat{H}_1(t) &= -i[\hat{T}_p,\partial_t]\hat{T}_p^\dagger = -i(\hat{T}_p\partial_t - \partial_t\hat{T}_p)\hat{T}_p^\dagger \\
&= -i(\hat{T}_p\partial_t - (\partial_t\hat{T}_p) - \hat{T}_p\partial_t)\hat{T}_p^\dagger \\
&= i(\partial_t\hat{T}_p)\hat{T}_p^\dagger = i\dot{p}_x(t)\partial_x\bar{\tau}_z\,.
\end{aligned} \tag{259}$$

Therefore, the Hamiltonian in the comoving frame reads

$$\begin{aligned}
\hat{\mathcal{H}}(t) &= \hat{T}_p\hat{H}(t)\hat{T}_p^\dagger + i\dot{p}_x(t)\partial_x\bar{\tau}_z \\
&= \Big(-\frac{\boldsymbol{\nabla}^2}{2m} - \mu\Big)\bar{\tau}_z + \Delta\bar{\tau}_x \\
&\quad -J\boldsymbol{M}(\boldsymbol{r})\cdot\bar{\boldsymbol{\sigma}} + B\bar{\sigma}_y \\
&\quad +i\alpha\boldsymbol{e}_z\cdot(\boldsymbol{\nabla}\times\boldsymbol{\sigma})\bar{\tau}_z + i\dot{p}_x(t)\partial_x\bar{\tau}_z\,,
\end{aligned} \tag{260}$$

where the additional term $\hat{H}_1(t)$ is the only explicitly time-dependent part. The new term takes the form of a classical shift in the kinetic energy. This is the form of the Hamilonian that we are going to use in the rest of this section.

4.3 Constant Velocity

On this level, we apply an adiabatic approximation (see Section 2.4.1). The relevant quantities are

1. the *instantaneous* states $\boldsymbol{\xi}_n(\boldsymbol{r},t)$
2. the *instantaneous* energies $E_n(t)$.

The discarded terms are proportional to matrix elements of the time-derivative of the Hamiltonian $\dot{\hat{H}}_t(t)$, which is proportional to the acceleration of the wall $\ddot{p}_x(t)$. Thus, if the domain wall moves with constant velocity, the adiabatic approximation is, in fact, exact. For this section, we examine this case and set

$$\dot{p}_x(t) = v \,. \tag{261}$$

One essential feature of the adiabatic approximation is that, once we are in an instantaneous eigenstate, the system will always stay in it. In other words, if there exists a bound state with a constant velocity, it is completely stable and will not decay. On the other hand, if there was no bound state in the moving system, there would be no possibility to move a MBS, because it depends on the existence of the channel provided by the bound state. Therefore, as a preparation for the following analysis, we check the moving bulk system for the existence of a bound state. For this, we add the dynamic term from Equation (260) and numerically calculate eigenstates. Those are the instantaneous eigenstates discussed above. To allow for better comparison, we choose the same parameters as in Figure 20 for the analysis. The result is presented in Figure 31. The spectrum away from $k_y = 0$ is significantly transformed compared to the static case in Figure 20, the states are nevertheless localized. The other visual features are the same as in the static case, and the states look like they have shifted places, indicating that the topological protection stays intact.

In consequence, we see that the added energy term from constant movement does not inhibit the formation of a bound state. Therefore, a bound states exists that moves in sync with the domain wall and does not scatter into other states in the adiabatic limit.

4.4 Sudden Movements

In reality, we cannot have an always moving wall, but instead have to start from a static system and then transition to the moving one. Thus, the question arises whether static bound state evolves into the comoving one or scatters into other states. In [127], the probability that a system that starts in a bound state on a generic well avoids scattering into other states was evaluated. We apply the concept introduced there to the moving 2π domain wall in the bulk model and investigate the probability. The suddenly moving wall is described by the position
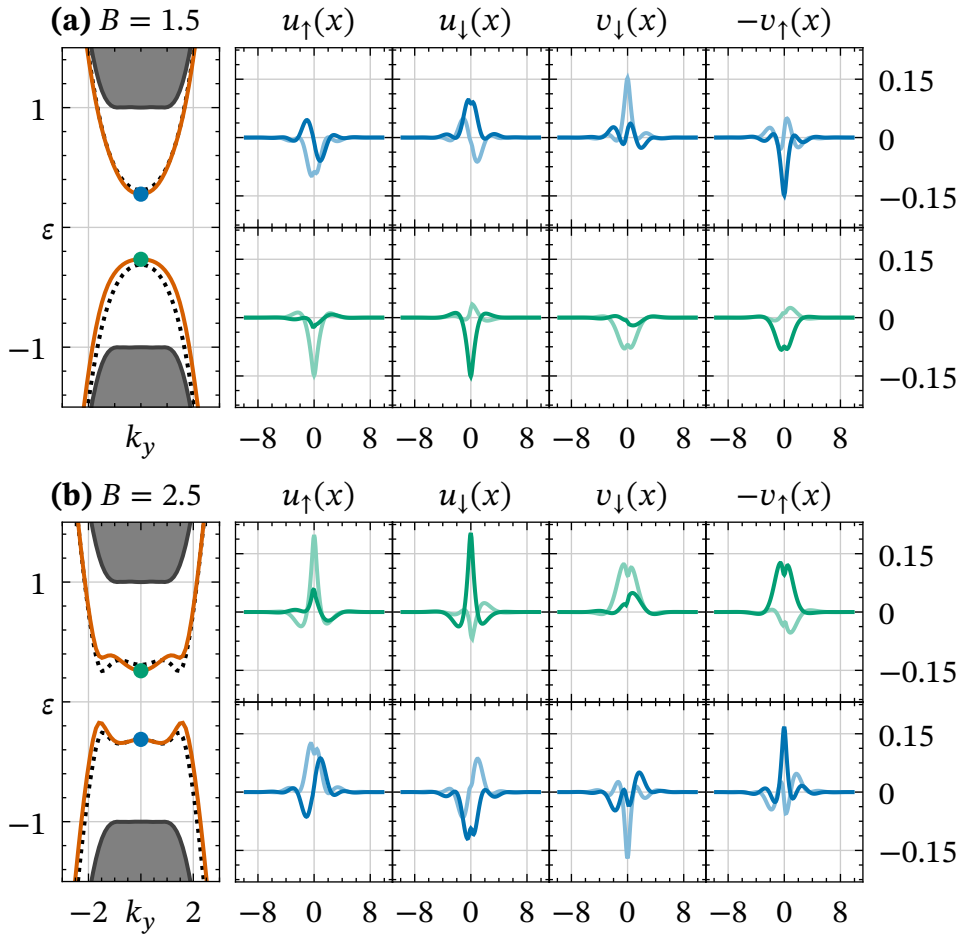
Figure 31: Bound states (right) and spectrum (left) on a moving domain wall for $k_y = 0$ for $\Delta = 1$, $m = 1$, $\mu = 0$, $w = 0.2$, $x_0 = 0.02$, and $\dot{p}_x = 0.25$. The discretisation is perfomed with 201 points with a grid spacing of 0.1. The four Nambu components are shown separately with the real and imaginary part in different shading. The imaginary part is plotted in a lighter colour. The spectrum is shown with the static one marked with dotted line as a comparison and the bulk continuum shaded in gray. The bound state inside the superconducting gap is drawn in orange.

$$p_x(t) = \begin{cases} v_0 t & \text{if } t > 0 \\ 0 & \text{otherwise,} \end{cases} \tag{262}$$

We put the system at $t = 0$ into the static bound state $\varphi(\boldsymbol{r})$. The bound state of the moving potential $\psi(\boldsymbol{r}, t)$ is related to the static one $\varphi(\boldsymbol{r})$ by

$$\psi(\boldsymbol{r}, t) = \exp\left(\mathrm{i}mvx - \mathrm{i}\frac{mv^2}{2}t - \mathrm{i}Et\right)\varphi(\boldsymbol{r} - \boldsymbol{p}(t)). \tag{263}$$

As a next step, we calculate the probability that the system stays in the same state it was at $t = 0$. From the adiabatic approximation, which is exact for constant velocity, we know, that once the system is in the moving bound state, it will not decay. Thus, it is sufficient to examine the point $t = 0$. There, there possibility for the system to transition from the static state $\varphi(\boldsymbol{r})$ at $t < 0$ to the state $\psi(\boldsymbol{r}, t)$, which are eigenstates at $t > 0$, is given by their overlap. This overlap evaluates to

$$P_{00} = \int \mathrm{d}\boldsymbol{r}\, \psi(\boldsymbol{r}, 0)^{\dagger}\varphi(\boldsymbol{r}) = \int \mathrm{d}\boldsymbol{r}\, \mathrm{e}^{-\mathrm{i}mvx}|\varphi(\boldsymbol{r})|^2. \tag{264}$$

As there is no analytic expression for the bound states, we calculate this probability numerically. This involves calculating the lowest eigenstate of the static bulk system and plugging it as $\varphi(\boldsymbol{r})$ into Equation (264). The results of this are presented in Figure 32. We also estimate the width of the distribution by fitting a gaussian.

Note that these are the probabilities for the respectively lowest state, which, depending on the region, might not be an MBS. The probability strictly monotonically decreases with increasing velocity and starts by definition at unity for zero velocity. This confirms the intuition that higher velocities and thus more energy put into the system can cause the bound state to be left behind. There is no critical velocity as the probability never crosses zero. But with increasing field, the distribution broadens, resulting in a more stable configuration. Another thing to note is that the distribution is smooth with no characteristic features appearing at specific velocites.

4.5 Fermi's Golden Rule

To make the next step of generalisation, we pertubatively treat the case of non-constant velocity and use Fermi's golden rule[128] to calculate transition probabilities. We take an oscillating velocity

$$\dot{p}_x(t) = v_0 \sin(\omega t), \tag{265}$$

resulting in the time-dependent potential

(a) Probability

(b) Distribution width
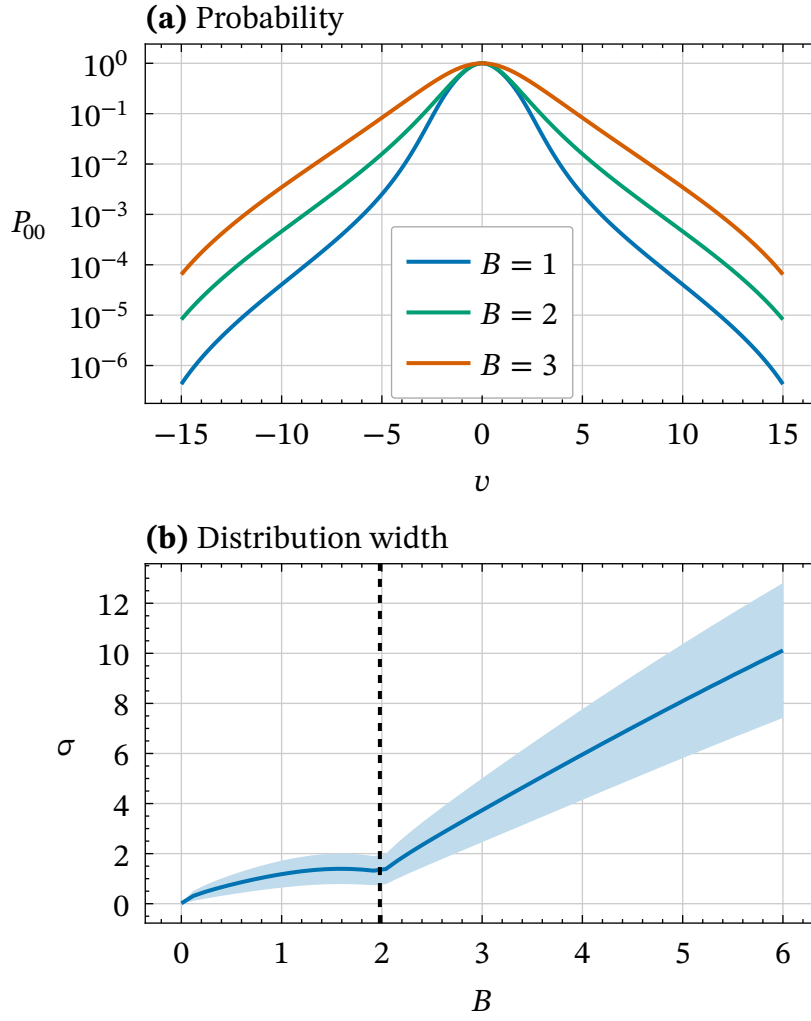
Figure 32: Dependence of the probability to stay in the bound state at the point of a sudden jump in velocity on the velocity **(a)** and width of the distribution for different fields **(b)** for $\Delta = 1$, $\alpha = 0.3$, $m = 1$, $w = 0.2$, $x_0 = 0.02$ and different magnetic field configurations. The topological transition is marked with a dashed line and obtained by looking for a sign change in the Pfaffian invariant at $t < 0$. The width is obtained via fitting a gaussian and the fit error is visualised by shading an area of one standard deviation.

$$\hat{\bar{H}}_1(t) = \underbrace{i v_0 \partial_x \bar{\tau}_z}_{\hat{\bar{V}}} \cos(\omega t).$$
(266)

The transition rate from the lowest positive energy state $\varphi(\boldsymbol{r})$ to another state $\psi(\boldsymbol{r})$ with energy E is given by

$$\Gamma_{\varphi \to \psi}(v_0, \omega) = 2\pi \left| \langle \psi | \hat{V} | \varphi \rangle \right|^2 \delta(E - \omega)$$
$$= 2\pi v_0^2 |\langle \psi | \partial_x \bar{\tau}_z | \varphi \rangle|^2 \delta(E - \omega) \,. \tag{267}$$

A more general movement profile can be fourier transformed after which the contribution for each fourier component p_ω is given by $\Gamma_{\varphi \to \psi}(p_\omega, \omega)$.

We do not distingish the states the transition happens to; thus we sum over all possible outgoing states other that the initial state. In the continuous system, this would be an integral, but as we do the calculation numerically, we have a discrete set of states. Therefore, we need to broaden the δ-distribution in Equation (267). This is physically justified as the δ-distribution is only valid when evaluating the transition rates at $t \to \infty$, which is not realistic. Instead, decoherence effects occur, broadening the distribution. For simplicity, we consider energies in a range $\omega \pm \Omega$, effectively broadening the δ-distribution to a box of width 2Ω. Additionally, we need to discretize the scattering potential $\hat{V}$, which we do in the same way as the SOC in Section 3.5.1. Putting this together, we obtain the transition rate per energy from the numerical eigenstates as

$$\Gamma(\omega) = \frac{\pi v_0^2}{2a\Omega} \sum_{\substack{i \\ E_i \in [\omega - \Omega, \omega + \Omega)}} \left| \sum_{i_x=1}^{N_x} \sum_{i_y=1}^{N_y} \psi_{i;i_x,i_y} \bar{\tau}_z \left(\varphi_{i_x+1,i_y} - \varphi_{i_x-1,i_y} \right) \right|^2, \tag{268}$$

where the sum over i goes over all states with energies in the box[33] of size 2Ω around ω and $N_x \times N_y$ is the size of the discretized lattice with lattice spacing a. Contributions from outside the sample yield zero as we have hard boundary conditions.

Because of the artificial doubling from the BdG formalism, we have to select either only the positive or the negative energy states. However, since the MBS are degenerate, it is not obvious which one to discard. The numerical diagonalization returns two random basis vectors. $\varphi_a(\mathbf{r})$ and $\varphi_b(\mathbf{r})$ of this subspace, which are not necessarily PHS partners of each other. Thus, we need to find the proper basis so that we can select one of the states. For this, we numerically find a unitary transformation, which is parametrised by

---

[33]We arbitrarily choose to inlude the boundary on the lower end.

$$\bar{U} = \begin{pmatrix} c_1 & c_2 \\ -e^{i\varphi}c_2^* & e^{i\varphi}c_1^* \end{pmatrix} \tag{269}$$

$$c_i \in \mathbb{C} \tag{270}$$

$$\varphi \in [0, 2\pi). \tag{271}$$

With this, we rotate the vectors we get from the diagonalisation and obtain two new vectors

$$\begin{pmatrix} |0\rangle \\ |1\rangle \end{pmatrix} \equiv \bar{U} \begin{pmatrix} |a\rangle \\ |b\rangle \end{pmatrix} \tag{272}$$

$$\langle \mathbf{r}|i\rangle \equiv \boldsymbol{\varphi}_i(\mathbf{r}). \tag{273}$$

The goal of this transformation is that $\boldsymbol{\varphi}_0(\mathbf{r})$ and $\boldsymbol{\varphi}_1(\mathbf{r})$ are PHS partners, up to a global phase that has no physical meaning. Therefore, we need to find a cost function, that is minimal in this case. This function is not unique, but we define with the PHS operator $\hat{\mathcal{C}}$

$$f(\bar{U}) = |1 - |\langle 0|\hat{\mathcal{C}}|1\rangle|| + |1 - |\langle 1|\hat{\mathcal{C}}|0\rangle|| + |\langle 0|\hat{\mathcal{C}}|0\rangle| + |\langle 1|\hat{\mathcal{C}}|1\rangle|. \tag{274}$$

This function is positive and vanishes, when the condition we target is fulfilled because then we have $|\langle i|\hat{\mathcal{C}}|j\rangle| = 1 - \delta_{i,j}$. In this correct basis, the choice of state to use for the Golden rule calculation is irrelevant.

The resulting transition rates are shown in Figure 33 for three different field configurations, all far in the topological regime. There, both the transition rates (**(a)** and **(b)**) and the density of states (**(c)**) are presented. The density of states is relevant, because more states contributing at a certain energy enhance the transition rate. We see two different energy scales that are relevant for the setup. The first one is the topological gap, which is given by the distance from the MBS to the next highest state (in the present case around $\omega \approx 0.3$). In this energy area, there are no target states are available and therefore, in the present approximation, no transitions are possible. The other one is given by the s-wave gap $\Delta = 1$. Inside this gap, only the continuum of standing waves along the one-dimensional channel provides the set of target states. Above this gap, the two-dimensional bulk states are located as well, which causes a higher density of states.

The lowest field case of $B = JM_0 = 3$ stands out and shows a pronounced dip in the transition rate directly below the s-wave gap, which is caused by a reduced density of states. The origin of this is not clear. This effect is also visible in Figure 33 **(b)**, where the medium energy shows highly non-monotonic
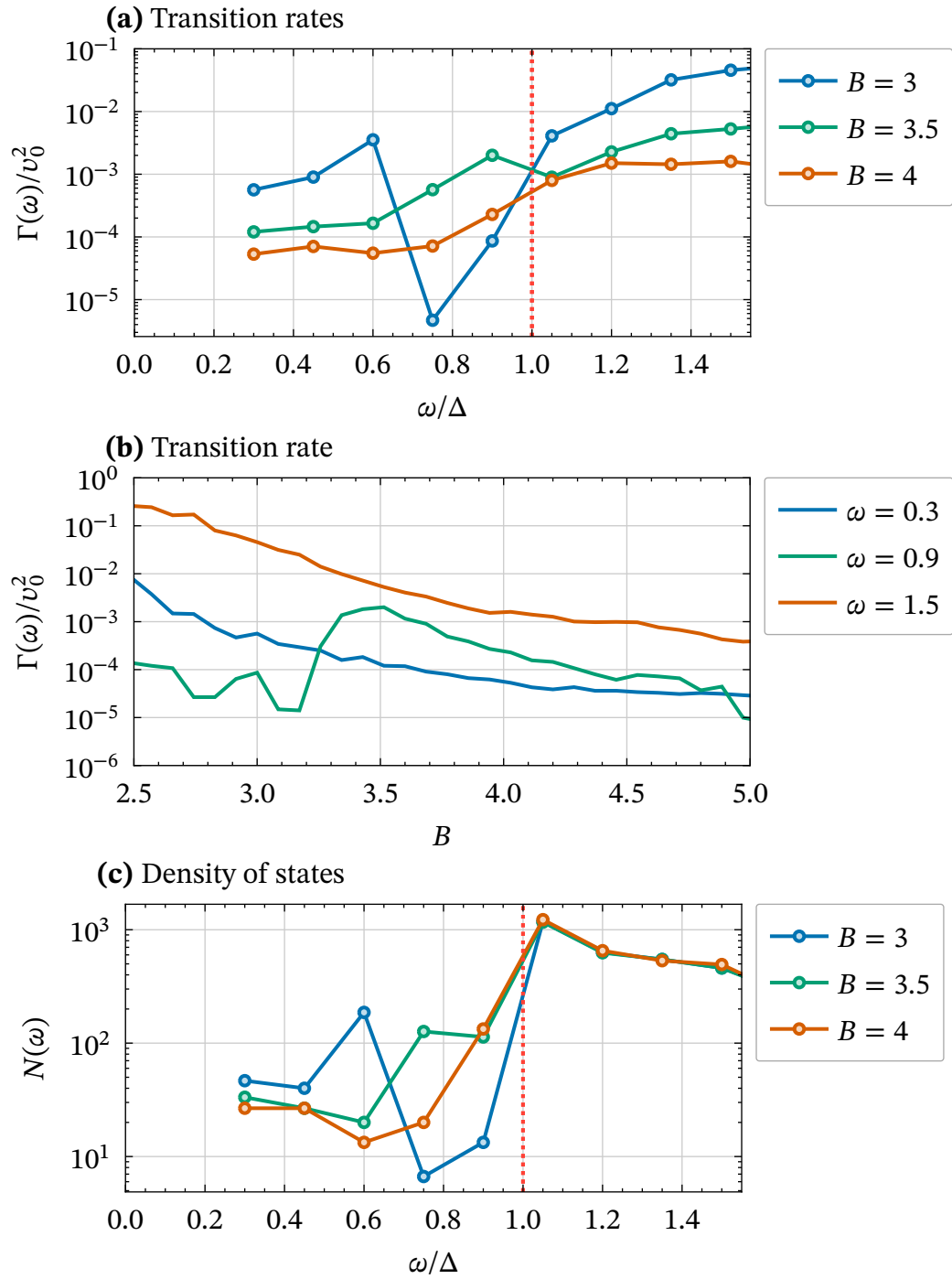
Figure 33: Transition rates according to Fermi's golden rule depending on the energy ω (**(a)**) and the field (**(b)**) and density of states (**(c)**) for $\Omega = 0.15$, $\Delta = 1$, $m = 1$, $\mu = 0$, $w = 0.2$, and $x_0 = 0.02$ and $B = JM_0$. In **(a)** and **(c)** the superconducting gap is marked with a dashed line.

behaviour in the transition rates. At lower and higher energies, though, the transition rates decrease with increasing fields monotonically. Thus, to keep the transition rate low, low energies and high fields are preferred.

As a conclusion, to prevent scattering into other states, the weight of the Fourier components of the velocity above the topological gap should ideally vanish. This also means that a high topological gap is beneficial, which can be achieved by a suitable choice of fields and a high SOC. Also, higher fields make the MBS more stable and less likely to decay into other states.

4.6 Numerical Simulations

We conclude with a more general approach that uses a more direct numerical solution that calculates the time evolution of a starting state. This is implemented with the help of tkwant[129]. The code developed for these simulations is published under Ref. [130]. To make the simulation flexible, the domain wall position is read from a sequence of image files. This makes it possible to use an animation tool like Blender to have full control over the domain wall curve and orientation by drawing images (see Section B.2 for examples). Additionally, a mask can be provided to define the shape of the sample. Therfore, the software is capable of handling arbitrary domain wall paths and samples shapes[34] and thus expand upon the investigations of the prior sections.

In Figure 34, a simple linear motion of a domain wall is presented. The domain wall moves from the left side to the right side of the sample on a timescale of $t_{\max} = 100$ in the natural units of the problem (see Chapter A). The localised state stays basically unchanged and is moved without any scattering. We also confirm the absence of scattering by looking at the integrated Majorana polarisation for a state $\psi(r)$ from above with the PHS operator $\hat{\mathcal{C}}$[126]

$$P(r) \equiv \psi^{\dagger}(r)\hat{\mathcal{C}}\psi(r) \,. \tag{246}$$

p. 88

The quantity is evaluated statically at each snapshot and thus is capturing the momentary behaviour. We can think of this physically as suddenly stopping at that point and then calculating the Majorana polarisation at the moment of

---

[34]The limitation is set by the computation time and computing resources. Especially changing the orientation of the domain wall tends to negatively influence the computation time.

(a) $t = 0$

(b) $t = 33.33$

(c) $t = 66.67$

(d) $t = 100$

(e) position

(f) $\int d\mathbf{r} |P(\mathbf{r})|$

Figure 34: Snapshots of the time evolution of the local probability density $|\psi(\mathbf{r}, t)|^2$ (**(a)** to **(d)**) of a slow moving domain wall, the position of the wall and state along the x-direction (**(e)**), and the momentary integrated Majorana polarisation (**(f)**) for $\Delta = 1$, $m = 1$, $w = 0.2$, $x_0 = 0.02$, $\alpha = 0.8$, $B = 3$, and $JM_0 = 3$. The lattice is disretized with a lattice constant $a = 0.1$ and a size of 79×119. In the snapshots, the current position expectation value and its path it shown in red.

stopping. Up to some fluctuations, the value remains close to 1, indicating that the state keeps its Majorana character. Another value that we can examine is the position expectation value. Additionally, we examine the position expectation value of the MBS $\boldsymbol{\psi}(\boldsymbol{r}, t)$, which is given by

$$\boldsymbol{p}_{\text{MBS}}(t) = \int \mathrm{d}\boldsymbol{r}\, \boldsymbol{r} |\boldsymbol{\psi}(\boldsymbol{r}, t)|^2 . \tag{275}$$

Note that, while this is the classical equivalent of the position of the *fermionic* quasi-particle, the Majorana is not located at this position. In fact, as the expectation value is in the middle of the pair, the local probability density of the MBS is very low there. If the MBS follows the domain wall, we expect a linear motion as well. And indeed, when comparing with the domain wall position we input into the simulation (Figure 34 **(e)**), we observe that the MBS follows closely, while only slightly trailing behind in the end. Therefore, we conclude that the MBS can be moved, at least when the movement happens slow enough, confirming the findings from the adiabatic treatment.

But what happens when the movement is much quicker than in this example? From the previous results, we expect there to be a higher probability for the state to scatter into other states. To investigate this, we perform the same simulation, but on a 10 times smaller timescale (see Figure 35). All other parameters are the same as in Figure 34. Compared to the slow movement, the result is substantially different. Over the course of the movement, the state delocalises more. This is caused by it lagging behind the domain wall (Figure 35 **(e)**) and therefore escaping the bound state. In the beginning, the MBS is following along, but at around $t = 3$ the localisation breaks down. Whether this is mainly caused by the larger velocity or the acceleration has yet to be determined. At the end, the state is so far delocalised that the expected position is close to centre of the sample. There is still some localised part left, which is why the integrated Majorana polarisation (Figure 35 **(f)**) decreases, but only to around 0.6. Consequently, as we established before the movement needs to happen slow enough to not destroy the MBS. This complements and is consistent to the prior analysis in this chapter.

Finally, we come back to slow movement speeds, but simulate a more complex sample geometry (Figure 37). We assume that the magnet is a full strip to not cause a more complicated texture and still facilitate a simple linear motion. The superconductor is patterned and has cut-outs and holes. The chosen shape (see Figure 36) highlights the flexibility of the simulation and acts as a means

(a) $t = 0$ **(b)** $t = 3.33$ **(c)** $t = 6.67$ **(d)** $t = 10$

(e) position

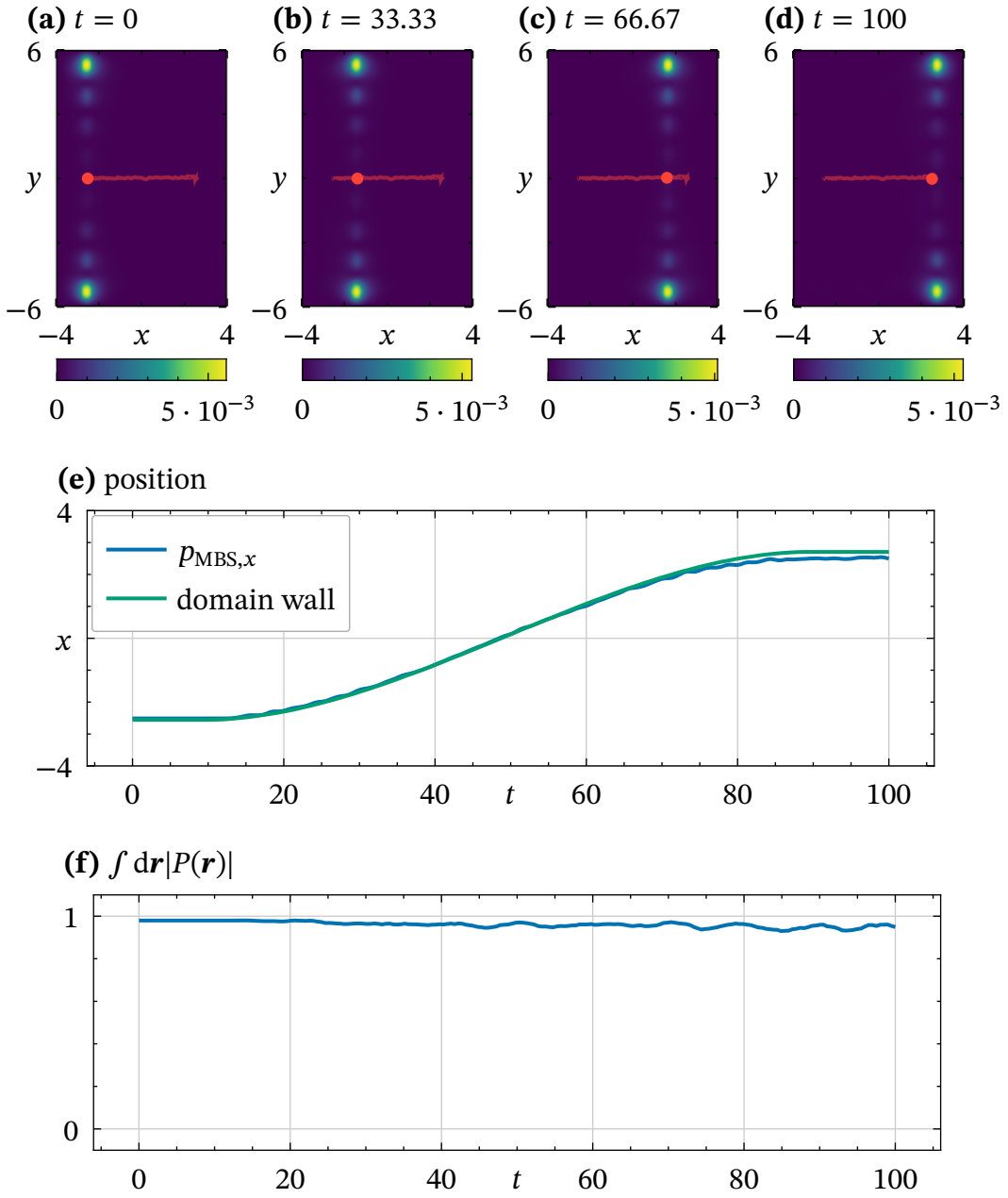**(f)** $\int \mathrm{d}\boldsymbol{r}\,|P(\boldsymbol{r})|$

Figure 35: Snapshots of the time evolution of the local probability density $|\psi(\boldsymbol{r}, t)|^2$ (**(a)** to **(d)**) of a fast moving domain wall, the position of the wall and state along the x-direction (**(e)**), and the momentary integrated Majorana polarisation (**(f)**) for $\Delta = 1$, $m = 1$, $w = 0.2$, $x_0 = 0.02$, $\alpha = 0.8$, $B = 3$, and $JM_0 = 3$. The lattice is disretized with a lattice constant $a = 0.1$ and a size of 79×119. In the snapshots, the current position expectation value and its path it shown in red.
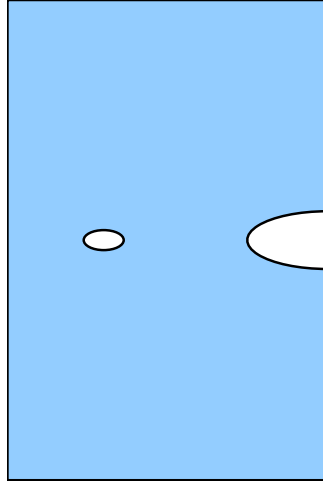
Figure 36: Example geometry used in the simulation in fig Figure 37. The coloured region marks the area that is part of the lattice.

to explore the stability of the MBS for future investigation, for example into possible braiding geometries. On the one hand, the simulation shows that when faced with obstacles, the bound state stays fairly robust and still follows the domain wall. The decreased Majorana polarisation indicates on the other hand that the states hybridises with higher energy states and looses its Majorana nature. To learn more about the robustness of the MBS when moving around obstacles, a more rigorous approach would be needed. Nevertheless, a certain resilience is already visible in this example.

To summarize the results of this full numerical treatment, we confirmed the findings from before and demonstrated that MBSes can be moved by moving the domain wall and even show a certain stability towards sample shape defects. We also showed that moving the domain wall too quickly results in the MBS lagging behind and being delocalised.

(a) $t = 0$

(b) $t = 33.33$

(c) $t = 66.67$

(d) $t = 100$

(e) position

(f) $\int \mathrm{d}\boldsymbol{r}\,|P(\boldsymbol{r})|$
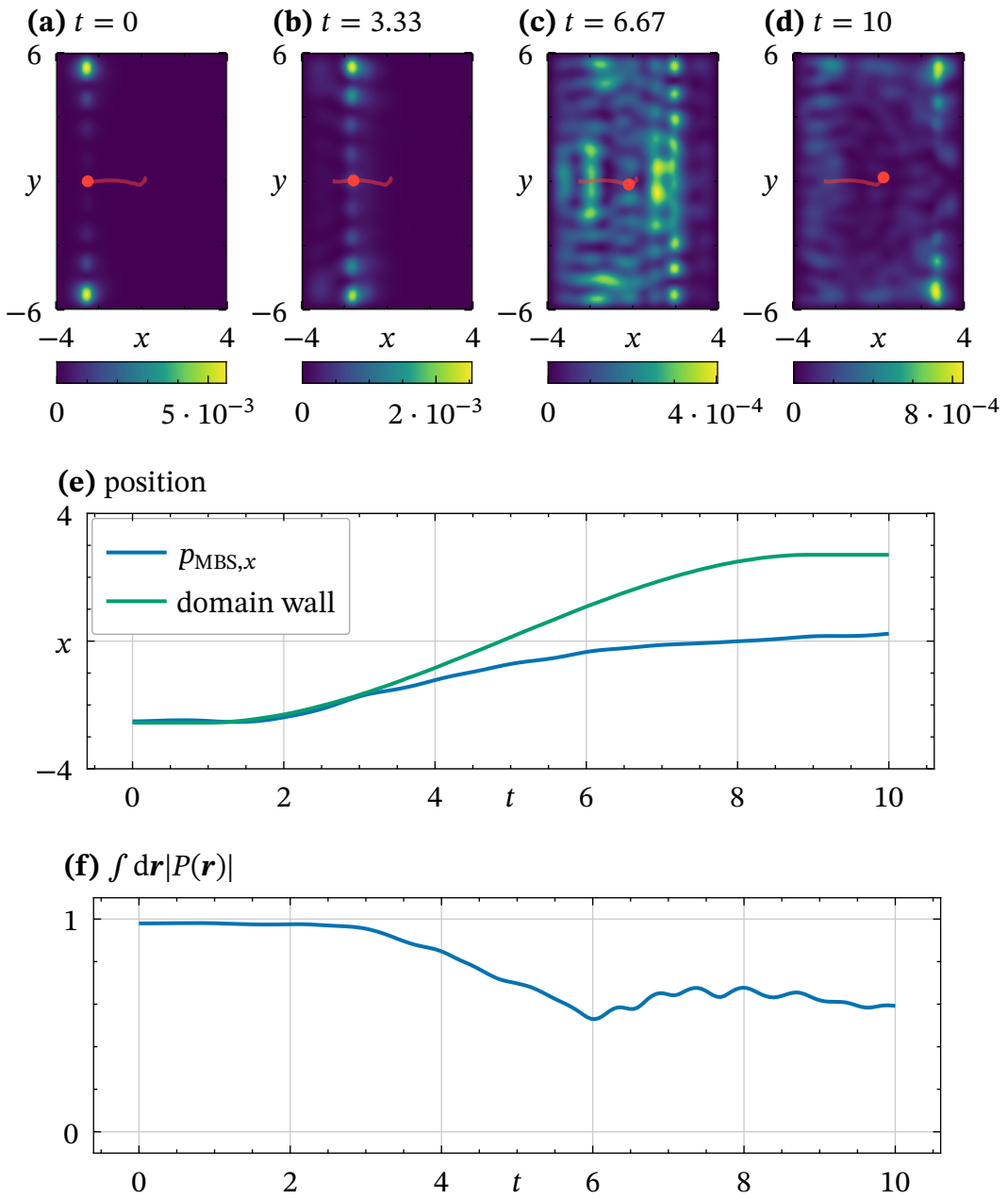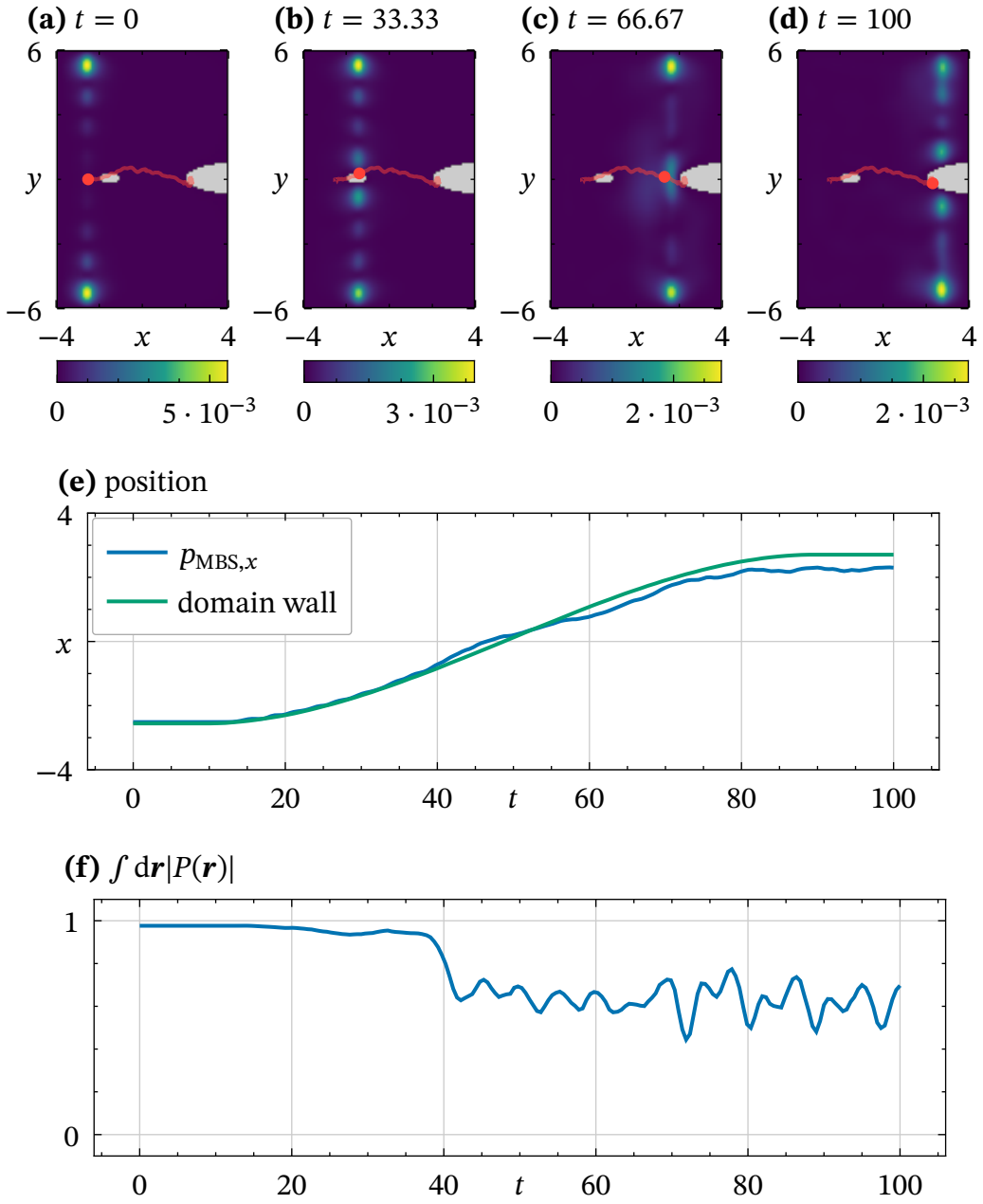
Figure 37: Snapshots of the time evolution of the local probability density $|\psi(\boldsymbol{r}, t)|^2$ (**(a)** to **(d)**) of a slow moving domain wall, in a complex geometry (Figure 36) the position of the wall and state along the x-direction (**(e)**), and the momentary integrated Majorana polarisation (**(f)**) for $\Delta = 1$, $m = 1$, $w = 0.2$, $x_0 = 0.02$, $\alpha = 0.8$ and $B = JM_0 = 3$. The lattice is disretized with a lattice constant $a = 0.1$ and a size of 79×119. In the snapshots, the current position expectation value and its path it shown in red. The gray area is not part of the lattice.

Conclusion 5

As a closure, we summarize the findings. For this, we refer to both main chapters of this work and first discuss the static case and the effect of various parameters in the system. Afterwards, we give an overview of the results regarding the dynamical behaviour. Finally, we give an outlook of possible future research directions and uses of the platform.

5.1 Summary

We examined magnet-superconductor hybrids (MSHes) consisting of an s-wave superconductor with strong spin-orbit coupling (SOC) and an in-plane 2π domain wall in the magnet.

First, we explored the topology of the system (Section 3.3) and argued that a pure in-plane character of the fields is necessary due to Pauli limiting. This, in addition to the simple access to dynamical features marks an important advantage of our setup.

Afterwards, we numerically confirmed the existence of Majorana bound states (MBSes) in the system by both looking at an infinite bulk system (Section 3.6.1) and also a finite one as well (Section 3.6.2). Most of the analysis was performed on a double Ising wall, but we confirmed the applicability for smoother domain walls (Section 3.6.4). We discussed the influence of the fields and geometric features of the domain wall on the topological region. This gives directions for possible materials and setups for experiments. On the superconducting side, we need s-wave pairing and SOC. The SOC should be as large as possible to obtain well localized MBSes and a large topological gap. To be compatible with the formation of the desired magnetic texture, the superconductor has to be coupled with an anti-ferromagnetic exchange coupling to the magnetic layer. The magnet, on the other hand, requires a strong easy-plane anisotropy to achieve a purely in-plane texture. Additionally, an easy-axis anisotropy parallel to the desired wall direction is needed and is one of the ingredients, together with the magnetic stiffness, for tuning the domain wall width and shape at a specified magnetic field. The field influences those parameters as well, but is restricted through the requirement of finding topology in the system. For the wall shape, some fine-tuning has to be done to be in a

regime, where the wall is thin enough to provide an effective one-dimensional channel, but also not too thin as this rises the required field strengths. We mostly investigated sharp Ising-like walls, but justified the usage of smoother profiles. The field configuration that provides optimal conditions for finding topology is found at the point where the external field and the magnetisation contribute approximately equal energies and are large enough to move the system into the topological phase. Finally, it is beneficial for the superconductor to not extend past the magnetic layer, as this restricts the topological phase.

In addition to the investigation of the static case, we also investigated the dynamics of moving the MBS (Chapter 4). This is facilitated by the movement of the domain walls in the magnet, which is possible with spin currents[39–43]. We confirmed this and examined the behaviour depending on the movement. Furthermore, we developed and applied a flexible software for complex domain wall paths and geometries and laid the groundwork for the investigation of complicated dynamical systems.

To summarize, we confirmed magnetic 2π domain walls are a feasible platform for Majorana devices both for realising static and mobile Majoranas.

5.2 Outlook

This work confirmed the capability to host MBSes of MSHes with magnetic 2π domain walls. While we analysed the influence of most parameters, there are more unanswered questions, especially around wider domain walls at higher fields. Therefore, further research into the topology and character of the in-gap states in these situations is of interest.

Further calculations would aid the experimental search for MBSes, for example in the choice of possible materials. Additionally, self-consistent simulations might be necessary for the interpretation of experiments to include the influence of the superconductor on the magnetic layer.

On the theoretical side, there are various interesting future research directions building upon the found MBSes. For example, more investigations could shed light on possible braiding protocols. We showed that MBSes can be moved, but how to braid them has yet to be investigated, especially into the direction of selecting a suitable sample geometry. Typical t-junctions[8,24] are difficult to apply with in-plane domain walls because the field direction at the intersection is ill-defined. Therefore, different geometries have to be designed and tested.

Additionally, for the application of braiding multiple pairs of Majoranas are required[5].

This leads us to another possible application and future direction. Using multiple domain walls on a ribbon, we can build two chains of Majoranas. By controlling the magnetic texture, the distance and thus the coupling between the Majorana sites can be tuned as well.

In conclusion, there are enticing prospect of both theoretical and experimental nature for further studies.

Acknowledgements 6

This work would not have been possible without the assistance of many people. I want to mention some of them here, but this list is not exhaustive.

First and foremost, I would like to thank my supervisor Prof. Dr. Markus Garst for providing me with the opportunity and environment to do this research and offering countless hours of his time for discussions. Secondly, I very much appreciate Prof. Dr. Alexander Shnirman co-supervising this work and providing me with guidance and reassurance.

I am truly grateful to Riccardo Ciola, Lars Franke, and Dr. Paul Pöpperl for many constructive discussions about physics and moral support during this endeavour. Furthermore, many thanks to Dr. Andreas Poenicke, not just for the technical support but also the many great teaching experiences he provided me with and the many interesting conversations. Dr. Stefan Rex helped me immensely with getting started.

As well, the state of this work would not be the same without careful proofreading. Many thanks go to Andrea Hauck, Dr./VAK Moscow Victoria Tokareva, Dr. Paul Pöpperl, Riccardo Ciola, Sebastian Kalt, and Kirsten Bark, who took the valuable time to read this text and suggest corrections.

Last, but certainly not least, I want to express my gratitude for all the love and support I get from my friends, family, and above all, my partner, Dr./VAK Moscow Victoria Tokareva. You made me believe in myself and my capability to do this. I could not have done it without you.

Units and Scales

A

In this work, we chose suitable dimensionless units that make the analytical treatment of the problem more comfortable. The choice used here is also very common in the literature[30,32]. For comparison with experiments and a more in-depth understanding of the physical implications, it is still useful to have the option to convert quantities to SI units. In the following, we are denoting a quantity x in SI units as x_{SI}. As a reminder, the Hamiltonian discussed before has the form

$$\hat{H} = \left(-\frac{\hat{\mathbf{V}}^2}{2m} - \mu\right)\bar{\tau}_z + \Delta\bar{\tau}_x - J\mathbf{M}(x) \cdot \bar{\sigma} + B\bar{\sigma}_y + i\alpha(\hat{\mathbf{V}} \times \bar{\sigma})\bar{\tau}_z \quad (131)$$

$$\bar{\sigma}_i = \bar{\bar{\mathbb{1}}}_2 \otimes \bar{\Sigma}_i$$

$$\bar{\tau}_i = \bar{\Sigma}_i \otimes \bar{\bar{\mathbb{1}}}_2$$

$$\mathbf{M}(x) = M_0 \begin{pmatrix} \sin(\theta(x)) \\ \cos(\theta(x)) \\ 0 \end{pmatrix} \quad (132)$$

$$\theta(x) = 2\arctan\left(\frac{\sinh\left(\frac{x}{x_0}\right)}{\sinh\left(\frac{w}{x_0}\right)}\right) - \pi. \quad (133)$$

<div style="text-align:right">p. 45, p. 46</div>

In SI units, this reads

$$\hat{H}_{\mathrm{SI}} = \left(-\hbar^2\frac{\hat{\mathbf{V}}^2_{\mathrm{SI}}}{2m_{\mathrm{SI}}} - \mu_{\mathrm{SI}}\right)\bar{\tau}_z + \Delta_{\mathrm{SI}}\bar{\tau}_x - J_{\mathrm{SI}}\mathbf{M}_{\mathrm{SI}}(x_{\mathrm{SI}}) \cdot \bar{\sigma}$$

$$+ \mu_{\mathrm{B}}B_{\mathrm{SI}}\bar{\sigma}_y + i\alpha_{\mathrm{SI}}\hbar(\hat{\mathbf{V}}_{\mathrm{SI}} \times \bar{\sigma})\bar{\tau}_z. \quad (277)$$

To get dimensionless quantities, we need to define two scales. The first one is an energy scale, for which we pick the gap Δ_{SI}. This choice is not unique, but the superconducting gap is the most important energy scale in the system, as it gives an upper bound for the topological gap and hence protection. Furthermore, we set a length scale. Again, here we have many choices and select one that is convenient for the numerical calculations. This length scale is obtained by forcing the dimensionless mass m to be unity, yielding

Table 3: Conversion of the quantities of the system between SI units and the dimensionless units used in this work.

quantity	from SI	to SI
superconducting gap	$\Delta = 1$	Δ_{SI}
mass	$m = 1$	m_{SI}
Hamiltonian	$\hat{H} = \hat{H}_{\mathrm{SI}} \dfrac{1}{\Delta_{\mathrm{SI}}}$	$\hat{H}_{\mathrm{SI}} = \Delta_{\mathrm{SI}} \hat{H}$
chemical potential	$\mu = \mu_{\mathrm{SI}} \dfrac{1}{\Delta_{\mathrm{SI}}}$	$\mu_{\mathrm{SI}} = \mu \Delta_{\mathrm{SI}}$
inter-layer coupling	$J = J_{\mathrm{SI}} \dfrac{1}{\mu_0 \mu_{\mathrm{B}}}$	$J_{\mathrm{SI}} = J \mu_0 \mu_{\mathrm{B}}$
magnetisation amplitude	$M_0 = M_{0,\mathrm{SI}} \dfrac{\mu_0 \mu_{\mathrm{B}}}{\Delta_{\mathrm{SI}}}$	$M_{0,\mathrm{SI}} = M_0 \dfrac{\Delta_{\mathrm{SI}}}{\mu_0 \mu_{\mathrm{B}}}$
spin-orbit coupling	$\alpha = \alpha_{\mathrm{SI}} \dfrac{1}{\hbar} \sqrt{\dfrac{m_{\mathrm{SI}}}{\Delta_{\mathrm{SI}}}}$	$\alpha_{\mathrm{SI}} = \alpha \hbar \sqrt{\dfrac{\Delta_{\mathrm{SI}}}{m_{\mathrm{SI}}}}$
wave vector	$\boldsymbol{k} = \boldsymbol{k}_{\mathrm{SI}} \dfrac{\hbar}{\sqrt{m_{\mathrm{SI}} \Delta_{\mathrm{SI}}}}$	$\boldsymbol{k}_{\mathrm{SI}} = \boldsymbol{k} \dfrac{\sqrt{m_{\mathrm{SI}} \Delta_{\mathrm{SI}}}}{\hbar}$
space derivative	$\hat{\boldsymbol{\nabla}} = \hat{\boldsymbol{\nabla}}_{\mathrm{SI}} \dfrac{\hbar}{\sqrt{m_{\mathrm{SI}} \Delta_{\mathrm{SI}}}}$	$\hat{\boldsymbol{\nabla}}_{\mathrm{SI}} = \hat{\boldsymbol{\nabla}} \dfrac{\sqrt{m_{\mathrm{SI}} \Delta_{\mathrm{SI}}}}{\hbar}$
magnetic field	$B = B_{\mathrm{SI}} \dfrac{\mu_{\mathrm{B}}}{\Delta_{\mathrm{SI}}}$	$B_{\mathrm{SI}} = B \dfrac{\Delta_{\mathrm{SI}}}{\mu_{\mathrm{B}}}$
domain wall width	$w = w_{\mathrm{SI}} \dfrac{\sqrt{m_{\mathrm{SI}} \Delta_{\mathrm{SI}}}}{\hbar}$	$w_{\mathrm{SI}} = w \dfrac{\hbar}{\sqrt{m_{\mathrm{SI}} \Delta_{\mathrm{SI}}}}$
domain wall scale	$x_0 = x_{0,\mathrm{SI}} \dfrac{\sqrt{m_{\mathrm{SI}} \Delta_{\mathrm{SI}}}}{\hbar}$	$x_{0,\mathrm{SI}} = x_0 \dfrac{\hbar}{\sqrt{m_{\mathrm{SI}} \Delta_{\mathrm{SI}}}}$

$$\Lambda_{\mathrm{SI}} \equiv \frac{\hbar}{\sqrt{m_{\mathrm{SI}} \Delta_{\mathrm{SI}}}} \,. \tag{278}$$

With that, we obtain the dimensionless quantities by rescaling everything. On the SI unit side, the superconducting gap Δ_{SI} and the effective mass m_{SI} are used as externally determined input parameters. For the magnetisation term $J\boldsymbol{M}$ only the product is significant. Thus, we only use the combination when discussion values. The resulting conversions are collected in Table 3. Even though Δ and m are fixed, we still keep them in all formulas to be consistent with the literature and also to make it easier to follow the physical meaning of terms.

Software B

In this section, the main pieces of software developed and used during this work are documented. First, a tutorial for the software used to analyse the static problem is given[131]. Afterwards, the software for the full numerical treatment of the time-dependent system is introduced[130].

B.1 Diagonalisation of the Static Problem

This software, in the following referred to as `mbscluster`[131], simulates superconductor magnet hybrids with a 2π domain wall in the magnet and targets highly parallel environments[35] like computing clusters. The functionality is exposed through several scripts. This guide will walk you through a simple example.

B.1.1 Discretisation

Before going into the usage of the software, we first shortly discuss the implemented discretisation procedure.

B.1.2 Installation

In general, there are two options to run the code:

- Using a locally installed Python interpreter and to install it locally
- Using the provided Apptainer image
- Using a locally installed Python interpreter and PDM to run it directly from the folder

As the environment will differ between clusters, some details might need to be adjusted. The necessary commands will be given for the bwUnicluster2.0 as

---

[35]Facilitated by MPI and the corresponding Python binding[132].

this is where development and testing is happening. You don't need to follow both guides, one is sufficient.

Local Python Installation

In addition to Python, some external dependencies that cannot be handled by PDM are required. Mainly, the code depends on MPI for parallelization. Theoretically, all MPI versions should work, but the code is only tested with OpenMPI. So before getting started, install the following dependencies:

- Python, at least version 3.9 is required via `pip`/`pipx`/...
- OpenMPI, including the development headers, which might be in a separate

package depending on your system

On a cluster, Python and OpenMPI are typically available through a module system. On the bwUnicluster2.0, the corresponding modules can be loaded with

```
module load devel/python mpi/openmpi
```

Now you can install the package. It is very much recommended to install it into a virtual environment. This can be done manually, but also with tools like `pipx`.

pip	pipx
`pip install .`	`pipx install .`

This provides all the scripts in the path and also installs the library itself.

Apptainer

Another option is to run the software in a container. Due to how MPI works, there are still external dependencies required. Therefore, install the following things first

- Apptainer package depending on your system
- OpenMPI, including the development headers, which might be in a separate package depending on your system

If you want to run the code on a cluster, this has to be handled by the cluster administration. OpenMPI is typically available through a module system. On the bwUnicluster2.0, the corresponding modules can be loaded with

```
module load devel/python mpi/openmpi
```

The Apptainer container can be downloaded from the supplementary data[60] or built from scratch using

```
apptainer build mbscluster.sif
```

When running the container, it is important to make sure that the necessary folders are mounted. Which these are will depend on your system. For the bwUnicluster2.0, the typical candidates are `/scratch`, `/pfs` and maybe the LSDF storage. Mounts have to be given to all commands, so make sure to add the corresponding `--bind` arguments.

B.1.3 Configuration

While all parameters can also be given as runtime arguments, some options can also be configured in a configuration file. This is read (if the file exists) from the following places:

- `/etc/mbs.ini`
- `$XDG_CONFIG_HOME/mbs.ini` (typically `~/.config/mbs.ini`)
- `config.ini` in the current working directory
- optionally at the location given with a runtime argument

The only available options are currently the paths. For example, the file in Listing 1 would configure the simulation output to land in `~/.local/share/mbs/data`, plots in `~/mbs/plots` and exported text files in `~/mbs/export`. What is meant with this will be explained later in the example.

B.1.4 Minimal Example

Having setup everything, you are now ready to run our first example. Make sure that you have either setup the output paths in a configuration file (Section B.1.3)

```
1  [general]
2  data_path = ./output/data
3
4  [plot]
5  output = ./output/plot
6
7  [export]
8  output = ./output/export
```

Listing 1: Example configuration file which configures the relevant paths.

or pass them with each call. The next sections will guide you through running a simple simulation. The files created here can also be found in the examples folder[131].

B.1.5 Parameters

The first step is to write a Python file, that generates the list of parameters. The file has to contain a function, called `parameters()`, that gets no arguments and returns a NumPy array of tuples with an integer id and a `Parameters` object. Refer to the API documentation[36] for more details. A minimal example is presented in Listing 2 that sweeps over a single parameter.

> **Warning**
>
> The pairing of ids to parameter objects has to be **unique** and **consistent** between runs. Otherwise, you will run into troubles as the hash of the file is used for being able to continue aborted runs. Therefore, all random behaviour has to be initialized with a seed.

```python
1  import numpy as np
2
3  from mbs.db import Parameters
4
5
6  def parameters() -> np.ndarray:
7      return np.array([(0, Parameters())])
```

---

[36]This is both available under https://mbscluster.gitlab.io/mbscluster/api and in the supplementary data[60].

Listing 2: Minimal parameter script that contains a sweep over a single parameter, here `alpha`.

Single Parameter Sweep

The next example in Listing 3 would run the simulation on a single set of parameters initialized to the default parameters. In reality, we want to run the simulation for a list of parameters. So let us extend this to a more realistic example that overwrites default parameters and runs a sweep over the spin obit coupling strength `alpha`.

```python
import numpy as np

from mbs.db import Parameters


def parameters() -> np.ndarray:
    alpha_values = np.linspace(0.1, 1.0, 4)
    return np.array(
        list(
            enumerate(
                map(
                    lambda alpha: Parameters(
                        a=0.1,  # lattice parameter
                        w=0.2,  # domain wall width
                        x0=0.02,  # domain wall scale
                        alpha=alpha,  # spin-orbit coupling
                    ),
                    alpha_values,
                )
            )
        )
    )
```

Listing 3: Parameter script that sweeps over a single parameter, here `alpha`.

Multi-Parameter Sweep

But what if we would like to run a sweep over multiple parameters? Let's consider this example:

```python
1   import numpy as np

2

3   from mbs.db import Parameters
4   from mbs.util import prod_space

5

6

7   def new_parameters(pars: tuple[float, float, float]) → Parameters:
8       w, b, m0 = pars
9       return Parameters(
10          a=0.2,  # lattice parameter
11          alpha=0.3,  # spin-orbit coupling
12          w=w,  # domain wall width
13          x0=0.1 * w,  # domain wall scale
14          b=b,  # magnetic field
15          m0=m0,  # magnetization amplitude
16          n1=31,  # number of points for the 1d simulation
17          n2x=11,  # number of points for the 2d simulation in x-direction
18          n2y=31,  # number of points for the 2d simulation in y-direction
19      )

20

21

22  def parameters() → np.ndarray:
23      w = np.geomspace(0.2, 0.4, 2)
24      b = np.linspace(0.0, 5.0, 31)
25      m0 = np.linspace(0.0, 5.0, 31)
26      pars = np.array(list(enumerate(map(new_parameters, prod_space(w, b, m0)))))
27      return pars
```

Listing 4: Parameter script that sweeps over multiple parameters.

- sweep over magnetic field b and magnetisation amplitude m0
- domain wall width w values 0.2 and 0.4
- domain wall scale x0 should always be 0.1 * w

We could calculate all combinations manually, but the mbs.util provides a handy function prod_space() which does this for us. This combines to the code in Listing 4.

Shuffling Things Around

While not strictly necessary, it can be helpful to shuffle the list (see Listing 5). That way, intermediate results while the simulation is still running might be more helpful.

> **Warning**
>
> As mentioned before, the paring of ids and parameter sets has to be unique. So be careful here and only shuffle after enumerating.

```python
import numpy as np

from mbs.db import Parameters
from mbs.util import prod_space


def new_parameters(pars: tuple[float, float, float]) → Parameters:
    w, b, m0 = pars
    return Parameters(
        a=0.2,  # lattice parameter
        alpha=0.3,  # spin-orbit coupling
        w=w,  # domain wall width
        x0=0.1 * w,  # domain wall scale
        b=b,  # magnetic field
        m0=m0,  # magnetization amplitude
        n1=31,  # number of points for the 1d simulation
        n2x=11,  # number of points for the 2d simulation in x-direction
        n2y=31,  # number of points for the 2d simulation in y-direction
    )

def parameters() → np.ndarray:
    w = np.geomspace(0.2, 0.4, 2)
    b = np.linspace(0.0, 5.0, 31)
    m0 = np.linspace(0.0, 5.0, 31)
    pars = np.array(list(enumerate(map(new_parameters, prod_space(w, b, m0)))))
    np.random.shuffle(pars)
    return pars
```

Listing 5: Parameter script that sweeps over multiple parameters and shuffles them.

Running the Simulation

Having prepared our `parameters.py` file and configured the output folders, we can now run the simulation with the following command:

Local	PDM	Apptainer
`mbs`	`pdm` run mbs	`apptainer` run mbscluster.sif

You can also run it with MPI for parallelization. The MPI command and arguments might be different on your system, here default settings and 8 processes are used.

Local	PDM	Apptainer
`mpirun -np 8 mbs`	`mpirun -np 8 pdm run mbs`	`mpirun -np 8 apptainer run mbscluster.sif`

In general, this command and the others offer optional arguments. Refer to the help (available with the `--help` argument) to get more details.

> **Warning**
>
> On a desktop or laptop, the simulation might take a long time with the given parameters. You can adjust the size (`n1`, `n2x`, `n2y`) or the number of points for the sweep to get a quicker, but worse result. You can proceed to the plotting already before the simulation is finished, as it will also work on partial results. In very early stages when very little points are available, some things might break, though.

Monitoring the Simulation

While the simulation is running, you can check the status with

Local	PDM	Apptainer
`mbsmonitor`	`pdm` run mbsmonitor	`apptainer` run --app monitor mbscluster.sif

This should give you something similar to this output

name	results	ETA

2024-10-16T16:44:16.417038	65/1922	1:26:11

Examining the Result Data

Let's have a look now, what exactly is generated by this command. Your output folder will look like this:

- `state.pickle`: Current simulation state, used for resuming calculations
- `2024-10-16T16:44:16.417038`: Session results (with your session name of course)
  - ‣ `data.db`: SQLite database containing the parameters and the pairing to the result files
  - ‣ `parameters.py`: Copy of the parameters file used for the simulation
  - ‣ `session.pickle`: Pickled session information
  - ‣ `000000...`: Results for one set of parameters
    - `meta.pickle`: Pickled metadata
    - `vals_1d.npy`: Array with eigenvalues of 1d Hamiltonian
    - `vecs_1d.npy`: Array with eigenvectors of 1d Hamiltonian
    - `vals_2d.npy`: Array with eigenvalues of 2d Hamiltonian
    - `vecs_2d.npy`: Array with eigenvectors of 2d Hamiltonian
    - `prob.npy`: Probability for the system to remain groundstate with a suddenly moving potential (see the API Documentatoin)

Plotting the Results

Simple predefined plots can be generated by just calling the plotting script.

Local	PDM	Apptainer
`mbsplot`	`pdm run mbsplot`	`apptainer run --app plot mbscluster.sif`

This looks at which parameters are changing in this session and generates plots for each pair of changing parameters. If they are linearly dependent, simple line plots are generated, otherwise a density plot. For our example, the pair of
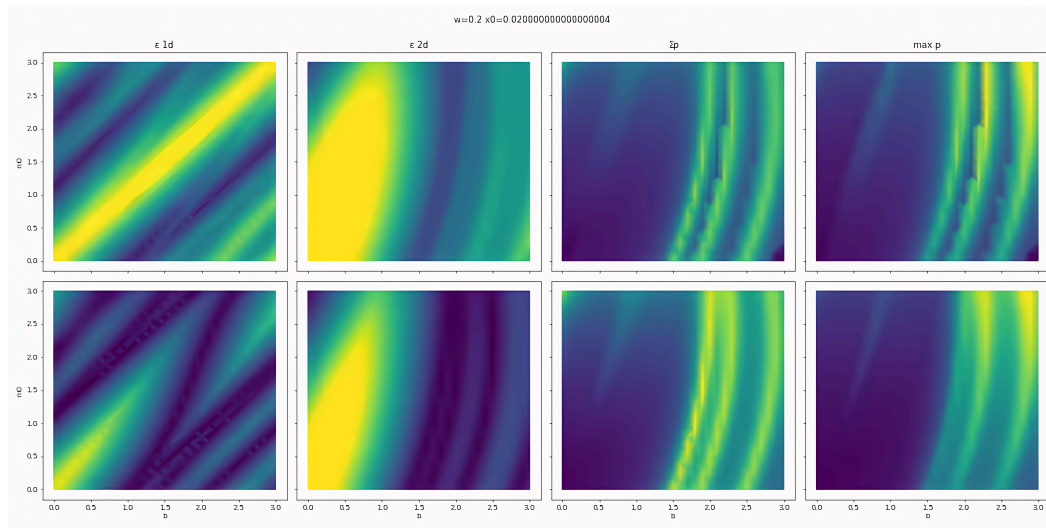
Figure 38: Output of `mbsplot`. Presented are bulk and finite system energies and bot the summed Majorana polarisation and its maximum. The bottom row corresponds to the lowest and the top row to the second lowest state in energy respectively.

`b` and `m0` is the most interesting. If the plot command takes too long, you can also specify `-r b,m0` to ignore the other changing parameters.

In the folder `b_m0` you will find multiple images. Each corresponds to a set of values for the remaining parameters. By default, only a maximum number of 10 sets is taking, but this can be overwritten with the `--plots` argument. Here, we only have 2, corresponding to the two values of `w` (remember that `x0` is not changing independently).

Let's examine the first one in more detail (see Figure 38). We calculated the four lowest eigenvalues. By construction, we have a particle-hole symmetry that creates pairs of states with energy $\pm\varepsilon$ that have the same probability density $|\psi_\pm|^2$. Thus, it's enough to only look at one state per pair. In the resulting plot, there are eight plots arranged in two rows. Each row corresponds to one pair of states, with the lowest energy one being on the bottom. For each state, four quantities are plotted as a density plot over the two selected changing quantities. The values for the others are listed in the title (in our case, there are two plots corresponding to the two domain wall widths). Those four quantities are

- ε 1d: energy in an infinite 1d system in y-direction at $k_y = 0$
- ε 2d: energy in the finite 2d system
- $\sum p$: sum of Majorana polarisation over the whole 2d sample

```python
1   import os
2   from pathlib import Path
3
4   from mbs.db import get_runs
5   from mbs.scripts.config import get_config
6
7   conf = get_config()  # read configuration files
8   data_path = Path(
9       os.path.expanduser(conf.get("general", "data_path"))
10  )  # obtain configured data path and expand ~
11  runs = get_runs(data_path)  # get list of runs
12
13  for session, database_path in runs:
14      print(session.name)
```

Listing 6: Custom script that list sessions.

- max p: Maximum value of Majorana polarisation over the whole 2d sample

Signs for Majoranas are:

- ε 1d: as large as possible as this determines the topological gap
- ε 2d: as close as possible to zero
- $\sum p$: as large as possible
- max p: as large as possible

B.1.6 Accessing the Results From Python

So far, we only used the predefined scripts. Those can only get you so far, and sometimes a more flexible approach is needed. It is also possible to access the data from a custom Python script. This is only possible when using a local Python interpreter to run the code (see the local installation part in Section B.1.2 for setup instructions). This tutorial does not go into the details of all possible functions, for this, refer to the documentation. If you are using the library directly from the folder, make sure to run your scripts also inside the PDM managed virtual environment with `pdm run python $FILE`.

We start by grabbing the saved simulation runs like shown in Listing 6. This should output something like (with different session names of course)

```
2025-07-14T14:37:09.840098
2025-07-14T14:43:25.664730
```

```python
1   import os
2   from pathlib import Path
3
4   from mbs.db import Database, get_runs
5   from mbs.scripts.config import get_config
6
7   conf = get_config()  # read configuration files
8   data_path = Path(
9       os.path.expanduser(conf.get("general", "data_path"))
10  )  # obtain configured data path and expand ~
11  runs = get_runs(data_path)  # get list of runs
12
13  for session, database_path in runs:
14      print(session.name)
15      with Database(database_path) as db:
16          results = db.get_results()
17          for num, parameters, _metadata in results:
18              print("\t", f"{num:>6}: {parameters}")
```

Listing 7: Custom script that list sessions and reads metadata from the database.

```
2025-07-14T15:04:00.595131
2025-07-14T13:26:59.801148
2025-07-14T14:54:44.871032
```

As a next step, we can open the database and obtain the association of result ids to parameters and metadata (Listing 7) resulting in something like

```
2025-07-14T14:37:09.840098
     296: a=0.2 m=1.0 mu=0.0 delta=1.0 alpha=0.3 …
     772: a=0.2 m=1.0 mu=0.0 delta=1.0 alpha=0.3 …
    1479: a=0.2 m=1.0 mu=0.0 delta=1.0 alpha=0.3 …
     682: a=0.2 m=1.0 mu=0.0 delta=1.0 alpha=0.3 …
     286: a=0.2 m=1.0 mu=0.0 delta=1.0 alpha=0.3 …
     866: a=0.2 m=1.0 mu=0.0 delta=1.0 alpha=0.3 …
     715: a=0.2 m=1.0 mu=0.0 delta=1.0 alpha=0.3 …
     472: a=0.2 m=1.0 mu=0.0 delta=1.0 alpha=0.3 …
    1756: a=0.2 m=1.0 mu=0.0 delta=1.0 alpha=0.3 …
```

Filtering

`get_results()` is powerful, but also complicated. It takes an optional `conditions` argument with a list of selectors that are inserted into the SQL query and combined with AND operations. Let us now filter to only get the results,

```python
1   import os
2   from pathlib import Path
3
4   from mbs.db import Database, get_runs
5   from mbs.scripts.config import get_config
6
7   conf = get_config()  # read configuration files
8   data_path = Path(
9       os.path.expanduser(conf.get("general", "data_path"))
10  )  # obtain configured data path and expand ~
11  runs = get_runs(data_path)  # get list of runs
12
13  for session, database_path in runs:
14      print(session.name)
15      with Database(database_path) as db:
16          results = db.get_results(conditions=["w > 0.19", "w < 0.21"])
17          for num, parameters, _metadata in results:
18              print("\t", f"{num:>6}: {parameters}")
```

Listing 8: Custom script that list sessions and reads metadata from the database.

which belong to `w=0.2`. With floats, it is never a good idea to check for exact equality. Thus, we check for it being in a small range. The script in Listing 8 results in an output similar to the following:

```
2025-07-14T14:37:09.840098
    213: a=0.2 m=1.0 mu=0.0 delta=1.0 alpha=0.3 …
    400: a=0.2 m=1.0 mu=0.0 delta=1.0 alpha=0.3 …
    505: a=0.2 m=1.0 mu=0.0 delta=1.0 alpha=0.3 …
    566: a=0.2 m=1.0 mu=0.0 delta=1.0 alpha=0.3 …
    580: a=0.2 m=1.0 mu=0.0 delta=1.0 alpha=0.3 …
    633: a=0.2 m=1.0 mu=0.0 delta=1.0 alpha=0.3 …
    682: a=0.2 m=1.0 mu=0.0 delta=1.0 alpha=0.3 …
    688: a=0.2 m=1.0 mu=0.0 delta=1.0 alpha=0.3 …
    772: a=0.2 m=1.0 mu=0.0 delta=1.0 alpha=0.3 …
```

Reading the Data

Now that we filtered for the result we are interested in, we can read the actual data from the files. For the case of this tutorial, we are only reading the eigenvalues of the finite 2d simulation. We achieve this by telling the result object to skip reading the rest.

```python
1   import os
2   from pathlib import Path
3
4   from mbs.db import Database, Result, get_runs
5   from mbs.scripts.config import get_config
6
7   conf = get_config()  # read configuration files
8   data_path = Path(
9       os.path.expanduser(conf.get("general", "data_path"))
10  )  # obtain configured data path and expand ~
11  runs = get_runs(data_path)  # get list of runs
12
13  for session, database_path in runs:
14      print(session.name)
15      with Database(database_path) as db:
16          results = db.get_results(conditions=["w > 0.19", "w < 0.21"])
17          for num, parameters, _metadata in results:
18              print("\t", f"{num:>6}: {parameters}")
19              data = Result(
20                  data_path=data_path,
21                  session=session,
22                  num=num,
23                  skip_vecs_1d=True,
24                  skip_vals_2d=True,
25                  skip_vecs_2d=True,
26              )
27              vals = data.vals_1d
28              print("\t\t", vals)
```

Listing 9: Example Python script to load the simulation results.

```
2025-07-14T14:37:09.840098
     213: a=0.2 m=1.0 mu=0.0 delta=1.0 alpha=0.3 …
    [[-30.01999201 -20.01999201  20.01999201   30.0…
     400: a=0.2 m=1.0 mu=0.0 delta=1.0 alpha=0.3 …
    [[-30.68665867 -19.35332534  19.35332534   30.6…
     505: a=0.2 m=1.0 mu=0.0 delta=1.0 alpha=0.3 …
    [[-27.85332534 -22.18665867  22.18665867   27.8…
     566: a=0.2 m=1.0 mu=0.0 delta=1.0 alpha=0.3 …
    [[-27.85332534 -22.18665867  22.18665867   27.8…
     580: a=0.2 m=1.0 mu=0.0 delta=1.0 alpha=0.3 …
```

Plot

As a last step, we can use the data to, for example, plot the lowest eigenvalue of the finite 2d simulation.

```python
import os
from pathlib import Path

import matplotlib.pyplot as plt
import numpy as np
from mbs.db import Database, Result, get_runs
from mbs.scripts.config import get_config

conf = get_config()  # read configuration files
data_path = Path(
    os.path.expanduser(conf.get("general", "data_path"))
)  # obtain configured data path and expand ~
runs = get_runs(data_path)  # get list of runs

for session, database_path in runs:
    print(session.name)
    with Database(database_path) as db:
        results = db.get_results(conditions=["w > 0.19", "w < 0.21"])

        energy = []
        b = []
        m0 = []

        for num, parameters, _metadata in results:
            data = Result(
                data_path=data_path,
                session=session,
                num=num,
                skip_vals_1d=True,
                skip_vecs_1d=True,
                skip_vecs_2d=True,
            )
            vals = data.vals_2d
            assert (
                vals is not None
            )  # Assert that we haven't made a mistake before when reading the data

            min_val = np.nanmin(np.abs(vals))
```
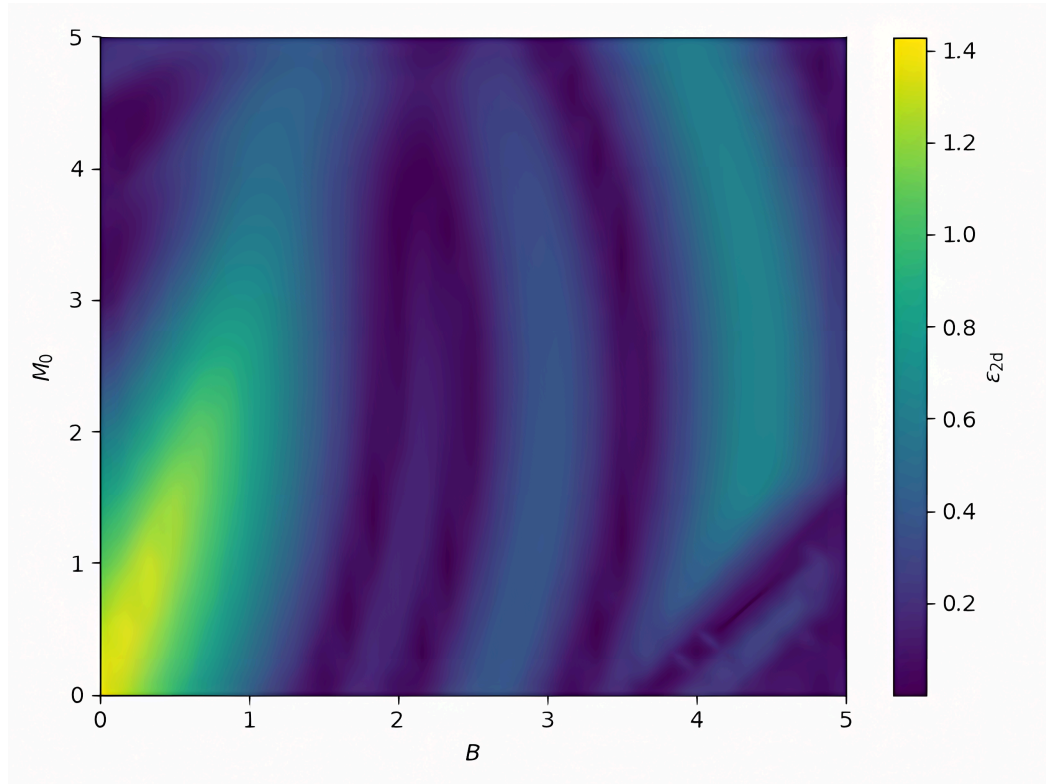
Figure 39: Plot output of the custom script in Listing 10.

```
39
40                b.append(parameters.b)
41                m0.append(parameters.m0)
42                energy.append(min_val)
43
44            plt.figure()
45            im = plt.tripcolor(b, m0, energy, shading="gouraud")
46            cbar = plt.colorbar(im)
47            cbar.set_label(r"$\epsilon_\mathrm{2d}$")
48
49            plt.xlim(np.nanmin(b), np.nanmax(b))
50            plt.ylim(np.nanmin(m0), np.nanmax(m0))
51            plt.xlabel("$B$")
52            plt.ylabel("$M_0$")
53            plt.tight_layout()
54
55            plt.savefig(f"{session.name}.png")
```

Listing 10: Example Python script to plot the simulation results.

And voila, you have your own plot (see Figure 39)!

B.2 Dynamics of a Moving Domain Wall

The second piece of software[130] is used to simulate the time evolution of a time-dependent system where the time-dependence is given by the movement of the magnetic domain wall. The numerical part is handled by `tkwant`[129] around which this software is a wrapper, that handles the setup of the lattice, magnetic texture and dynamics. In the following, a short tutorial that walks through the process of running a simulation.

B.2.1 Installation

The software is published under [130] and also available in the supplemental data[60]. It can be installed as a normal Python package with usual means, but it might be required or beneficial to first manually install `kwant` and `tkwant` in a Conda environment, as their build process might break when installing with `pip`.

B.2.2 Configuration

The input to the simulation is a packed `.tar.xz` folder with the following content

- `config.json`: system parameters
- `mask.png`: sample mask
- `wall/*.png`: domain wall positions

In the following sections, we introduce all of them.

System Parameters

The first part is a JSON-file that describes the system and can be verified using a schema. An example is shown in Listing 11 and split into three sections with the following parameters

- `evolution`: time evolution parameters
  - ‣ `t_max`: final time

```
 1  {
 2      "$schema": "https://solidtux-phd.gitlab.io/kwant-braiding/config-v1.schema.
        json",
 3      "evolution": {
 4          "t_max": 100.0,
 5          "steps": 1000
 6      },
 7      "calculation": {
 8          "sparse": true,
 9          "downsample": 2,
10          "follow_wall": false
11      },
12      "system": {
13          "lattice_constant": 0.1,
14          "delta": 1.0,
15          "mass": 1.0,
16          "alpha": 0.8,
17          "magnetic_field": 3,
18          "chemical_potential": 0.0,
19          "domain_wall": {
20              "width": 0.2,
21              "scale": 0.02,
22              "amplitude": 3
23          }
24      }
25  }
```

Listing 11: Example configuration file which configures the relevant parameters.

- steps: time steps for export (tkwant might make more steps internally)
- calculation: non-physical parameters
  - sparse: use sparse matrices
  - downsample: use only every n-pixel of the mask to allow for higher image resolution with a reasonable lattice (see next section)
  - follow_wall: the field direction of the magnetisation follows the domain wall (only relevant if the domain wall is tilted during the simulation)
- system: physical parameters
  - lattice_constant: grid spacing
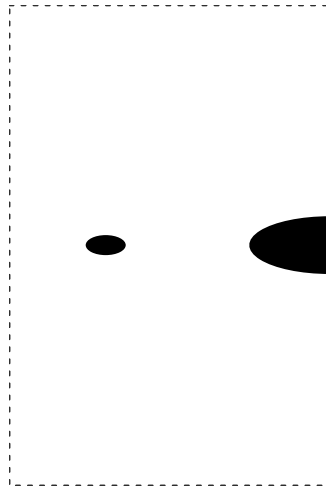 - delta: superconducting s-wave gap

Figure 40: Example mask for the dynamical simulation. The border has been added afterwards to make the outline visible. White denotes areas that are part of the lattice.

- ‣ `mass`: effective mass
- ‣ `alpha`: Rashba SOC strength
- ‣ `magnetic_field`: constant external field
- ‣ `chemical_potential`: chemical potential
- ‣ `domain_wall`: domain wall parameters
    - – `width`: width of the domain wall
    - – `scale`: steppness of the domain wall
    - – `amplitude`: magnitude of the magnetisation

Sample Mask

The sample mask is a simple black and white image, where white parts correspond to the part of the area that is included in the lattice. See Figure 40 for an example. The resolution of the image divided by the downsample parameter from before gives the size of the sample.

Domain Wall Position

The domain wall position is given by a list of images with coloured dots. The dimensions can be larger than the mask, which causes the overlap to be cut off
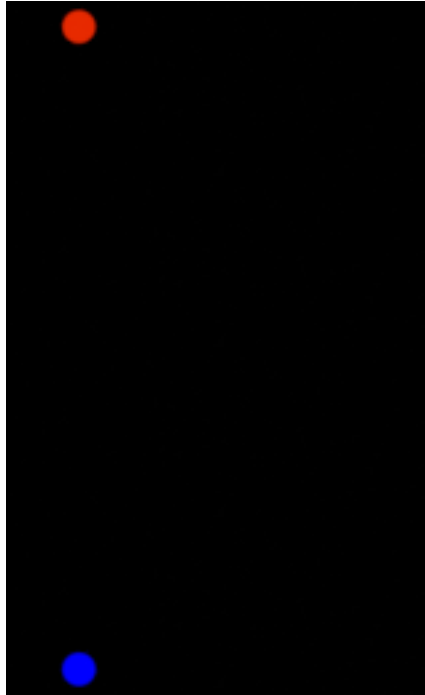
Figure 41: Example domain wall position image.

equally around all edges. That allows the end of the domain wall to be outside the sample. In Figure 41, and example is given. The two ends of the domain wall are identified by the average position of the different colours. A moving domain wall is realised by providing multiple images named `0001.png`, `0002.png`, … in the `wall` folder. The number of images does not have to be equal to the `steps` parameter from before, as the domain wall positions are interpolated anyway.

B.2.3 Running the Simulation

To run the simulation, simply give the path to the packaged input and the desired output folder to the software:

```
braid INPUT.tar.xz OUTPUT
```

The simulation can be interrupted and continued at any point.

B.2.4 Understanding the Output

When the simulation is finished, the output folder will contain many files. The results are found in four NumPy files in the folder `data`:

- `init.npz`: the ground state found for the initial configuration at $t = 0$
  - ‣ `h0`: Hamiltonian
  - ‣ `psi0`: eigenstate
  - ‣ `e0`: energy
- `lattice.npz`: coordinates of the lattice points (mainly relevant for an irregular mask)
  - ‣ `xvals`: x-coordinates
  - ‣ `yvals`: y-coordinates
- `mag.npz`: state of the domain wall over the time of the simulation
  - ‣ `pos`: position of all domain wall edges
  - ‣ `angle`: angles of the domain wall (only relevant when the wall is tilted)
- `res.npz`: main results of the simulation
  - ‣ `pos`: position expectation value of the state over time
  - ‣ `dens`: local density of the state over time
  - ‣ `psi`: full state over time
  - ‣ `time`: simulation **wall-time** over the simulation

Glossary

ABS: Andreev bound state

BCS: Bardeen-Cooper-Schrieffer

BKT: Berezinskii-Kosterlitz-Thouless

BdG: Bogoliubov-de Gennes

CS: chiral symmetry

ED: exact diagonalization

FP: field-polarized

FQHE: fractional quantum Hall effect

IQHE: integer quantum Hall effect

MBS: Majorana bound state

MSH: magnet-superconductor hybrid

PHS: particle-hole symmetry

QHE: quantum Hall effect

SAT: spin-alignment transformation

SC: superconductor

SOC: spin-orbit coupling

TRS: time-reversal symmetry

Bibliography

[1]   Arute F, Arya K, Babbush R, Bacon D, Bardin JC, Barends R, et al. Quantum Supremacy Using a Programmable Superconducting Processor. Nature 2019;574:505–10. https://doi.org/10.1038/s41586-019-1666-5.

[2]   Acharya R, Abanin DA, Aghababaie-Beni L, Aleiner I, Andersen TI, Ansmann M, et al. Quantum Error Correction below the Surface Code Threshold. Nature 2025;638:920–6. https://doi.org/10.1038/s41586-024-08449-y.

[3]   Fowler AG, Mariantoni M, Martinis JM, Cleland AN. Surface Codes: Towards Practical Large-Scale Quantum Computation. Phys Rev a 2012;86:32324. https://doi.org/10.1103/PhysRevA.86.032324.

[4]   Yang Z, Zolanvari M, Jain R. A Survey of Important Issues in Quantum Computing and Communications. IEEE Commun Surv Tutor 2023;25:1059–94. https://doi.org/10.1109/COMST.2023.3254481.

[5]   Kitaev A. Fault-Tolerant Quantum Computation by Anyons. Annals of Physics 2003;303:2–30. https://doi.org/10.1016/S0003-4916(02)00018-0.

[6]   Freedman M, Kitaev A, Larsen M, Wang Z. Topological Quantum Computation. Bull Am Math Soc 2003;40:31–8. https://doi.org/10.1090/S0273-0979-02-00964-3.

[7]   Nayak C, Simon SH, Stern A, Freedman M, Das Sarma S. Non-Abelian Anyons and Topological Quantum Computation. Rev Mod Phys 2008;80:1083–159. https://doi.org/10.1103/RevModPhys.80.1083.

[8]   Alicea J, Oreg Y, Refael G, Oppen F von, Fisher MPA. Non-Abelian Statistics and Topological Quantum Information Processing in 1D Wire Networks. Nature Phys 2011;7:412–7. https://doi.org/10.1038/nphys1915.

[9]   Stern A, Lindner NH. Topological Quantum Computation — From Basic Concepts to First Experiments. Science 2013;339:1179–84. https://doi.org/10.1126/science.1231473.

[10]   Melnikov D, Mironov A, Mironov S, Morozov A, Morozov A. Towards Topological Quantum Computer. Nuclear Physics B 2018;926:491–508. https://doi.org/10.1016/j.nuclphysb.2017.11.016.

[11] Hell M, Flensberg K, Leijnse M. Coupling and Braiding Majorana Bound States in Networks Defined in Two-Dimensional Electron Gases with Proximity-Induced Superconductivity. Phys Rev B 2017;96:35444. https://doi.org/10.1103/PhysRevB.96.035444.

[12] Majorana E. Teoria simmetrica dell'elettrone e del positrone. Nuovo Cim 1937;14:171–84. https://doi.org/10.1007/BF02961314.

[13] Prada E, San-Jose P, Moor MWA de, Geresdi A, Lee EJH, Klinovaja J, et al. From Andreev to Majorana Bound States in Hybrid Superconductor–Semiconductor Nanowires. Nat Rev Phys 2020;2:575–94. https://doi.org/10.1038/s42254-020-0228-y.

[14] Kitaev AY. Unpaired Majorana Fermions in Quantum Wires. Phys-Usp 2001;44:131–6. https://doi.org/10.1070/1063-7869/44/10S/S29.

[15] Fu L, Kane CL. Superconducting Proximity Effect and Majorana Fermions at the Surface of a Topological Insulator. Phys Rev Lett 2008;100:96407. https://doi.org/10.1103/physrevlett.100.096407.

[16] Sau JD. Generic New Platform for Topological Quantum Computation Using Semiconductor Heterostructures. Phys Rev Lett 2010;104. https://doi.org/10.1103/PhysRevLett.104.040502.

[17] Alicea J. Majorana Fermions in a Tunable Semiconductor Device. Phys Rev B 2010;81:125318. https://doi.org/10.1103/PhysRevB.81.125318.

[18] Lutchyn RM, Stanescu TD, Das Sarma S. Search for Majorana Fermions in Multiband Semiconducting Nanowires. Phys Rev Lett 2011;106:127001. https://doi.org/10.1103/PhysRevLett.106.127001.

[19] Kjaergaard M, Wölms K, Flensberg K. Majorana Fermions in Superconducting Nanowires without Spin-Orbit Coupling. Phys Rev B 2012;85:20503. https://doi.org/10.1103/physrevb.85.020503.

[20] Klinovaja J, Loss D. Composite Majorana Fermion Wave Functions in Nanowires. Phys Rev B 2012;86:85408. https://doi.org/10.1103/PhysRevB.86.085408.

[21] Mourik V, Zuo K, Frolov SM, Plissard SR, Bakkers EPAM, Kouwenhoven LP. Signatures of Majorana Fermions in Hybrid Superconductor-Semiconductor Nanowire Devices. Science 2012;336:1003–7. https://doi.org/10.1126/science.1222360.

[22] Sticlet D, Bena C, Simon P. Spin and Majorana Polarization in Topological Superconducting Wires. Phys Rev Lett 2012;108. https://doi.org/10.1103/PhysRevLett.108.096802.

[23] Microsoft Azure Quantum, Aghaee M, Alcaraz Ramirez A, Alam Z, Ali R, Andrzejczuk M, et al. Interferometric Single-Shot Parity Measurement in InAs–Al Hybrid Devices. Nature 2025;638:651–5. https://doi.org/10.1038/s41586-024-08445-2.

[24] Kim SK, Tewari S, Tserkovnyak Y. Control and Braiding of Majorana Fermions Bound to Magnetic Domain Walls. Phys Rev B 2015;92:20412. https://doi.org/10.1103/PhysRevB.92.020412.

[25] Heimes A, Mendler D, Kotetes P. Interplay of Topological Phases in Magnetic Adatom-Chains on Top of a Rashba Superconducting Surface. New J Phys 2015;17:23051. https://doi.org/10.1088/1367-2630/17/2/023051.

[26] Peng Y, Pientka F, Glazman LI, Von Oppen F. Strong Localization of Majorana End States in Chains of Magnetic Adatoms. Phys Rev Lett 2015;114:106801. https://doi.org/10.1103/PhysRevLett.114.106801.

[27] Röntynen J, Ojanen T. Topological Superconductivity and High Chern Numbers in 2D Ferromagnetic Shiba Lattices. Phys Rev Lett 2015;114:236803. https://doi.org/10.1103/PhysRevLett.114.236803.

[28] Röntynen J, Ojanen T. Chern Mosaic: Topology of Chiral Superconductivity on Ferromagnetic Adatom Lattices. Phys Rev B 2016;93:94521. https://doi.org/10.1103/PhysRevB.93.094521.

[29] Christensen MH, Schecter M, Flensberg K, Andersen BM, Paaske J. Spiral Magnetic Order and Topological Superconductivity in a Chain of Magnetic Adatoms on a Two-Dimensional Superconductor. Phys Rev B 2016;94:144509. https://doi.org/10.1103/PhysRevB.94.144509.

[30] Güngördü U, Sandhoefner S, Kovalev AA. Stabilization and Control of Majorana Bound States with Elongated Skyrmions. Phys Rev B 2018;97:115136. https://doi.org/10.1103/physrevb.97.115136.

[31] Rex S, Gornyi IV, Mirlin AD. Majorana Bound States in Magnetic Skyrmions Imposed onto a Superconductor. Phys Rev B 2019;100:64504. https://doi.org/10/gm2ndq.

[32] Rex S, Gornyi IV, Mirlin AD. Majorana Modes in Emergent-Wire Phases of Helical and Cycloidal Magnet-Superconductor Hybrids. Phys Rev B 2020;102:224501. https://doi.org/10.1103/PhysRevB.102.224501.

[33] Güngördü U, Kovalev AA. Majorana Bound States with Chiral Magnetic Textures. Arxiv220411818 Cond-Mat Physicsquant-Ph 2022.

[34] Schossmann M, Carbotte JP. Pauli Limiting of the Upper Critical
      Magnetic Field. Phys Rev B 1989;39:4210–6.
      https://doi.org/10.1103/PhysRevB.39.4210.

[35] Muratov CB, Osipov VV. Theory of 360° Domain Walls in Thin
      Ferromagnetic Films. J Appl Phys 2008;104:53908.
      https://doi.org/10.1063/1.2970100.

[36] Dean J, Kohn A, Kovács A, Zeltser A, Carey MJ, Hrkac G, et al. The
      Formation Mechanism of 360° Domain Walls in Exchange-Biased
      Polycrystalline Ferromagnetic Films. J Appl Phys 2011;110:73901.
      https://doi.org/10.1063/1.3642982.

[37] Zhang J, Siddiqui SA, Ho P, Currivan-Incorvia JA, Tryputen L, Lage E,
      et al. 360° Domain Walls: Stability, Magnetic Field and Electric
      Current Effects. New J Phys 2016;18:53028.
      https://doi.org/10.1088/1367-2630/18/5/053028.

[38] Zhou X, Vernier N, Agnus G, Eimer S, Lin W, Zhai Y. Highly
      Anisotropic Magnetic Domain Wall Behavior in In-Plane Magnetic
      Films. Phys Rev Lett 2020;125:237203.
      https://doi.org/10.1103/PhysRevLett.125.237203.

[39] Marrows CH. Spin-Polarised Currents and Magnetic Domain Walls.
      Advances in Physics 2005;54:585–713.
      https://doi.org/10.1080/00018730500442209.

[40] Emori S, Bauer U, Ahn S-M, Martinez E, Beach GSD. Current-Driven
      Dynamics of Chiral Ferromagnetic Domain Walls. Nature Mater
      2013;12:611–6. https://doi.org/10/f44tqd.

[41] Ryu K-S, Thomas L, Yang S-H, Parkin S. Chiral Spin Torque at
      Magnetic Domain Walls. Nature Nanotech 2013;8:527–33.
      https://doi.org/10/ghpbt8.

[42] Hu J-M, Yang T, Momeni K, Cheng X, Chen L, Lei S, et al. Fast
      Magnetic Domain-Wall Motion in a Ring-Shaped Nanowire Driven by
      a Voltage. Nano Lett 2016;16:2341–8. https://doi.org/10/f8jbpr.

[43] Nasseri SA. Magnetic Domain Wall Motion. 2017.

[44] Hauck D, Rex S, Garst M. Magnetic 2π Domain Walls for Tunable
      Majorana Devices. Arxiv:250521779 2025.
      https://doi.org/10.48550/arXiv.2505.21779.

[45] Sharma RG. Superconductivity: Basics and Applications to Magnets.
      Springer International Publishing; 2015.

[46]   Tinkham M. Introduction to Superconductivity. 2. ed. New York [U.a.]:
        McGraw-Hill; 1996.

[47]   Van Delft D, Kes P. The Discovery of Superconductivity. Phys Today
        2010;63:38–43. https://doi.org/10.1063/1.3490499.

[48]   Kamerlingh-Onnes H. Further Experiments with Liquid Helium. C.
        On the Change of Electrical Resistance of Pure Metals at Very Low
        Temperatures Etc. ITT. The Resistance of Platinum at Helium
        Temperatures. Commun Phys Lab Univ Leiden 1911;119:19–27.

[49]   Kamerlingh-Onnes H. The Resistance of Pure Mercury at Helium
        Temperatures. Commun Phys Lab Univ Leiden B 1911;120.

[50]   Kamerlingh-Onnes H. The Superconductivity of Mercury. Comm Phys
        Lab Univ Leiden 1911;122:124.

[51]   Kamerlingh-Onnes H. The Sudden Disappearance of the Ordinary
        Resistance of Tin, and the Super-Conductive State of Lead. Commun
        Phys Lab Univ Leiden D 1913;133.

[52]   Meissner W, Ochsenfeld R. Ein neuer Effekt bei Eintritt der
        Supraleitfähigkeit. Naturwissenschaften 1933;21:787–8.
        https://doi.org/10.1007/BF01504252.

[53]   London F, London H, Lindemann FA. The Electromagnetic Equations
        of the Supraconductor. Proc R Soc Lond Ser - Math Phys Sci
        1935;149:71–88. https://doi.org/10.1098/rspa.1935.0048.

[54]   Bardeen J, Cooper LN, Schrieffer JR. Theory of Superconductivity.
        Phys Rev 1957;108:1175–204.
        https://doi.org/10.1103/PhysRev.108.1175.

[55]   Timm C. Theory of Superconductivity 2020.

[56]   Schrieffer JR. Theory of Superconductivity. New York: Benjamin; 1964.

[57]   Zhu J-X. Bogoliubov-de Gennes Method and Its Applications. vol. 924.
        Cham: Springer International Publishing; 2016.
        https://doi.org/10.1007/978-3-319-31314-6.

[58]   Gennes PGD. Superconductivity Of Metals And Alloys. CRC Press;
        2018.

[59]   Altland A, Simons BD. Condensed Matter Field Theory. 2. ed., [repr.].
        Cambridge [U.a.]: Cambridge Univ. Press; 2012.

[60]   Hauck D. Data for Thesis: Magnetic 2π Domain Walls for Tunable
        Majorana Devices 2025. https://doi.org/10.35097/rjh6d2704g05qzsg.

[61]   Munkres JR. Topology. 2. ed., Pearson new internat. ed. Harlow:
        Pearson; 2014.

[62] Klitzing KV, Dorda G, Pepper M. New Method for High-Accuracy Determination of the Fine-Structure Constant Based on Quantized Hall Resistance. Phys Rev Lett 1980;45:494–7. https://doi.org/10.1103/PhysRevLett.45.494.

[63] Hatsugai Y. Topological Aspects of the Quantum Hall Effect. J Phys: Condens Matter 1997;9:2507–49. https://doi.org/10.1088/0953-8984/9/12/003.

[64] Avron JE, Osadchy D, Seiler R. A Topological Look at the Quantum Hall Effect. Phys Today 2003;56:38–42. https://doi.org/10.1063/1.1611351.

[65] Matthews J. Temperature Dependence of the Hall and Longitudinal Resistances in a Quantum Hall Resistance Standard. J Res Natl Inst Stand Technol 2005;110. https://doi.org/10.6028/jres.110.078.

[66] Laughlin RB. Quantized Hall Conductivity in Two Dimensions. Phys Rev B 1981;23:5632–3. https://doi.org/10.1103/PhysRevB.23.5632.

[67] Halperin BI. Quantized Hall Conductance, Current-Carrying Edge States, and the Existence of Extended States in a Two-Dimensional Disordered Potential. Phys Rev B 1982;25:2185–90. https://doi.org/10.1103/PhysRevB.25.2185.

[68] Thouless DJ, Kohmoto M, Nightingale MP, Den Nijs M. Quantized Hall Conductance in a Two-Dimensional Periodic Potential. Phys Rev Lett 1982;49:405–8. https://doi.org/10.1103/PhysRevLett.49.405.

[69] Kosterlitz JM, Thouless DJ. Ordering, Metastability and Phase Transitions in Two-Dimensional Systems. J Phys C: Solid State Phys 1973;6:1181. https://doi.org/10.1088/0022-3719/6/7/010.

[70] Akhmerov A, Sau J, Heck B van, Rubbert S, Skolasiński R, Nijholt B, et al. Online Course on Topology in Condensed Matter 2021. https://topocondmat.org/ (accessed September 26, 2024).

[71] Qi X-L, Zhang S-C. Topological Insulators and Superconductors. Rev Mod Phys 2011;83:1057–110. https://doi.org/10.1103/RevModPhys.83.1057.

[72] Fu L, Kane CL. Topological Insulators with Inversion Symmetry. Phys Rev B 2007;76:45302. https://doi.org/10.1103/PhysRevB.76.045302.

[73] Kitaev A, Lebedev V, Feigel'man M. Periodic Table for Topological Insulators and Superconductors. In:. AIP Conf. Proc., Chernogolokova (Russia): AIP; 2009, pp. 22–30. https://doi.org/10.1063/1.3149495.

[74]   Altland A, Zirnbauer MR. Nonstandard Symmetry Classes in Mesoscopic Normal-Superconducting Hybrid Structures. Phys Rev B 1997;55:1142–61. https://doi.org/10.1103/PhysRevB.55.1142.

[75]   Zirnbauer MR. Riemannian Symmetric Superspaces and Their Origin in Random-Matrix Theory. J Math Phys 1996;37:4986–5018. https://doi.org/10.1063/1.531675.

[76]   Dyson FJ. The Threefold Way. Algebraic Structure of Symmetry Groups and Ensembles in Quantum Mechanics. J Math Phys 1962;3:1199–215. https://doi.org/10.1063/1.1703863.

[77]   Wigner E. Gruppentheorie und ihre Anwendung auf die Quantenmechanik der Atomspektren. Wiesbaden: Vieweg+Teubner Verlag; 1931. https://doi.org/10.1007/978-3-663-02555-9.

[78]   Varjas D, Rosdahl TÖ, Akhmerov AR. Qsymm: Algorithmic Symmetry Finding and Symmetric Hamiltonian Generation. New J Phys 2018;20:93026. https://doi.org/10.1088/1367-2630/aadf67.

[79]   Chiu C-K, Teo JCY, Schnyder AP, Ryu S. Classification of Topological Quantum Matter with Symmetries. Rev Mod Phys 2016;88:35005. https://doi.org/10.1103/RevModPhys.88.035005.

[80]   Bonesteel NE, Hormozi L, Zikos G, Simon SH. Braid Topologies for Quantum Computation. Phys Rev Lett 2005;95:140503. https://doi.org/10.1103/PhysRevLett.95.140503.

[81]   Müller J, Rosch A, Garst M. Edge Instabilities and Skyrmion Creation in Magnetic Layers. New J Phys 2016;18:65006. https://doi.org/10.1088/1367-2630/18/6/065006.

[82]   Coey JMD, Parkin SS, editors. Handbook of Magnetism and Magnetic Materials. Cham: Springer International Publishing; 2021. https://doi.org/10.1007/978-3-030-63210-6.

[83]   Abert CW. Discrete Mathematical Concepts in Micromagnetic Computations. 2013.

[84]   Hubert A, Schäfer R. Magnetic Domains: The Analysis of Magnetic Microstructures. Springer Science & Business Media; 1998.

[85]   Zeeman P. Ueber Einen Einfluss Der Magnetisirung Auf Die Natur Des von Einer Substanz Emittirten Lichtes. 1896.

[86]   Condat CA, Guyer RA, Miller MD. Double Sine-Gordon Chain. Phys Rev B 1983;27:474–94. https://doi.org/10.1103/PhysRevB.27.474.

[87]   Campbell DK, Peyrard M, Sodano P. Kink-Antikink Interactions in the
        Double Sine-Gordon Equation. Physica D: Nonlinear Phenomena
        1986;19:165–205. https://doi.org/10.1016/0167-2789(86)90019-9.

[88]   Sakurai JJ, Napolitano J. Modern Quantum Mechanics. Third edition.
        Cambridge, United Kingdom New York, NY Port Melbourne, VIC New
        Delhi Singapore: Cambridge University Press; 2011.
        https://doi.org/10.1017/9781108587280.

[89]   Крылов АН. О Численном Решении Уравнения, Которым в
        Технических Вопросах Определяются Частоты Малых Колебаний
        Материальных Систем. Известия Российской Академии Наук
        Серия Математическая 1931:491–539.

[90]   Mises RV, Pollaczek-Geiringer H. Praktische Verfahren Der
        Gleichungsauflösung. Z Angew Math Mech 1929;9:58–77.
        https://doi.org/10.1002/zamm.19290090105.

[91]   Lehoucq RB, Sorensen DC, Yang C. ARPACK Users' Guide: Solution of
        Large-Scale Eigenvalue Problems with Implicitly Restarted Arnoldi
        Methods. SIAM; 1998.

[92]   Arnoldi WE. The Principle of Minimized Iterations in the Solution of
        the Matrix Eigenvalue Problem. Quart Appl Math 1951;9:17–29.
        https://doi.org/10.1090/qam/42792.

[93]   Lehoucq RB, Sorensen DC. Deflation Techniques for an Implicitly
        Restarted Arnoldi Iteration. SIAM J Matrix Anal & Appl 1996;17:789–
        821. https://doi.org/10.1137/s0895479895281484.

[94]   Lehoucq RB. Implicitly Restarted Arnoldi Methods and Subspace
        Iteration. SIAM J Matrix Anal & Appl 2001;23:551–62.
        https://doi.org/10.1137/s0895479899358595.

[95]   Bedow J, Mascot E, Posske T, Uhrig GS, Wiesendanger R, Rachel S, et
        al. Topological Superconductivity Induced by a Triple-q Magnetic
        Structure. Phys Rev B 2020;102:180504.
        https://doi.org/10.1103/physrevb.102.180504.

[96]   Neuhaus-Steinmetz J, Vedmedenko EY, Posske T, Wiesendanger R.
        Complex Magnetic Ground States and Topological Electronic Phases of
        Atomic Spin Chains on Superconductors. Phys Rev B 2022;105:165415.
        https://doi.org/10.1103/PhysRevB.105.165415.

[97]   Schneider L, Beck P, Posske T, Crawford D, Mascot E, Rachel S, et al.
        Topological Shiba Bands in Artificial Spin Chains on Superconductors.
        Nat Phys 2021. https://doi.org/10.1038/s41567-021-01234-y.

[98] Bedow J, Mascot E, Hodge T, Rachel S, Morr DK. Implementation of Topological Quantum Gates in Magnet-Superconductor Hybrid Structures. Arxiv:230204889 2023.

[99] Nothhelfer J, Díaz SA, Kessler S, Meng T, Rizzi M, Hals KMD, et al. Steering Majorana Braiding via Skyrmion-Vortex Pairs: A Scalable Platform. Phys Rev B 2022;105:224509. https://doi.org/10.1103/PhysRevB.105.224509.

[100] Bobkova IV, Bobkov AM, Kamra A, Belzig W. Magnon-Cooparons in Magnet-Superconductor Hybrids. Commun Mater 2022;3:95. https://doi.org/10.1038/s43246-022-00321-8.

[101] Ozmetin AE, Rathnayaka KDD, Naugle DG, Lyuksyutov IF. Strong Increase in Critical Field and Current in Magnet-Superconductor Hybrids. J Appl Phys 2009;105:7. https://doi.org/10.1063/1.3076517.

[102] Menezes RM, Neto JFS, Silva CCDS, Milošević MV. Manipulation of Magnetic Skyrmions by Superconducting Vortices in Ferromagnet-Superconductor Heterostructures. Phys Rev B 2019;100:14431. https://doi.org/10.1103/PhysRevB.100.014431.

[103] Petrović AP, Raju M, Tee XY, Louat A, Maggio-Aprile I, Menezes RM, et al. Skyrmion-(Anti)Vortex Coupling in a Chiral Magnet-Superconductor Heterostructure. Phys Rev Lett 2021;126:117205. https://doi.org/10.1103/PhysRevLett.126.117205.

[104] Silaev MA, Volovik GE. Topological Superfluid ^{3}He–B: Fermion Zero Modes on Interfaces and in the Vortex Core. J Low Temp Phys 2010;161:460–73. https://doi.org/10.1007/s10909-010-0226-z.

[105] Yang G, Stano P, Klinovaja J, Loss D. Majorana Bound States in Magnetic Skyrmions. Phys Rev B 2016;93:224505. https://doi.org/10.1103/PhysRevB.93.224505.

[106] Sau JD, Sarma SD. Realizing a Robust Practical Majorana Chain in a Quantum-Dot-Superconductor Linear Array. Nat Commun 2012;3:964. https://doi.org/10.1038/ncomms1966.

[107] Pientka F, Glazman LI, Oppen F von. Topological Superconducting Phase in Helical Shiba Chains. Phys Rev B 2013;88:155420. https://doi.org/10.1103/PhysRevB.88.155420.

[108] Pawlak R, Hoffman S, Klinovaja J, Loss D, Meyer E. Majorana Fermions in Magnetic Chains. Prog Part Nucl Phys 2019;107:1–19. https://doi.org/10.1016/j.ppnp.2019.04.004.

[109] Hess R, Legg HF, Loss D, Klinovaja J. Prevalence of Trivial Zero-Energy Sub-Gap States in Non-Uniform Helical Spin Chains on the Surface of Superconductors. Arxiv220402324 Cond-Mat 2022.

[110] Schneider L, Beck P, Neuhaus-Steinmetz J, Rózsa L, Posske T, Wiebe J, et al. Precursors of Majorana Modes and Their Length-Dependent Energy Oscillations Probed at Both Ends of Atomic Shiba Chains. Nat Nanotechnol 2022;17:384–9. https://doi.org/10.1038/s41565-022-01078-4.

[111] Chatterjee P, Pradhan S, Nandy AK, Saha A. Tailoring Phase Transition from Topological Superconductor to Trivial Superconductor Induced by Magnetic Textures of a Spin-Chain on a p-Wave Superconductor. Arxiv:220615196 2022.

[112] Scheurer MS, Shnirman A. Nonadiabatic Processes in Majorana Qubit Systems. Phys Rev B 2013;88:64515. https://doi.org/10.1103/PhysRevB.88.064515.

[113] Fujimoto S. Topological Order and Non-Abelian Statistics in Noncentrosymmetric s -Wave Superconductors. Phys Rev B 2008;77:220501. https://doi.org/10.1103/PhysRevB.77.220501.

[114] Tewari S, Sau JD. Topological Invariants for Spin-Orbit Coupled Superconductor Nanowires. Phys Rev Lett 2012;109:150408. https://doi.org/10.1103/PhysRevLett.109.150408.

[115] Asbóth JK, Oroszlány L, Pályi A. A Short Course on Topological Insulators: Band-structure Topology and Edge States in One and Two Dimensions. Arxiv150902295 Cond-Mat 2016;919. https://doi.org/10.1007/978-3-319-25607-8.

[116] Mong RSK, Bardarson JH, Moore JE. Quantum Transport and Two-Parameter Scaling at the Surface of a Weak Topological Insulator. Phys Rev Lett 2012;108:76804. https://doi.org/10.1103/PhysRevLett.108.076804.

[117] Ringel Z, Kraus YE, Stern A. Strong Side of Weak Topological Insulators. Phys Rev B 2012;86:45102. https://doi.org/10.1103/PhysRevB.86.045102.

[118] Sato M, Takahashi Y, Fujimoto S. Non-Abelian Topological Order in s -Wave Superfluids of Ultracold Fermionic Atoms. Phys Rev Lett 2009;103:20401. https://doi.org/10.1103/PhysRevLett.103.020401.

[119] Loder F, Kampf AP, Kopp T. Route to Topological Superconductivity via Magnetic Field Rotation. Sci Rep 2015;5:15302. https://doi.org/10.1038/srep15302.

[120] Xie Y, Chai R-F, Zhu X, Zha G-Q. Inhomogeneous Stripe Phase and Tunable Majorana Zero Modes in Rashba \mkbibemph{s} -Wave Superconducting Systems in the Presence of in-Plane Zeeman Field. J Appl Phys 2024;136:124303. https://doi.org/10.1063/5.0232158.

[121] Volovik GE. Linear Momentum in Ferromagnets. J Phys C: Solid State Phys 1987;20:L83–7. https://doi.org/10.1088/0022-3719/20/7/003.

[122] Bazaliy YB, Jones BA, Zhang S-C. Modification of the Landau-Lifshitz Equation in the Presence of a Spin-Polarized Current in Colossal- and Giant-Magnetoresistive Materials. Phys Rev B 1998;57:R3213–6. https://doi.org/10.1103/PhysRevB.57.R3213.

[123] Barnes SE, Maekawa S. Generalization of Faraday's Law to Include Nonconservative Spin Forces. Phys Rev Lett 2007;98:246601. https://doi.org/10.1103/PhysRevLett.98.246601.

[124] Braunecker B, Japaridze GI, Klinovaja J, Loss D. Spin-Selective Peierls Transition in Interacting One-Dimensional Conductors with Spin-Orbit Interaction. Phys Rev B 2010;82:45127. https://doi.org/10.1103/PhysRevB.82.045127.

[125] Wimmer M. Efficient Numerical Computation of the Pfaffian for Dense and Banded Skew-Symmetric Matrices. ACM Trans Math Softw TOMS 2012;38:1–17. https://doi.org/10.1145/2331130.2331138.

[126] Sedlmayr N, Bena C. Visualizing Majorana Bound States in One and Two Dimensions Using the Generalized Majorana Polarization. Phys Rev B 2015;92:115115. https://doi.org/10.1103/PhysRevB.92.115115.

[127] Ahumada-Centeno M, Amore P, Fernández FM, Manzanares-Martinez J. Quantum Particles in a Moving Potential. Phys Scr 2020;95:65405. https://doi.org/10.1088/1402-4896/ab80e6.

[128] Dirac PAM, Bohr NHD. The Quantum Theory of the Emission and Absorption of Radiation. Proc R Soc Lond Ser Contain Pap Math Phys Character 1997;114:243–65. https://doi.org/10.1098/rspa.1927.0039.

[129] Kloss T, Weston J, Gaury B, Rossignol B, Groth C, Waintal X. tkwant: A Software Package for Time-Dependent Quantum Transport. New J Phys 2021;23:23025. https://doi.org/10.1088/1367-2630/abddf7.

[130] Hauck D. kwant-braiding 2025. https://doi.org/10.5281/ZENODO.15467577.

[131] Hauck D. mbscluster 2025.
https://doi.org/10.5281/ZENODO.15528160.

[132] Dalcín L, Paz R, Storti M. MPI for Python. Journal of Parallel and
Distributed Computing 2005;65:1108–15.
https://doi.org/10.1016/j.jpdc.2005.03.010.